

SORBONNE UNIVERSITÉ

DOCTORAL THESIS

**Nonlinear quantum optics with a single
Rydberg superatom coupled to a
medium-finesse cavity**

Author:
Julien VANEECLOO

Supervisor:
Dr. ALEXEI OURJOUUMTSEV

*A thesis submitted in fulfillment of the requirements
for the degregge of Doctor of Philosophy
in the*

Quantum photonics
Physics Institute of the Collège de France

August 26, 2021

Abstract

by Julien VANEECLOO

The Thesis Abstract is written here (and usually kept to just this page). The page is kept centered vertically so can expand into the blank space above the title too...

Acknowledgements

Contents

Abstract	ii
Acknowledgements	iii
I Theoretical and Experimental tools	2
1 Rydberg superatoms in cavity for photon-photon interactions	5
1.1 Rydberg atoms	6
1.1.1 General properties	6
1.1.2 Dipole-dipole interaction	8
1.2 Atom-light interaction in a cavity (CQED)	8
1.2.1 A classical approach to the atom-cavity coupling	8
1.2.2 Quantum treatment for two levels atoms	10
1.2.3 Electromagnetically induced transparency	11
1.3 Effective interactions between optical photons	13
1.3.1 Blockade picture	13
1.3.2 Low-loss interactions	13
1.3.3 Outlook : Intra-cavity interaction	13
2 Presentation of the experimental setup	15
2.1 Experimental platform	16
2.1.1 Science cavity	18
2.1.2 Build-up cavities	24
2.2 Laser bench	27
2.2.1 Lasers	27
2.2.2 Frequency locking chain	29
2.3 Control setup	33
2.3.1 Hardware	33
2.3.2 Software	34
3 Preparation of an atomic ensemble inside the science cavity	37
3.1 Magneto-optical traps	39
3.1.1 Atomic beam: 2D MOT	40
3.1.2 3D Magneto-optical trap	41
3.2 Optical dipole traps	46
3.2.1 Conveyor belt	47
3.2.2 Crossed-dipole trap	49
3.3 Degenerate Raman sideband cooling	51

4 Detection for the atoms-cavity coupling	57
4.1 Detection setup	58
4.1.1 Homodyne detection	58
4.1.2 Intensity measurements	63
4.1.3 Optical setup	65
4.2 Strong coupling regime	68
4.2.1 Optical pumping	68
4.2.2 Coupling to $ 5S_{1/2}, F = 1\rangle \rightarrow 5P_{1/2}, F = 2\rangle$	70
II Observation of strongly interacting photons with a single Rydberg superatom	75
Bibliography	77

List of Figures

1.1	Cavity spectrum	9
1.2	Rabi Splitting	11
2.1	Rydberg vacuum chamber	16
2.2	Bake of Viton	17
2.3	Rydberg platform assembly	18
2.4	Twisted cavity	19
2.5	Losses	20
2.6	Laguerre-Gaussian modes	22
2.7	Image rotation	23
2.8	Blue cavities	25
2.9	Rubidium Lines and TA pro	27
2.10	SOLSTIS laser	28
2.11	Pound-Drever-Hall	30
2.12	Locking chain	31
2.13	Stable Laser System cavity and transfer cavity	31
2.14	Control of the experiment	33
2.15	Vito, Config Sequence	35
2.16	Vito, Config Channels	35
3.1	Vacuum chamber	38
3.2	MOT beams for the D ₂ line of rubidium 87	40
3.3	2D MOT drawing and 3D MOT loading rate	40
3.4	Magneto-optical trap setup	41
3.5	Absorption imaging	42
3.6	Temperature measurement	43
3.7	Magnetic field compensation	44
3.8	Gaussian beam	46
3.9	Conveyor belt	47
3.10	Transport with the conveyor belt	48
3.11	Longitudinal frequencies	49
3.12	1064 nm crossed-Dipole Trap	50
3.13	Degenerate Raman Sideband Cooling	52
3.14	Optimization of the cooling and compression	53
3.15	Sequence for the preparation of the atomic cloud	55
4.1	Homodyne detection	59
4.2	Wigner functions	60
4.3	Noise	61
4.4	Phase stability	62
4.5	SPAD vs APD	64

4.6	Photon statistics	64
4.7	Probe and detection setup	66
4.8	Atoms-cavity alignment	68
4.9	Optical pumping	69
4.10	Sequence and stability	71
4.11	Atoms-cavity coupling	72
4.12	Quadratures and phase for the atoms-cavity coupling	73
4.13	Reflection and Phase vs coupling regimes	73

List of Tables

3.1 Summery of the MOT parameters after 50 ms of loading.	44
---	----

Physical Constants

The `\constant` command is provided by the `siunitx` package, see its documentation for instructions on how to use it.

Constant Name

List of Symbols

<i>a</i>	distance	m
<i>P</i>	power	W (J s ⁻¹)
Symbol	Name	Unit
ω	angular frequency	rad

For/Dedicated to/To my...

Part I

Theoretical and Experimental tools

Chapter 1

Rydberg superatoms in cavity for photon-photon interactions

Contents

1.1 Rydberg atoms	6
1.1.1 General properties	6
Spectra of Alkali atoms	6
Hyperfine splitting and Pashen back regime	7
Lifetime and linewidth	7
Sensitivity to external field	7
1.1.2 Dipole-dipole interaction	8
interaction	8
Van-der walls interaction	8
1.2 Atom-light interaction in a cavity (CQED)	8
1.2.1 A classical approach to the atom-cavity coupling	8
Toy model cavity: spectrum	8
Coupling the cavity to a dielectric medium	9
1.2.2 Quantum treatment for two levels atoms	10
Field quantization and coherent driving	10
Atoms inside the resonator : Rabi Splitting	10
1.2.3 Electromagnetically induced transparency	11
Free space and dark state of the Hamiltonian	11
Transmission spectrum	12
1.3 Effective interactions between optical photons	13
1.3.1 Blockade picture	13
1.3.2 Low-loss interactions	13
small cloud response	13
possible protocol	13
1.3.3 Outlook : Intra-cavity interaction	13
Contact interaction	13

This first chapter is a brief introduction to the theoretical ideas behind this new experimental platform to support our technical and experimental choices. It is also an opportunity to highlight the assets of Rydberg atoms as well as the coupling to a medium-finesse cavity in the framework of quantum optics. In the first section, I introduce Rydberg atoms and their interesting features in the context of Alkali atoms, from the similarity with Hydrogen atom to the interaction potential between Rydberg atoms. In the next part, the coupling between atoms and light is discussed in the context of cavity quantum electrodynamics (CQED). In the last section of this chapter, we will focus on effective interactions between photons when CQED is associated with Rydberg atoms.

1.1 Rydberg atoms

1.1.1 General properties

Rydberg atoms are highly excited atoms characterized by a great principal quantum number n . Those atoms are extensively studied in many field of research (CITATION) and we would like to put emphasize on their unique and attracting properties. We will see that the energy ladder is not very different from hydrogen for Alkali atoms and that those highly excited states have an extended lifetime. Hyperfine splitting is often neglected for rydberg atoms and we will discussed in which limit this approximation is true. Finally, those states have a huge atomic dipole making them very sensitive to external field but also strongly interacting with one another via Van-der Waals forces.

Spectra of Alkali atoms

Alkali atoms stand in the first raw of the Mendeleev periodic table with a unique electron in their outer shell. This structure make them close to the hydrogen atom such that the spectrum of a given Alkali can be calculated by adding some correction to the energy levels of the hydrogen atom. This correction comes from the quantum defects theory to take into account the interactions of inner electrons with the outer electron. The energy ladder for Alkali atoms can thus be expressed as :

$$E_{n,l,j} = -\frac{m_c}{m_c + m_e} \frac{R_y}{n_{n,l,j}^{*2}}, \text{ with } n_{n,l,j}^{*} = n - \delta_{n,l,j} \quad (1.1)$$

where R_y is the Rydberg constant given by :

$$R_y = \frac{m_e e^4}{8\epsilon_0^2 h^3 c} \quad (1.2)$$

and δ_l is the quantum defect indexed by l , the angular orbital momentum, the fine structure j and the principal quantum number n . Those quantum defects are estimated from measurements of the spectrum with the following model :

$$\delta_{n,l,j} = \delta_{0,l,j} + \frac{\delta_{2,l,j}}{(n - \delta_{0,l,j})^2} + \frac{\delta_{l,j,4}}{(n - \delta_{0,l,j})^4} + \dots \quad (1.3)$$

The biggest quantum defect is obtained for S states and corresponds to 3.19 for Rubidium 87. As one can expect, low excited states of the outer electron are more significantly impacted by those corrections. Thereby, the Hydrogen atom spectrum is recovered in the limit where $n \ll 1$. Concretely, it corresponds to a screening of the core by inner electrons such that the

outer electron feels a unique charge from the core. This limit corresponds to the definition of a Rydberg atom.

Hyperfine splitting and Pashen back regime

It is often stated that the hyperfine splitting is negligible for Rydberg atoms because the last electron is far from the core. The good quantum number would be J and not F . Historically, many experiments were conducted around $n \approx 40$ where the hyperfine splitting is about 400 kHz for rubidium. It is neither big nor negligible depending on the experimental context. One way to fight force the change of basis is to add a magnetic field. If the zeeman splitting is great in front of the hyperfine energy. The hyperfine splitting is a correction to the van-der waals Hamiltonian with :

the system enters into the Pashen back regime with a hamiltonian almost diagonal in the J basis. This is an important effect at low Rydberg states that becomes less and less important

Lifetime and linewidth

Another interesting property of Rydberg atoms is their extended lifetime compare to low excited states. The fermi golden rule provide an interesting insight on the scaling law with the principal quantum number n . The emission rate from an excited state e to a lower level g is:

$$\Gamma_{g,e} = \frac{\omega_{g,e}^3 \langle d \rangle^2}{3\pi\epsilon_0\hbar c^3} \quad (1.4)$$

and the lifetime of the state e is then :

$$\tau_e = \frac{1}{\sum_i \Gamma_{g_i,e}} \quad (1.5)$$

with a summation of the states with lower energy: $E_{g_i} < E_e$ and a temperature of 0 K. The main contributions comes from transitions with very low excited states where $\hbar\omega_{g,e} \approx |E_{g_i}| \gg |E_e| \propto n^{-2}$ and $\langle d \rangle^2 \propto \ell_{max}/(2\ell + 1)n^{-3}$ with ℓ the angular momentum of the excited state. On contrary transitions with neighbors have an increased dipole $\langle d \rangle^2 \propto n^4$ but the energy spacing is much more smaller $\omega_{g,e} \propto n^{-3}$. In this case, the lifetime scales as n^3 for low angular momenta and up to n^5 for circular rydberg states ($\ell = n - 1$). At ambient temperature, the black body radiation favors transitions at the $\sim GHz$ corresponding to the energy between neighbors Rydberg states close to $n \approx 100$ (REF arc ou autre).

ref : regle d'or de fermi pour calculer

Sensitivity to external field

the sensitivity to an external field make Rydberg atoms very interesting for metrology. For instance for a constant extrernal field \mathcal{E} , the first order correction vanish by symmetry for $l = 0$ states. The second order quantum perturbation then gives :

$$\Delta E = \frac{1}{2}\alpha_0\mathcal{E}^2 = \sum_{i \neq j} \frac{|\langle \phi_i | d | \phi_j \rangle|^2}{E_i^0 - E_j^0} \mathcal{E}^2 \quad (1.6)$$

the polarizability (α_0) then scales in n^7 . This is of first importance for experiments. A special attention must be paid to the control of stray electric fields to not broaden the Rydberg linewidth. Circular Rydberg states are also very sensitive to the magnetic field but we will only used low angular momentum.(REF de manips)

1.1.2 Dipole-dipole interaction

interaction

$$V(\delta r) = \frac{\hat{\mu}_1 \hat{\mu}_2}{\|\delta r\|^3} - \frac{3(\hat{\mu}_1 \cdot \delta r)(\hat{\mu}_2 \cdot \delta r)}{\|\delta r\|^5} \quad (1.7)$$

This interaction couple two rydbergs states through their strong dipoles. This energy can either mixed them together whith other rydberg states. In this case we have the bound energy

Van-der walls interaction

1.2 Atom-light interaction in a cavity (CQED)

Historically, the cavity quantum electrodynamics was develop with very high finesse cavity and single atoms coupled to the electromagnetic field. The cavity geometry impose a single electromagnetic field mode with a well defined mode volume, while the high finesse ensure a strong interaction, or equivalently a strong coupling, between the field and the two level system. The intrinsic non-linearity of the two level system results in numerous interesting features. (examples) The high finesse criterion is for technical reason a challenging task that can be "countourner" in several ways =*i* Citer les alternatives : Jouer sur le volume de mode, jouer sur le couplage champ evanescent, jouer sur le nombre de systemes à 2 lvl. This experiment bet on the coupling with an ensemble of atoms. It naturally suffers from the loss of nonlinearity as saturation is reduced by a factor 1/N. The solution for this problem comes from the interaction of Rydberg atoms to map them directly on the atomic ensemble.

1.2.1 A classical approach to the atom-cavity coupling

Before going into a quantum description of the coupling between atoms and a resonator, we can have a good understanding of the problem by a simple classical model. The atom or the atomic ensemble is described as a generic dielectric medium with a complex refractive index $n(\omega)$ and a length l_0 . For clarity we will assume that the cavity is made of only two mirrors in vacuum separated by a distance L but it can be easily extended to N mirrors. A light beam of amplitude E_{in} at a frequency ω is injected from a mirror with a reflectivity r_0 and the second mirror is characterized by a reflectivity r_1 . We will further assume here that there is no loss in our mirror such that the transmission coefficient is $t_i = \sqrt{1 - r_i^2}$.

Toy model cavity: spectrum

Let's first describe the response in transmission of the resonator alone. The progressive field amplitude inside the cavity, E_{cav}^+ , is given by the sum of the input amplitude transmitted through the first mirror $t_0 E_{in}$ with the amplitude after one round trip in the resonator $r_0 r_1 t_0 E_{in} e^{i\omega 2L/c}$ and so on. This build-up gives :

$$E_{cav}^+ = \sum_n (r_0 r_1 e^{i\phi})^n t_0 E_{in} = \frac{t_0}{1 - r_0 r_1 e^{i\phi}} E_{in} \quad (1.8)$$

where $\phi = \omega 2L/c$. The transmitted field after the second mirror is simply given by $E_t = t_1 E_{cav}^+$. We can rewrite this expression for the intensity to obtain the airy fonction:

$$I_t = I_{in} \frac{t_0^2 t_1^2}{(1 - r_0 r_1)^2 + 4r_0 r_1 \sin(\frac{\phi}{2})^2} \quad (1.9)$$

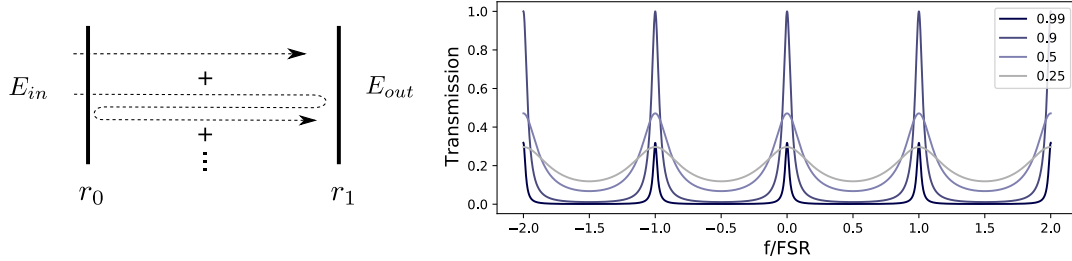


Figure 1.1: Cavity spectrum. Left - The intra cavity field is a buil-up of the transmitted field with an infinite sum of round trip contribution. Right- Spectrum of the cavity when we vary one mirror reflectivity, legend panel, when the second mirror reflectivity is at $r = 0.9$. The frequency is normalized by the Free Spectral Range (FSR) equal to $c/2L$.The cavity transmission is maximal for $r_1 = r_2$ corresponding to an impedance matched cavity where the intput and output amplitude are equal. The increase of reflectivity leads to a refinement of the resonance width.

The cavity spectrum is naturally made of two characteristic frequencies. First, the transmission is a periodic function of the frequency with a period of $\nu_{FSR} = 2L/c$ called Free Spectral Range (FSR). Here $1/\nu_{FSR}$ is the time taken by light to make a round-trip. When the reflectivity of the two mirrors is close to one, the sinus function can be approximated by its first order development close to a resonance. We recover a Lorentzian shape with a frequency full-width a half maximum given by :

$$\delta_f = \frac{\nu_{FSR}}{\pi} \frac{1 - r_0 r_1}{\sqrt{r_0 r_1}} \quad (1.10)$$

Because we have a Lorentzian, the lifetime of photons inside the cavity is $\tau = 1/(2\pi\delta_f)$ and the photon rate is $K = 2\pi\delta_f$. The ratio between those two frequency ranges is called the finesse of the resonator. It characterizes how well resolved is a resonance. In our example, the finesse is :

$$\mathcal{F} = \frac{\nu_{FSR}}{\delta_f} = \pi \frac{\sqrt{r_0 r_1}}{1 - r_0 r_1} \quad (1.11)$$

Another interpretation of the finesse is the ratio between the lifetime of a photon and the duration of a round-trip. The finesse is thus the number of round-trips inside the resonator N up to a factor 2π : $\mathcal{F} = 2\pi N$.

Coupling the cavity to a dielectric medium

Now that we have the spectrum of an empty cavity, we can look at the spectrum in the presence of a thin dielectric medium characterized by a complex reflective index $n(\omega)$ and a length l_0 . The refractive index capture the response of the medium to an external electromagnetic field through its polarization $P = \chi\epsilon_0 E$ with the relation $\chi = n^2 - 1$. Starting from equation (1.8) we only have to change the accumulated phase by $\phi' = \omega 2(L - l_0)/c + \omega 2n(\omega)2l_0/c = \phi + \omega(n(\omega) - 1)2l_0/c$. There are two effects on the spectrum, first the real part of the refractive index shift the resonance of the empty cavity. The imaginary component corresponds to absorption of light and leads to a decrease of the transmission. In the limit $2\omega/cl_0|(n-1)| \ll 1$, the transmission is approximately :

$$T = \frac{I_t}{I_{in}} = \frac{t_0^2 t_1^2}{(1 + r_0 r_1 2k l_0 \text{Im}(n))^2 + 4r_0 r_1 \sin(\frac{\phi}{2} + k l_0 (\text{Re}(n) - 1))^2} \quad (1.12)$$

Let's take the simple example of

1.2.2 Quantum treatment for two levels atoms

To obtain a more accurate description of the atoms-cavity system one need to consider a full quantum treatment of the problem. On one hand, atoms are seen as quantum object simplified here to a collection of two level systems made of the ground state $|g\rangle$ and the excited state $|e\rangle$ and on the other hand, the light is also described by quantum mechanics using the second quantification to introduce creation a^\dagger and annihilation a operators.

Field quantization and coherent driving

If we assume that light propagates in the TEM₀₀ of the cavity with a waist w and a length ℓ , the electric field operator obtained by the second quantification reads :ATTENTION IL Y A ERREUR DANS LA NORMALISATION E cf chap4

$$\hat{E}_c(r, z) = \sqrt{\frac{\hbar\omega}{2\epsilon_0 V}} e^{-r^2/w^2} (\hat{a}^\dagger(z) + \hat{a}(z)) \quad (1.13)$$

Where ω is the light frequency, ϵ_0 the vacuum permittivity, $\hat{a}(z) = \hat{a}(0)e^{ikz}$ and $\hat{a}^\dagger(z) = \hat{a}^\dagger(0)e^{-ikz}$ annihilation and creation operator at position z . Finally, $V=\frac{\pi}{2}w^2\ell$ is the volume associated to the mode to ensure that we recover the energy :

$$\frac{\epsilon_0\ell}{2} \int \langle E_c^2(r) \rangle 2\pi r dr = \hbar\omega(n + 1/2) \quad (1.14)$$

Now that we have the expression of the field inside the resonator we must take into account an external bath that feeds the cavity from a given mirror of transmission T which defines a field feeding rate $\kappa_0 = cT/2\ell$. The operator describing the driving of the cavity by a external coherent states $|\alpha\rangle$ is then :

$$\hat{F}/\hbar = i\alpha\sqrt{2\kappa_0}(\hat{a}^\dagger e^{-i\omega t} - \hat{a}e^{i\omega t}) \quad (1.15)$$

The Hamiltonian of the quantum field is $\hat{H}_f = \hbar\omega a^\dagger a + \hat{F}$ and the dynamics of the density matrix $\hat{\rho}$ is obtained with the master equation :

$$\hbar \frac{d\hat{\rho}}{dt} = i[\hat{\rho}, \hat{H}_f] + \mathcal{L}_f[\hat{\rho}] \quad (1.16)$$

Where the Lindblad operator \mathcal{L}_f is here to consider leaks of photons out of the cavity. This comes from defects of our mirrors summarized in a coefficient L or equivalently in a field damping rate $\kappa = cL/2\ell$ taking into account all losses. This operator reads :

$$\mathcal{L}_f[\hat{\rho}] = \hbar\kappa(2\hat{a}\hat{\rho}\hat{a}^\dagger - \{\hat{n}, \hat{\rho}\}) \quad (1.17)$$

Atoms inside the resonator : Rabi Splitting

The second step consists in a quantum description of our atoms and the light-matter interaction. The interaction Hamiltonian is $H_{int} = -\hat{\mathbf{d}} \cdot \hat{\mathbf{E}}$ valid in the limit of the dipole approximation where it is assumed that the wavelength λ is much greater than the typical size of our atom. The Hamiltonian describing the light matter interaction plus the energy of the cloud is thus :

$$\hat{H}_a/\hbar = \sum_i^N \omega_e \hat{\sigma}_{ee}^{(i)} + g_i(\hat{a}^\dagger + \hat{a})(\hat{\sigma}_{eg}^{(i)} + \hat{\sigma}_{ge}^{(i)}) \quad (1.18)$$

Again, we need to take into account an external bath coupled to our system, here to obtain the decay from the excited state at a field damping rate γ :

$$\mathcal{L}_a[\hat{\rho}] = \hbar\gamma \sum_i^N (2\hat{\sigma}_{ge}^{(i)}\hat{\rho}\hat{\sigma}_{eg}^{(i)} - \{\hat{\sigma}_{ee}^{(i)}, \hat{\rho}\}) \quad (1.19)$$

and the full dynamics of the system atoms-light inside the resonator is obtain by

$$\hbar \frac{d\hat{\rho}}{dt} = i[\hat{\rho}, \hat{H}_a + \hat{H}_f] + \mathcal{L}[\hat{\rho}] \quad (1.20)$$

By making slowly varying field approximation in the rotating frame and looking at the steady state, one can infer the transmission of the cavity in the presence of atoms :

$$T = T_0 \frac{1}{(1 + \frac{2C}{1+\delta_e^2/\gamma^2})^2 + (\delta_c/\kappa - \delta_e/\gamma \frac{2C}{(1+\delta_e^2/\gamma^2)^2})^2} \quad (1.21)$$

Where $\delta_e = \omega - \omega_e$, $\delta_c = \omega - \omega_c$ and $C = \sum_i g_i^2/(2\gamma\kappa)$ the cooperativity characterizing the coupling between atoms and the field inside the resonator. From this last equation, one recover the vacuum rabi splitting as we see two peaks in the presence of atoms compare to the empty cavity case, see figure 1.2.

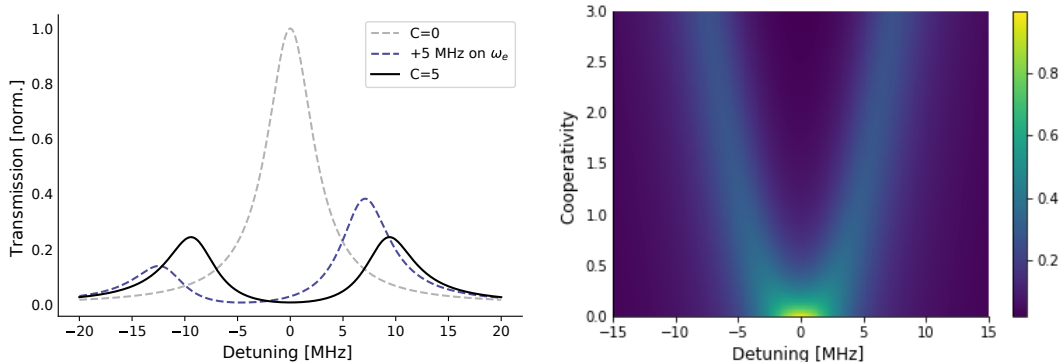


Figure 1.2: Rabi Splitting. Left- Spectrum of the cavity in several configuration with $\omega_c = \omega_e$, $\gamma = 2\pi \times 3$ MHz, $\kappa = 2\pi \times 2.7$ MHz. First without atoms in grey, we obtain one resonance of the cavity. When we put atoms with $C=5$, curve in black, we see that the strong absorption destroy the transmission at zero detuning while two peaks appears at ± 10 MHz. The last curve is an illustration of the splitting when $\omega_c \neq \omega_e$. Right- Transmission of the cavity as a function of the cooperativity and the laser detuning.

1.2.3 Electromagnetically induced transparency

In the previous subsection, we have seen the coupling of an ensemble of two level systems with a resonator. One step further is to consider now a third level to our atoms that will enable us to restore transparency in a narrow window of the cavity-atoms spectrum thanks to electromagnetically induced transparency.

Free space and dark state of the Hamiltonian

Let's first look at a free-space configuration to understand the underling process going on in electromagnetically induced transparency. We now look at atoms as three level systems made of a ground state $|g\rangle$, an excited state $|e\rangle$ and an third state $|f\rangle$. This feature is often

introduced in a lambda scheme, i.e. with a state $|f\rangle$ in a ground state of our atom. In fact the only requirement is to have a state with a lifetime much more important than the excited state $|e\rangle$. In our experiment, we work with a ladder scheme with a Rydberg state as a third state to induce a transparency window. To obtain this transparency, a weak probe is sent to address the $|g\rangle$ to $|e\rangle$ line while a strong field, called control field, is close to resonance with the transition between state $|e\rangle$ and $|f\rangle$. The Hamiltonian of the system is then :

$$\hat{H}/\hbar = \sum_i^N \omega_e \hat{\sigma}_{ee}^{(i)} + \omega_f \hat{\sigma}_{ff}^{(i)} - \Omega_p \cos(\omega_p t) (\hat{\sigma}_{eg}^{(i)} + \hat{\sigma}_{ge}^{(i)}) - \Omega_c \cos(\omega_c t) (\hat{\sigma}_{ef}^{(i)} + \hat{\sigma}_{fe}^{(i)}) \quad (1.22)$$

By making again the appropriate rotating wave approximation in the rotating frame, one obtain :

$$\hat{H}_{EIT}/\hbar = \sum_i^N \delta_e \hat{\sigma}_{ee}^{(i)} + \delta_f \hat{\sigma}_{ff}^{(i)} - \Omega_p (\hat{\sigma}_{eg}^{(i)} + \hat{\sigma}_{ge}^{(i)}) - \Omega_c (\hat{\sigma}_{ef}^{(i)} + \hat{\sigma}_{fe}^{(i)}) \quad (1.23)$$

where $\delta_e = \omega_e - \omega_p$ and $\delta_f = \omega_f - \omega_c$. For a given atom, the hamiltonian reads :

$$H^{(i)}/\hbar = \begin{pmatrix} 0 & -\Omega_p & 0 \\ -\Omega_p & \delta_p & -\Omega_c \\ 0 & -\Omega_c & \delta_c \end{pmatrix} \quad (1.24)$$

If now we look for a dark state $|\psi\rangle = a|g\rangle + b|e\rangle + c|f\rangle$ of this Hamiltonian $H^{(i)}$, we obtain $b = 0$, and $a = \sin(\theta)$, $b = \cos(\theta)$ where θ is given by $\tan(\theta) = -\Omega_c/\Omega_p$. Of course, I do not have consider here the decoherence but it gives a correct insight of the concept of electromagnetically induced transparency. The finite lifetime of the $|f\rangle$ states

Transmission spectrum

In presence of a resonator, electromagnetically induced transparency restore the transmission of light in a narrow window. To obtain the spectrum of the cavity with a three level scheme, we have to add the coupling between atoms and the control beam to the Hamiltonian describing the two-level case.

$$\hat{H}_{EIT}/\hbar = \sum_i^N \delta_f \hat{\sigma}_{ff}^{(i)} - \Omega_c (\hat{\sigma}_{ef}^{(i)} + \hat{\sigma}_{fe}^{(i)}) \quad (1.25)$$

and take into account losses from the third state $|f\rangle$:

$$\mathcal{L}_f[\hat{\rho}] = \hbar \gamma_f \sum_i^N (2\hat{\sigma}_{gf}^{(i)} \hat{\rho} \hat{\sigma}_{fg}^{(i)} - \{\hat{\sigma}_{ff}^{(i)}, \hat{\rho}\}) \quad (1.26)$$

To obtain the response of the system in the steady state, one can consider collective operators :

$$\hat{S} = \frac{1}{g_{eff}} \sum_i g_i \sigma_{ge}^{(i)} \quad (1.27)$$

$$\hat{P} = \frac{1}{g\Omega_{eff}} \sum_i g_i \Omega_i \sigma_{gf}^{(i)} \quad (1.28)$$

1.3 Effective interactions between optical photons

$$t = \frac{\gamma_c}{\delta_c - \sum_i \frac{g_i^2}{\delta_e - \frac{\Omega_i^2}{4\delta_r}}} \quad (1.29)$$

$$r = 1 - 2 \frac{T}{L} \frac{\gamma_c}{\delta_c - \sum_i \frac{g_i^2}{\delta_e - \frac{\Omega_i^2}{4\delta_r}}} \quad (1.30)$$

in the limit $\delta_r \delta_c$ small in front of Ω_i^2 , we have

$$t = \frac{\gamma_c}{\delta_c + \delta_r \sum_i \frac{4g_i^2}{\Omega_i^2}} \quad (1.31)$$

at res :

$$\gamma_{EIT} = \frac{\gamma_c + \sum_i \frac{4g_i^2}{\Omega_i^2} \gamma_r}{1 + \sum_i \frac{4g_i^2}{\Omega_i^2}} \quad (1.32)$$

$$t_{max} = \frac{\gamma_c}{\gamma_c + \gamma_r \sum_i \frac{4g_i^2}{\Omega_i^2}} \quad (1.33)$$

1.3.1 Blockade picture

1.3.2 Low-loss interactions

small cloud response

possible protocol

1.3.3 Outlook : Intra-cavity interaction

Contact interaction

br : Rydberg atoms are highly excited atoms characterized by a great principal quantum number n . This properties makes the spectrum of Rydberg atoms close to Hydrogen with a simple structure. The associated lifetime in such highly excited state are greatly enhanced compared to first excited states making them very interesting with a narrow spectral linewidth. Those state are very sensitive to external field which makes them good for precise measurement and metrological applications. For instance, Serge Haroche and his teams took advantage of the sensitivity of Rydberg state to microwave field to count photons inside a cavity without destroying them (Quantum Non-Demolition measurement of light). In addition, a Rydberg state has a strong polarizability that induces strong van der walls interactions between Rydberg atoms that is widely study those day as it can be very fruitful for nonlinear quantum optics. Historically, the name of Rydberg come from the physicist Johannes Rydberg who studied hydrogen spectral line and discovered in 1885 what is now called the Rydberg formula for Hydrogen atoms :

$$\frac{1}{\lambda} = R_0 \left(\frac{1}{n^2} - \frac{1}{n'^2} \right) \quad (1.34)$$

Where λ is the wavelength of the light, $n' > n$ two integers and $R_0 = ??$ the Rydberg constant.

Chapter 2

Presentation of the experimental setup

Contents

2.1 Experimental platform	16
Ultra-high vacuum	17
Assembly and overview	17
2.1.1 Science cavity	18
Reflectivity of the cavity	19
Optical modes of a twisted cavity	21
Cavity length locking	24
2.1.2 Build-up cavities	24
Confocal cavities	24
Presentation of the two resonators	25
Build-up factors	26
2.2 Laser bench	27
2.2.1 Lasers	27
DL pro and TA pro	27
Titanium-Sapphire Laser and External Cavity Doubler	28
High Power 1064 nm fiber laser	29
2.2.2 Frequency locking chain	29
Methods	29
Ultra-stable cavity and Transfer cavity	30
2.3 Control setup	33
2.3.1 Hardware	33
2.3.2 Software	34

In this chapter, we go into the details of the experimental platform and the technical means employed to perform experiments with Rydberg atoms in an optical cavity, as it was introduced in Chapter 1. The atomic source and atomic setup will be discussed in more detail in the next chapter. The first section is devoted to the components of the main vacuum chamber. We first describe the protocol used for the assembly of the experimental platform.

Furthermore, we highlight and discuss the main constraints such as vacuum quality, electric field control, versatility, etc. We then focus on the twisted science cavity. Several aspects of the resonator are discussed among which the geometry of the cavity and its reflectivity. Then, the two build-up cavities for 474-480 nm are presented and characterized with the aim to improve Rydberg Electromagnetically Induced Transparency. The following section describes our lasers and the locking chain employed to stabilize the frequency of our cavities and lasers. This is an important step to precisely address Rydberg atoms because of their narrow spectral linewidth, about 2 kHz at $n = 100$ ⁽¹⁾. Finally, control of the experiment, data acquisitions and related graphical user interface is covered in the last section of this chapter.

2.1 Experimental platform

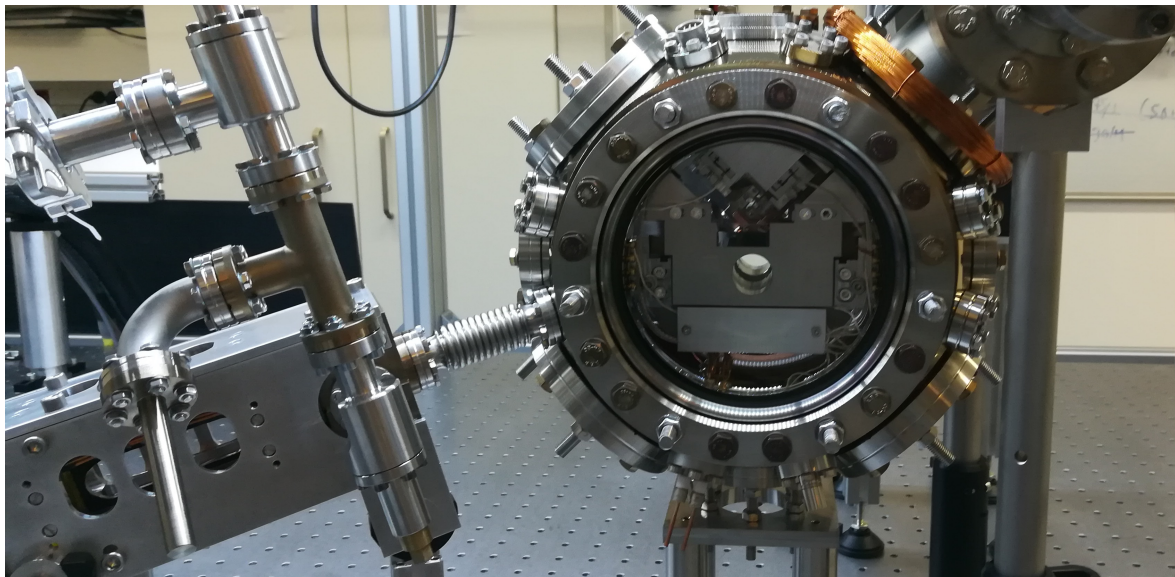


Figure 2.1: Rydberg vacuum chamber. The 2D MOT (our source of atoms, on the left) is linked to the main vacuum chamber (cylinder shaped) where experiments are carried out. The photography was taken right after the assembly, therefore the platform was still at ambient pressure.

Trapped cold atomic ensemble is a fragile tool impossible to observe at ambient pressure because of collisions with other atomic species present in the environment. When building this kind of experiment, the very first issue is to reach an ultra-high vacuum regime⁽²⁾ to significantly suppress collisions and increase the lifetime of the atomic cloud. The experiment is thus surrounded by a cylinder vacuum chamber made of stainless steel (316 L) with a 10 cm radius and a length of 15 cm, see figure 2.1. This vacuum enclosure is linked to an ion pump (Agilent VacIon Plus 55 Pump, 55L/s) and a Non-evaporable getter (SAES CapaciTorr Z100) to maintain the pressure level. The chamber is also connected to the source of atoms, the two dimensional Magneto-optical trap (2DMOT) through a 1 μm radius hole. This geometry induces a differential pressure between the two parts of the experiment and protects the vacuum inside the main chamber from the 2DMOT where the hot rubidium vapor is located. This section focuses on the inside of the main vacuum chamber. Before going into the details of the platform, it is worth mentioning that putting the overall system under high vacuum requires some precautions.

⁽¹⁾ 100S state at room temperature, estimated from ARC calculator [1].

⁽²⁾ Pressure below 1×10^{-8} mbar.

Ultra-high vacuum

In the low pressure regime, vacuum is limited by outgassing processes hence the cruciality of the choice of materials [2]. This is well documented by LIGO Scientific Collaboration, where they tested a huge amount of materials for ultra-high vacuum. They also provide their cleaning protocol for each component [3]. As an example, we give our cleaning process for one of the most sensitive materials inside the vacuum chamber:

Viton (synthetic rubber) : The first stage is a rough cleaning to remove most of the grease and oil with wipes. It is then repeated in a bath of hot water mixed with Liquinox detergent to help scrub surfaces. It is followed by an ultrasonic bath in Liquinox to remove inaccessible dirt. Viton parts are then put into a pressure cook with deionized water at 15 psi during 2 hours. This cooking is repeated four times interspersed by a rinsing step with deionized water. The last step consists in a bake at 120 °C during 48 hours. In practice, the bake was repeated until no deposits were visible in the test chamber. We cleaned parts with wipes and an ultrasonic bath before restarting a bake.

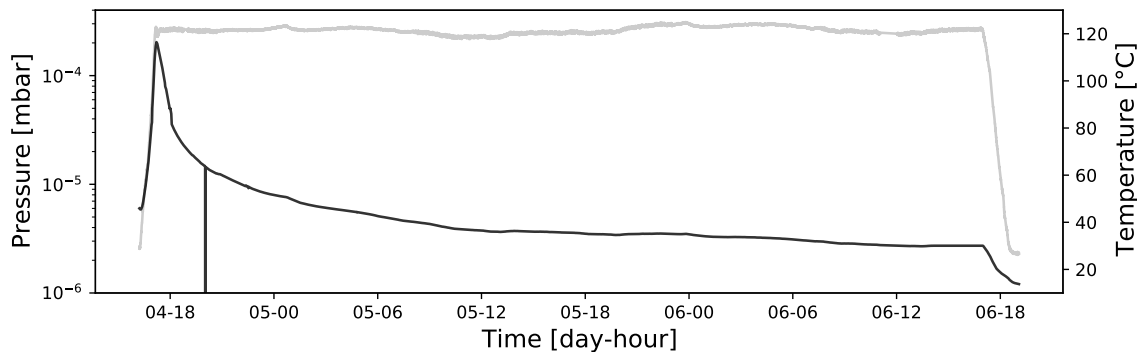


Figure 2.2: Bake of Viton. An example of baking during 48 hours with Viton parts. In black the pressure monitored by the turbo pump and in grey the temperature measured on the bake chamber with a thermo sensor. We observe a 6-fold decrease of the pressure after the bake.

This protocol is adapted to each part, from electrical wires to the main vacuum chamber itself. The vacuum inside the chamber was achieved by a turbo pump coupled to a primary pump (Pfeiffer Pumping Station TSH 071E) to go from ambient pressure to ultra-high vacuum. One final bake of the entire platform was carried out during 2 weeks to reach the current 2.10^{-9} mbar pressure inside the main vacuum chamber. Once the desired pressure had been reached, an ionic pump took over in the long term to avoid the important mechanical vibrations of the primary pump.

Assembly and overview

The science platform can be split in three parts, from bottom to top: the magneto-optical trap coils support, the blue cavities holder and the science cavity support, see figure 2.3. Those three supports are stacked one on top of the other separated by small Viton cylinders ($r=2$ mm, $l=10$ mm) to stabilize them. The Viton pieces ensure the thermal and mechanical isolation of the setup. The whole platform lies on the MOT coils support which is hung on the main vacuum chamber by four grabbers. Each support is made of stainless steel (316 L) to avoid magnetization as it is the case for the chamber itself.

The science cavity is a four mirror twisted resonator with a tunable geometry. The position of two mirrors can be adjusted independently by two translation stages (more about it the following section). Two +50 mm aspheric lenses are attached on top of this support with

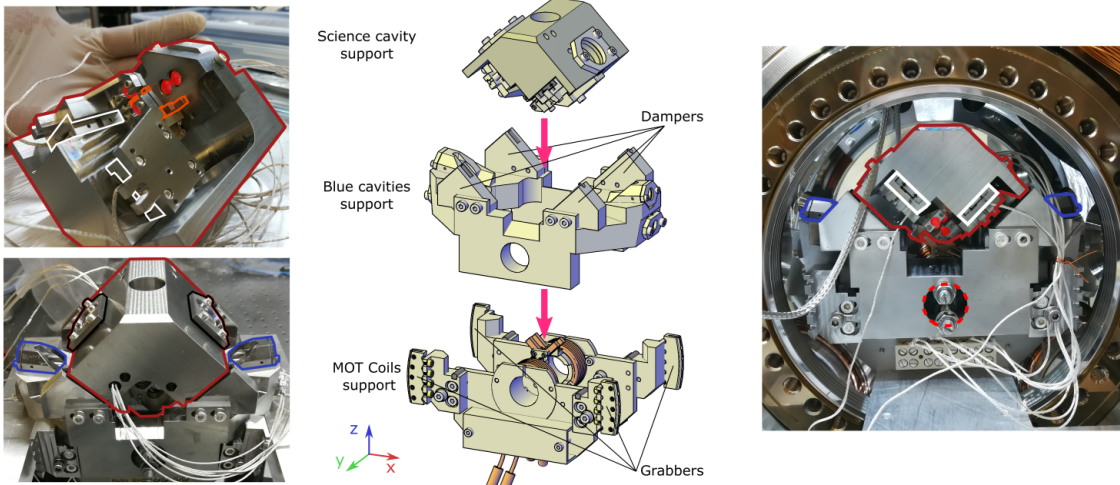


Figure 2.3: Rydberg platform assembly. Top left- Science cavity and its four mirrors are in red, electrodes are circled in orange, translation stages and science cavity support are respectively circled in white and red. Notice that in the top left image, science cavity support is upside-down for alignment tests. Down left- On top of the science support, circled in red, two +50 mm achromatic lenses are attached, circled in black, and the two blue cavity high-reflectivity mirrors are circled in blue on their own support. Right- the science platform inside the vacuum chamber, the dashed red circle is the entrance of the horizontal MOT beam where atoms are located before transport to the cavity. Center - drawings of the three parts, spaced for clarity. As described in the text, the science support lies on the blue cavities supports via Dampers and then the whole is placed on the MOT coils support fixed to the chamber.

a 0.24 numerical aperture in order to trap atoms over short distances ($\approx 10 \mu\text{m}$) and to make a high resolution characterization of the cloud. For instance, the number of atoms or the temperature can be measured by means of the absorption imaging technique detailed in chapter 3. The other main component of the setup is the pair of blue cavities to amplify the power of our blue control beams to address Rydberg states at the science cavity level. Control of the size and position of the beam inside both resonators is made possible by the confocal geometry, see 2.1.2 Confocal cavities. Steering of electrical components such as piezoelectric actuators for cavities or MOT coils are carried out by feedthroughs placed at the top and at the bottom of the vacuum chamber. Wires were insulated by a metal sheath to prevent the spread of electrical fields. This is a critical parameter to control when dealing with high Rydberg states because of their high polarizability scaling as $n^{7(3)}$. In addition, some shielding was added in front of the mirror support containing piezoelectric actuators and 8 electrodes were placed in the middle of the science cavity to further control electrical fields during the experiment.

2.1.1 Science cavity

The science cavity, also called optical cavity, is at the heart of the Rydberg platform to shape interactions between optical photons. In the context of Rydberg blockade, at least two regimes are interesting to investigate. The first one converts dissipation inside the cavity into a photonic dispersive response outside of it. This effect translates into a phase shift interaction between photons. The other regime corresponds to intra-cavity photons interactions where several excitations are propagating through the resonator. Both of them rely on the ability to have a beam size of the order of the blockade sphere or smaller inside the

⁽³⁾Here n is the principal quantum number.

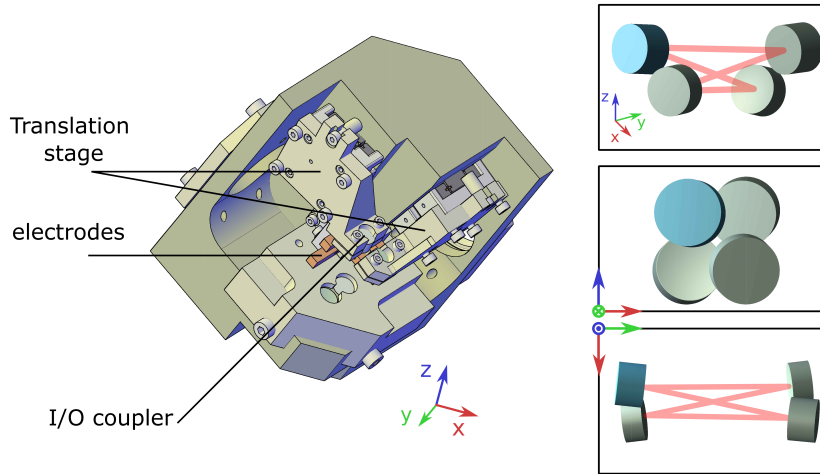


Figure 2.4: Twisted cavity. Left- Science cavity support. The four-mirror cavity is visible in the center of its support. Two mirrors are attached to two translation stages to adjust the length of the resonator and four electrodes are visible in the middle of the resonator to control electrical fields. Right- Science cavity. The Input/Output mirror is visible in Light blue and high-reflectivity mirrors is colored in grey. Mirrors are approximately 21 mm apart along the y axis and the incident angle of light on a mirror is about 9.3° .

resonator. In practice, it is hard to go far beyond $n = 100$ for the Rydberg state because ionization becomes non-negligible (ionization energy about $\hbar \times 350$ GHz). This limit sets the waist⁽⁴⁾ of our optical resonator to 21 μm . A small waist can be achieved with a standard two-mirror cavity, but at the cost of a short resonator length. For instance, Gerhard Rempe's team works on similar topics with a single atom coupled to a high-finesse resonator [4]. Their cavity has a 30 μm waist but a length of 500 μm [5]. In particular, it leads to dielectric media (mirrors) close to the cloud which is very problematic with Rydberg states because of their high polarizability [6, 7, 8]. The best way to extend the resonator length while preserving a small waist is to consider a bow-tie resonator. Planar configurations are prone to strong astigmatism. It is then better to consider a non-planar geometry for the cavity to counter this effect as it is discussed in the next section.

Our resonator is thus a four mirror twisted cavity composed of two planar mirrors in its upper part plus two concave mirrors in the lower part both with a 20 mm radius, see figure 2.4. One obvious advantage of such a geometry is the running-wave configuration that circumvents several issues of standing-wave cavities, for instance field inhomogeneities on the atomic ensemble. Mirrors are separated by a 21 mm distance along y axis and the angle of incidence on a mirror is approximately 9.3° . This distance is not fixed and can be adjusted independently over ± 3 mm with two independent translation stages placed on the input/output mirror side ($y < 0$). This flexibility combined with the non-planar geometry allows to reach several kinds of mode degeneracies.

Reflectivity of the cavity

We aim at coupling light to a cloud of rubidium and extracting as many photons as possible out of it. The best configuration is to consider a one-end cavity, i.e. a resonator with one input/output mirror of transmission T much more important than for the others mirrors. In

⁽⁴⁾Half width at $1/e^2$ of the intensity.

this configuration, the resonator reflection coefficient at resonance is given by:

$$r_{cav} = \frac{E_{out}}{E_{in}} = \frac{\sqrt{1 - L_0} - \sqrt{1 - T}}{1 - \sqrt{(1 - T)(1 - L_0)}} \approx \frac{T - L_0}{T + L_0} \text{ in the limit } T, L_0 \ll 1 \quad (2.1)$$

where L_0 is the total resonator losses taking into account the losses of each mirror. More precisely, the term L_0 encompasses different kinds of losses:

- **Absorption:** Light always propagates over a small distance inside a Bragg mirror. This propagation in the material induces a weak light absorption. This effect is probably one of the dominant sources of optical loss in our resonator.
- **Diffusion:** Diffuse reflections on the mirror are possible because of nano-metric defects on the surface. Our supplier guarantees a RMS roughness of $\sigma = 1.5 \text{ \AA}$ for our mirrors. In terms of losses it is approximately $L_d \approx (4\pi\sigma/\lambda)^2 \approx 6 \text{ ppm}$ ⁽⁵⁾.
- **Mirror size:** This term is a geometric factor taking into account the spatial cut-off caused by the finite size of our mirrors. This loss factor depends on the specific mode, it is completely negligible for the fundamental mode of our cavity as it is given by $L_{\text{cut-off}} = e^{-d^2/(2w^2)}$ where d is the mirror diameter ($\sim 6 \text{ mm}$) and w is the waist. However, this term could become visible for high order modes described in 2.1.1 Optical modes of a twisted cavity.

We estimated the sum of losses to be $L_0 \approx 300 \text{ ppm}$ before the bake of the entire platform. As previously mentioned, one option towards effective interactions between photons is to use dissipation inside the cavity to induce a dispersive response outside of it. This can be understood by adding a term to L_0 to take into account losses induced by the presence of atoms inside the resonator.

Without atoms, the system is such that the total losses are just the intrinsic losses of the cavity $L_0 \ll T \ll 1$. In this case, the reflectivity of the system is simply given by $|r_{cav}|^2 \approx 1 - 4L_0/T = R_0$.

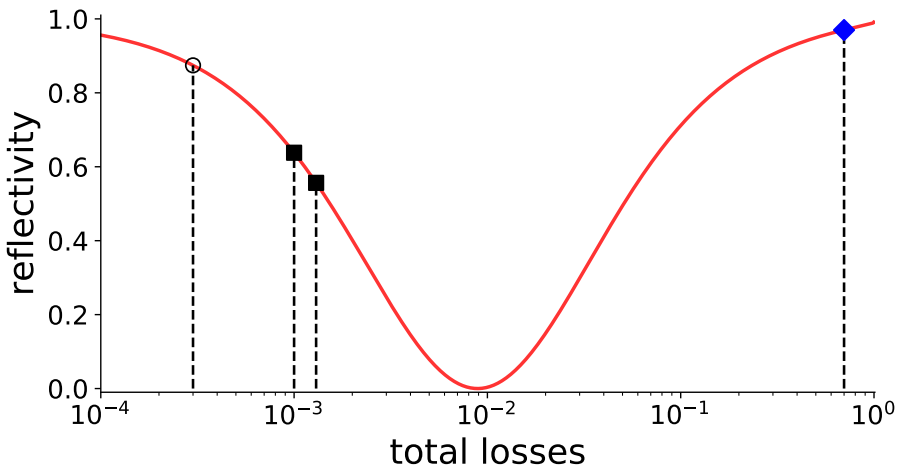


Figure 2.5: Losses. Reflectivity $|r_{cav}|^2$ is plotted for $T=0.90\%$ as a function of the total losses L_0 (red curve). $L_0 = 300 \text{ ppm}$ (black circle) are the total losses before degradation. Current level: $L_0 = 1000 \text{ ppm}$ at 795 nm and $L_0 = 1300 \text{ ppm}$ at 780 nm (dark square) give respectively $R_{795} = 0.64$ and $R_{780} = 0.55$, see text. The phase of the beam is π -shifted when the point $L_0 = T$ is crossed. The reflectivity for a small blockaded ensemble ($L = 70\%$, in blue) is $|r_{cav}|^2 = 0.97$, see text.

⁽⁵⁾Part per million, 10^{-6} . Those losses are calculated at 780 nm.

In a strongly dissipative regime, atomic losses are much more important than T such that the reflectivity goes asymptotically to $|r_{cav}|^2 = 1 - T = R$. The phase of the field is then π -shifted with respect to the initial case. We see here one role of the transmission coefficient. The rate at which photons leave the cavity is also set by the transmission of the input/output mirror: $K = cT/\ell = 2\kappa$ where ℓ is the roundtrip distance. It accordingly affects the value of the cooperativity, $C = g^2/(\kappa\gamma)$, for the coupling with rubidium atoms. Therefore, the value of the transmission (T) is a trade-off between several quantities. First, the need to have a low loss system to reach high fidelity for our interaction scheme, meaning $L_0 \ll T \ll 1$. Moreover, a fast response of the system, particularly interesting for quantum communication aspects and finally, a high cooperativity $C \gg 1$. A good compromise is to set the value of the photon rate close to the decay rate of rubidium 87 D lines $\Gamma = 2\pi \times 6.065 \text{ MHz}$ ⁽⁶⁾ such that $T \approx \Gamma\ell/c \approx 10^{-2}$. In practice, we estimated the transmission parameter of our cavity to be $T = 0.90\%$ ⁽⁷⁾, giving $R_0 = 90\%$ and $R = 99\%$. The cavity reflectivity is plotted with this value as a function of losses in figure 2.5. The coating made by Laseroptik is optimized at 780 nm and 795 nm⁽⁸⁾, where experiments are carried out, but also at 1064 nm to lock the cavity length, see 2.1.1 Cavity length locking. More precisely, mirror coatings are alternations of Ta_2O_5 and SiO_2 with one last SiO_2 layer to prevent vacuum degradation due to oxygen depletion [9]. The transmission parameter T also sets the value of other quantities such as the finesse of the cavity. In the limit $L_0, T \ll 1$, the finesse is approximately given by $F = 2\pi/(T + L_0) = 675$ at 795 nm.

Finally, we can estimate the reflectivity in the presence of a small blockaded rubidium cloud to verify that 0.90% of transmission is not too important. We take a Gaussian RMS of $\sigma_c = 5 \mu\text{m}$ for our cloud to fit inside a Rydberg blockade sphere for the 100S state⁽⁹⁾ and a typical peak atomic density of $n_0 = 5 \times 10^{11} \text{ cm}^{-3}$. The optical depth is $OD = n_0 \sqrt{2\pi\sigma_c\sigma}$ with the rubidium cross section $\sigma \simeq 2 \times 10^{-9} \text{ cm}^{-2}$. It gives $L_{at} = 1 - \exp(-OD) \approx 0.7 \gg T$ and corresponds to $r_{cav}^2 \approx 97\%$.

The value of L_0 is critical to have high-fidelity photonic interactions. This is one of the main issue for cavity QED with single atoms because losses induced by a single atom have to be much more important than the transmission. It means going to very low transmission for the I/O coupler in the high-finesse regime. In this case, reducing the intrinsic losses is a challenging task [4]. After we started to run experiments with atoms, we observed a decrease of the finesse that we attribute to a rubidium deposit on our mirrors. The finesse is now 620 at 780 nm and 590 at 795 nm. We estimated the value of L_0 to be now ~ 1000 ppm at 795 nm and ~ 1000 ppm at 780 nm. With this change, the reflectivity for an empty cavity is now 64% at 795 nm. We did not focus yet on this problem but we did not manage to get rid of it with UV light. The next step is probably to heat the structure close to the mirrors.

Optical modes of a twisted cavity

We will now discuss the propagation of light through our four-mirror twisted resonator to find the optical modes. Let us limit ourselves to the study of monochromatic beams propagating along \mathbf{z} so that in the appropriate basis, the field can be written as $\mathbf{E}(x, y, z) = E_0(x, y, z)e^{i(wt - kz)}\mathbf{e}$ where \mathbf{e} is the polarization vector orthogonal to \mathbf{z} . We will further assume that the envelope E_0 slowly varies with z compared to the exponential term. In this limit, also called paraxial approximation, the scalar wave equation $(\nabla^2 + 2k^2)E(x, y, z) = 0$

⁽⁶⁾Full width at half maximum of the D_2 line. For the D_1 line: $\Gamma = 2\pi \times 5.746 \text{ MHz}$.

⁽⁷⁾0.89% at 780 and 0.91% at 795 nm.

⁽⁸⁾We work with the cavity locked on a hyperfine transition from one of the rubidium 87 fine doublet: $D_1, 5S_{1/2} \rightarrow 5P_{1/2}$ at 795 nm and $D_2, 5S_{1/2} \rightarrow 5P_{3/2}$ at 780 nm.

⁽⁹⁾At $n=100$, the blockade radius is about $R=16 \mu\text{m}$ for a linewidth of $\gamma = 3 \text{ MHz}$, $R = (C_6/\gamma)^{1/6}$.

becomes :

$$\frac{1}{2k} \nabla_{\perp}^2 E_0(x, y, z) = i \frac{\partial}{\partial z} E_0(x, y, z) \quad (2.2)$$

This expression is valid for a homogeneous and isotropic dielectric medium. Several orthogonal bases exist to compute a general solution of this equation. In a planar running-wave cavity, we must take into account non-normal reflection on mirrors. For a spherical mirror of focal length f making an angle θ with an incident light beam, the effective focal length is different along the tangential ($f \cos(\theta)$) and sagittal ($f / \cos(\theta)$) directions. Adding a second spherical mirror in a planar cavity can only worsen this astigmatism. Therefore, the mode factorizes into a Hermit-Gauss mode of the sagittal variable and another of the tangential variable. On the contrary, this effect can be suppressed by twisting the resonator out of the plane with two curved mirrors. In this case, the astigmatism induced by the first curved mirror can be compensated by the second one [10, 11, 12]. We are then looking for a set of modes that preserves the cylindrical symmetry [13]. The natural basis which has this symmetry is given by the Laguerre-Gaussian modes (shown in figure 2.6). Its formal expression is:

$$u_{l,n}(r, \phi, z) = C_0 \frac{w_0}{w(z)} \left(\frac{r \sqrt{(2)}}{w(z)} \right)^{|l|} L_n^{|l|} \left(\frac{2r^2}{w(z)^2} \right) e^{-\frac{r^2}{w(z)^2}} e^{-\frac{ikl^2}{R(z)^2}} e^{i(l\phi + \psi(z))} e^{ikz} \quad (2.3)$$

where C_0 is a normalization constant, l and n are integers respectively named azimuthal and radial index.

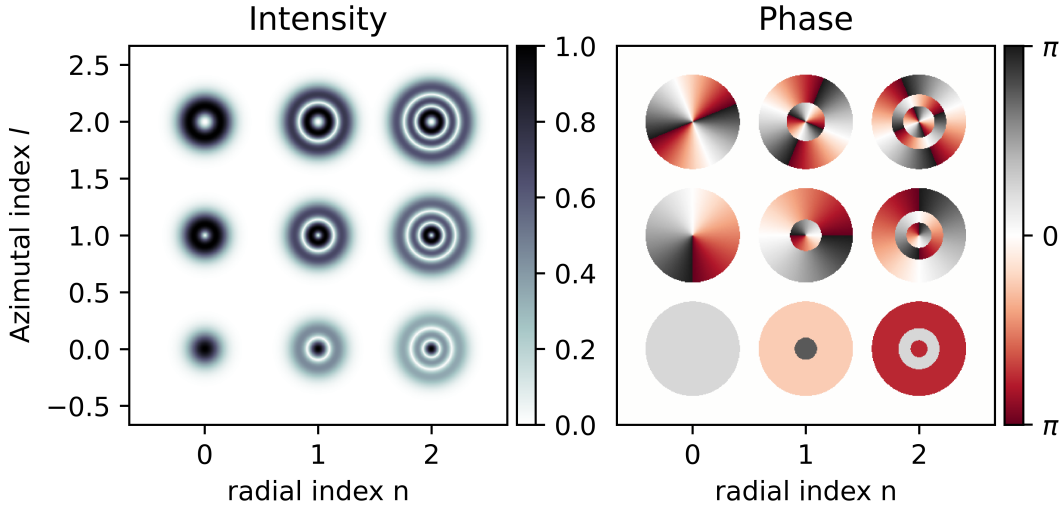


Figure 2.6: Laguerre-Gaussian modes. Intensity (Left) and phase (right) of the LG modes as a function of the azimuthal index l and the radial index n .

$L_n^{|l|}$ is the Generalized Laguerre-Gauss polynomials given by:

$$L_n^{|l|}(t) = \frac{t^{-|l|} e^t}{n!} \frac{d^n}{dt^n} (e^{-t} t^{n+|l|}) \quad (2.4)$$

Along the transverse plane, the beam is characterized by the spot size parameter w :

$$w(z) = w_0 \sqrt{1 + \left(\frac{z - z_0}{z_r} \right)^2} \quad (2.5)$$

The quantity w_0 is called the waist of the beam at position z_0 while $z_r = \pi w_0^2 / \lambda$ is the Rayleigh length. It characterizes the typical distance over which the beam keeps its shape. In addition, a radius of curvature R is associated to the Gaussian mode:

$$R(z) = (z - z_0) \sqrt{1 + \left(\frac{z_r}{z - z_0}\right)^2} \quad (2.6)$$

Finally, the mode is characterized by a Gouy phase ψ :

$$\psi(z) = (1 + |l| + 2n) \arctan\left(\frac{z - z_0}{z_r}\right) \quad (2.7)$$

The fundamental mode, also called TEM_{0,0} for Transverse ElectroMagnetic mode, is a Gaussian fully characterized by two quantities: the waist w_0 and its position z_0 . For practical reason, those two parameters are gathered in a unique complex number $q(z) = (z - z_0) + iz_r$.

The paraxial equation may seem complicated to solve for a given resonator geometry. It is in fact equivalent to a simpler method: ABCD matrix from ray optics [10]. In one dimension, the output position and angle (h_{out}, θ_{out}) is a linear transformation of the input parameters (h_{in}, θ_{in}) for any thin optical element. It is given by what is called an "ABCD" matrix :

$$\begin{pmatrix} h_{out} \\ \theta_{out} \end{pmatrix} = \begin{bmatrix} A & B \\ C & D \end{bmatrix} \begin{pmatrix} h_{in} \\ \theta_{in} \end{pmatrix} \quad (2.8)$$

The propagation of light through the cavity is then fully captured by a matrix M . By generalizing this approach to the two transverse axes, one can compute the eigenmodes of our twisted resonator, with a roundtrip phase:

$$\phi = \frac{2\pi\ell_{rt}}{c} \nu + \left(\frac{1}{2} + m\right) \chi_1 + \left(\frac{1}{2} + l\right) \chi_2 = 2\pi n \quad (2.9)$$

where n, m, l are integers corresponding respectively to the longitudinal and the transverse modes. The twisted geometry induces a rotation of the polarization inside the cavity, shown in figure 2.7. The eigenmodes of our resonator are then circularly polarized Laguerre-Gaussian modes where right and left-handed modes are split [10, 11, 14]. Transverse modes indices m, l are related to right and left circularly polarized modes. Finally, $\chi_{1,2}$ are two parameters taking into account Gouy phase factors and depend on the distance between mirrors. In

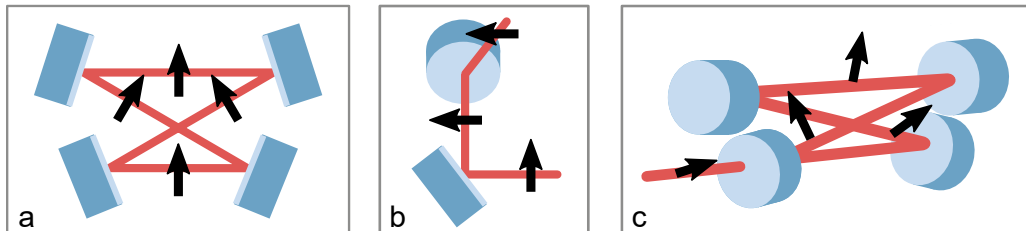


Figure 2.7: Image rotation. Illustration of the image rotation induced by the geometry of the resonator (mirrors are supposed flat here). a- For a planar resonator, the image (black arrow) is not rotating. b- One simple example of image rotation. c- Rotation along the optical path for our four mirrors twisted cavity.

practice, we control the two parameters χ_1, χ_2 through the two Smaract translation stages with a few nanometers resolution⁽¹⁰⁾. Thanks to this high resolution, it is possible to fully

⁽¹⁰⁾Smaract translation stages are based on the stick-slip phenomenon.

control the degeneracy of the transverse modes. Let us consider for instance a configuration such that $\chi_1 = p/q$ where p and q are coprime integers. The mode $u_{l,m,n}$ is resonant if $\nu_{l,m,n} = \frac{2\pi\ell_{rt}}{c}[(\frac{1}{2} + m)\chi_1 + (\frac{1}{2} + l)\chi_2 + 2\pi n]$. We observe that this mode is degenerated with the mode $u_{l,m+qj,n-jp}$ where j is an integer. We have thus a p/q degeneracy between modes $u_{l,m+qj,n+jp}$ for any integer j . This degeneracy has been exploited recently in the group of Jonathan Simon to emulate a 2D gas of electrons in a magnetic field [15, 16].

Cavity length locking

The science platform and supports were designed to reduce as much as possible thermal fluctuations and mechanical vibrations by isolating each support with Viton cylinders as mentioned in the introduction of this section. Despite these precautions, the cavity length is locked to avoid inherent drift caused by slow dynamics. Furthermore, the cavity must be coupled to an atomic transition which is only possible by a control of the cavity length. This is made possible by three piezoelectric actuators placed behind the two mirrors support in front of the input-output mirror (shown in figure 2.3). The feedback voltage is obtained by the standard Pound-Drever-Hall technique (PDH, explained in 2.2.2 Frequency locking chain) where the cavity length is locked on a reference laser. We initially planned to use a far off-resonant 1064 nm laser but we did not manage to keep it stable enough. We then turned to a 783 nm beam much closer to the rubidium lines. We had to reduce its power down to 1 nW in front of the cavity to protect our atoms from interactions with this locking beam. We used a specific Thorlabs APD (430 A/M) for this locking at weak intensity.

2.1.2 Build-up cavities

The dipole matrix elements for the coupling between a low excited state of rubidium ($5P_{1/2}$ or $5P_{3/2}$) and a Rydberg state (nS) are very weak with a scaling in $n^{-3/2}$. For instance, at $n = 100$ and with 1 W focused on a 100 μm waist, the Rabi frequency is only about $2\pi \times 4 \text{ MHz}$ ⁽¹¹⁾. In addition, some of the experimental protocols we aim for require the use of two different Rydberg states. We therefore have two blue lasers (Ti-sapphire laser + External Cavity Doubler from Msquared, see Lasers section), each can at most deliver 1 W and two build-up cavities increase this power. The two resonators were put inside the vacuum chamber to obtain a small waist (about 100 μm) and to ensure a high stability. They are perpendicular to the science cavity optical axis and tilted by 8° with respect to the horizontal axis, shown in figure 2.8.

Confocal cavities

The optimal value of the waist is a trade-off between a high control Rabi frequency and the inhomogeneous broadening induced by the variation of the intensity on the atomic sample. On the other hand, the small atomic sample (few tens of micrometers) must be well coupled to both the science cavity mode (20 μm waist) and our two control beams (about 100 μm). The position of the modes of our cavities and their size are therefore sensitive parameters for our experiment that we have to control to some extent. A confocal cavity is a simple solution to both problems. In this configuration, two mirrors are separated by a distance equal to the radius of curvature of the two mirrors. The confocal ABCD matrix after one round-trip (introduced in the previous section) is simply:

$$M_{\text{confocal}} = \begin{bmatrix} -1 & 0 \\ 0 & -1 \end{bmatrix} \quad (2.10)$$

⁽¹¹⁾The dipole is calculated between $5P_{1/2}, F = 2, m_F = +2$ and the $100S$ Rydberg state with linearly polarized light.

where we notice that $M_{confocal}^2 = 1$. It means that there is no constraint on the beam input angle or initial position. Any mode goes back to its initial configuration after at most two round-trips. Thereby, it is possible to make a fine alignment of the blue beam on the atomic sample to maximize the overlap but also to adjust the size of the beam to optimize the control Rabi frequency. This is even more interesting because it is possible to inject light out of the optical axis of the cavity and thus avoid inhomogeneities caused by a standing-wave configuration. The waist of the $\text{TEM}_{0,0}$ mode is given by $w = \sqrt{\lambda R/\pi}$, consequently $z_r = R$ and the frequency of a resonant mode can be expressed as :

$$\nu_{n,p} = \frac{c}{4R}(2n + m) \quad (2.11)$$

where m is the transverse mode index and n the longitudinal index (both integers).

Presentation of the two resonators

Our blue cavities are single-ended resonators with an Input/Ouput mirror transmission of 1%. The radius of curvature is $R=150\text{ nm}$ giving a free spectral range of 1 GHz and a $\text{TEM}_{0,0}$ waist of $107\text{ }\mu\text{m}$. We call the resonator with the I/O mirror on the left of figure 2.8 the Left cavity and the other one the Right cavity. The finesse of the cavity is estimated from the full width at half maximum of the $\text{TEM}_{0,0}$ mode: $\Gamma_{Right} = 2\pi \times 2.4\text{ MHz}$ and $\Gamma_{Left} = 2\pi \times 2.0\text{ MHz}$ giving $F_{Right} = 416$ and $F_{Left} = 500$. During the assembly, we had to carefully align the cavity to match the condition $R = L$, which makes confocal resonators only marginally stable. Then, the science cavity support was aligned on top of it to ensure that the $\text{TEM}_{0,0}$ of each blue cavity is $500\text{ }\mu\text{m}$ away from the science cavity waist, see figure 2.8. The high-intensity beam is thus injected in a bow-tie mode and overlap with the cloud on its lower arm. Below this $500\text{ }\mu\text{m}$ separation, interferences in running-wave modes becomes too important and induce significant inhomogeneities.

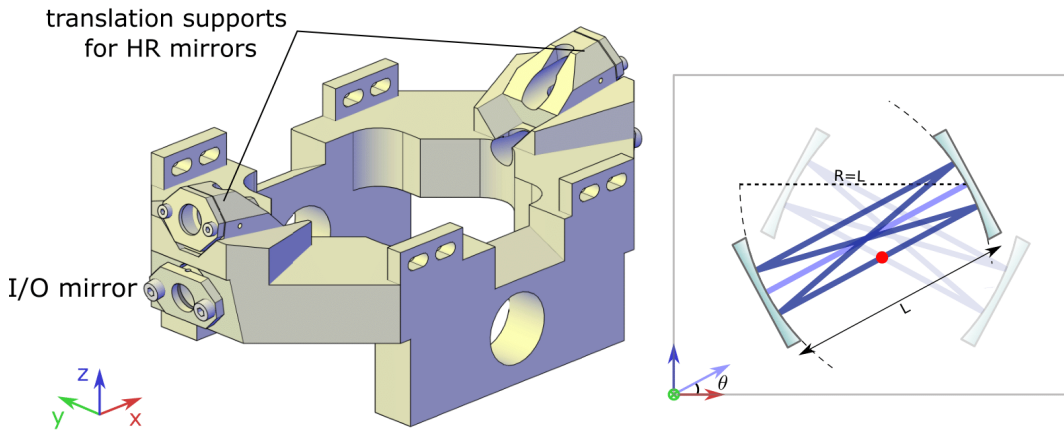


Figure 2.8: Blue cavities. The two blue cavities are perpendicular to the science cavity optical axis (y). Left- Blue cavities support, the two I/O mirrors can be translated to adjust the length of the resonators. Right- Sketch of the two resonators. A confocal cavity is characterized by a distance between mirrors equal to the radius of curvature, $R = L$. $\text{TEM}_{0,0}$ mode is represented in light blue while a bow-tie mode is drawn in deep blue and crosses the cloud, red dot.

The lengths of the cavities are stabilized like the science cavity, see 2.1.1 Cavity length locking. A ring piezo-actuator is placed behind the high reflectivity mirror of each cavity for the locking. The mirrors coatings are optimized at 474 nm and 480 nm only, so the $\text{TEM}_{0,0}$ mode is used to lock the cavity. The locking beam is separated from the high-intensity beam

by 500 MHz=FSR/2 for the cavity to be resonant for both beams when it is stabilized on the locking beam. By doing so, the locking light is not resonant with the addressed Rydberg state and it does not overlap with the cloud.

To align our power beam onto the cloud, the build-up beam is first injected in the TEM_{0,0}. It is easily identifiable because modes are separated by $\frac{c}{2R}$ and not $\frac{c}{4R}$. Then, the position of the high-power beam is adjusted by a mirror attached to a translation stage. The translation is not perpendicular to the optical axis of the cavity so the beam angle must be corrected to match the desired configuration. Therefore, we adjust the inclination to have the two outgoing beams separated by an angle of $\theta_1 = \frac{2l}{R}n$ and $\theta_2 = \frac{2l}{R}$ with respect to the input beam, where $l = 0.5$ mm is the displacement, $n = 1.52$ is the refractive index of BK7 at 475 nm giving a ratio of 3/2. This is what is expected for a perfectly aligned bow-tie mode. During this adjustment, we optimize the electromagnetically-induced transparency on the atoms-cavity spectrum.

Build-up factors

In theory, the running-wave mode of the power beam undergoes twice as much losses as the TEM_{0,0} mode. This is due to the fact that the light is reflected twice on the I/O mirror before ending its roundtrip. In reality, mirrors are always better in their center and it depends also on the quality of the length alignment to reach confocality. For the left resonator, the finesse in the bow-tie mode is estimated⁽¹²⁾ to be 40% of the TEM_{0,0} finesse. It is worse for the left cavity with only 26%. We attribute this difference to an imperfect adjustment of the length of the second resonator. The amplification of a cavity is defined as the ratio between the intensity inside the cavity and the input intensity: $A_{\text{build-up}} = I_{\text{cav}}/I_{\text{input}} = F_m/\pi$, with F_m the effective finesse. We observe an amplification of 45 (64 in theory) for the best cavity and 20 (41) for the second one with a waist of 200 μm . This value is estimated from the control Rabi frequency (measured on the EIT spectra). We have reduced the waist by a factor 3 and the build-up changed to 30 for the best cavity and 12 for the other one. Going further only makes this effect worse, so we are currently working with a waist of 60 μm ⁽¹³⁾. We measured the finesse in all those configurations and the drop remains unexplained. Here again, we suspect that this effect originates from a defect of the confocality. This could be explained by a distortion of the mode propagating through the resonator along with an enlargement of the waist.

⁽¹²⁾ Estimation from the linewidth of the mode.

⁽¹³⁾ We are here referring to the injected waist, we do not have access to the waist inside the resonator.

2.2 Laser bench

2.2.1 Lasers

The realization of lasers in the mid-1950s was a major technological progress for society and especially physics experiments. This is visible by the diversity of application and the variety of economic actors using this technology from medical areas to industry. This is also true for experimental science where lasers have allowed the development of spectroscopy [17], optics in the relativistic regime [18], trapping of atoms and nano-particles [19], etc. In our specific experiment at the crossing between ultracold atoms and quantum optics, lasers have to play several roles. The first one is to address rubidium transitions at the hyperfine level. This requires a monochromatic source with a narrow spectral linewidth so that we can manipulate a cloud of atoms: cooling, trapping... Laser light is also used to probe our system to study the coupling between our cavity and the atomic ensemble. From a technical point of view, we also need to stabilize the length of several resonators (science cavity, blue cavities...) and this is also done with lasers.

DL pro and TA pro

DL pro laser is an External Cavity Diode Laser (ECDL) built by Toptica. The system consists of a diode with an anti-reflective coating at one end, followed by a tunable grating optimized at a specific frequency. The other frequencies are then sent back to the diode. This back and forth travel between the diode and the grating filters the frequency and increases the output power. A DL pro produces about a few tens of milliwatts of a narrow width light with a tunable central wavelength that is perfectly adapted to our needs. Fast feedback can be sent to the current of the internal diode and slow feedback to piezoelectric actuators on the grating to stabilize the frequency. Our first DL pro is optimized at 780 nm with an output power of 41 mW and a beam waist of 0.5 mm. This laser is dedicated to repump atoms in the 3D MOT, in the 2D MOT and during atomic manipulation within the science cavity. It can address $|5S_{1/2}, F = 2\rangle \rightarrow |5P_{3/2}, F' = 1, 2\rangle$ transition depending on the context. The second one is used at 795 nm with 36 mW and it is used to address the D_1 line of rubidium 87 as a probe during experiments with Rydberg atoms (rubidium lines are shown in figure 2.9). The last DL pro is optimized at 780 nm with 60 mW, it is dedicated to degenerate Raman sideband cooling technique and its frequency is 10 GHz above the Repumper laser.

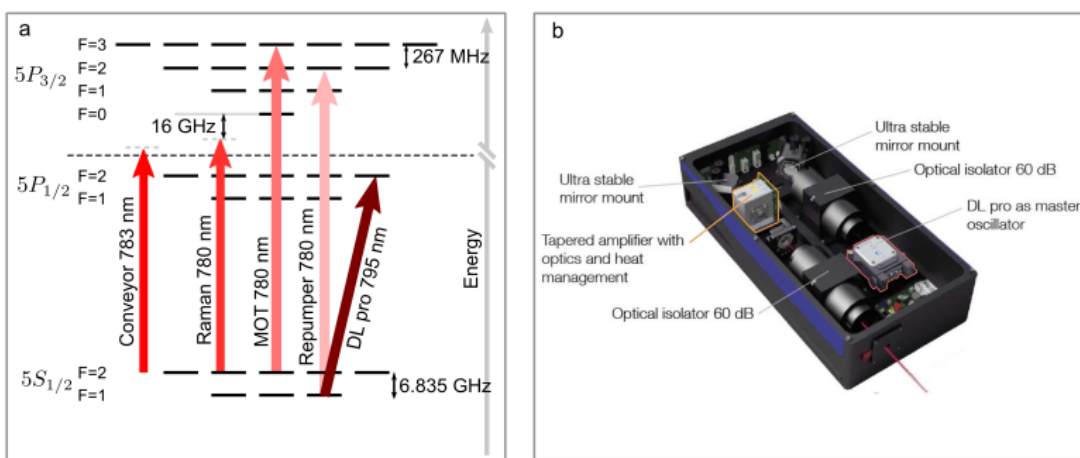


Figure 2.9: Rubidium Lines and TA pro . a- Rubidium D_1 ($5S_{1/2} \rightarrow 5P_{1/2}$) and D_2 ($5S_{1/2} \rightarrow 5P_{3/2}$) lines at the hyperfine level and lasers frequencies (in red). b- TA pro with the tapered amplifier and the DL pro (image from toptica.com).

As it can be seen the output power of a DL pro does not exceed 60 mW which is not enough for some trapping applications, for instance our 3DMOT alone requires about 200 mW⁽¹⁴⁾. To gain power we use a Tapered Amplifier laser system (TA pro), also marketed by Toptica, that produces about 1 W of laser light. The first one was optimized at 780 nm to be resonant with the D_2 line of rubidium 87, mostly applied on $|5S_{1/2}, F = 2\rangle \rightarrow |5P_{3/2}, F' = 3\rangle$. It is used in the 3D MOT and 2D MOT to trap and cool down atoms, for absorption imaging but also as a hyperfine pump for Raman degenerate sideband cooling. The laser building block is a DL pro employed as a master oscillator. It is followed by an optical isolator to prevent the intensity from returning back inside the laser diode. The light is then focused and led to a tapered amplifier where the geometry allows to both amplify and spatially filter the beams. The resulting output beam has a good quality factor⁽¹⁵⁾ with M^2 below 2. The output beam waist is 0.5 mm with an output power of 800 mW. Finally, a second optical isolator is put on the exit of the amplifier to further protect the optical system. We also have an older version of this laser, that is used to transport atoms from the 3D MOT to the optical cavity (the conveyor belt). The frequency of the laser is tuned at 783 nm with an output power of 1.1 W and a 500 μm waist.

Titanium-Sapphire Laser and External Cavity Doubler

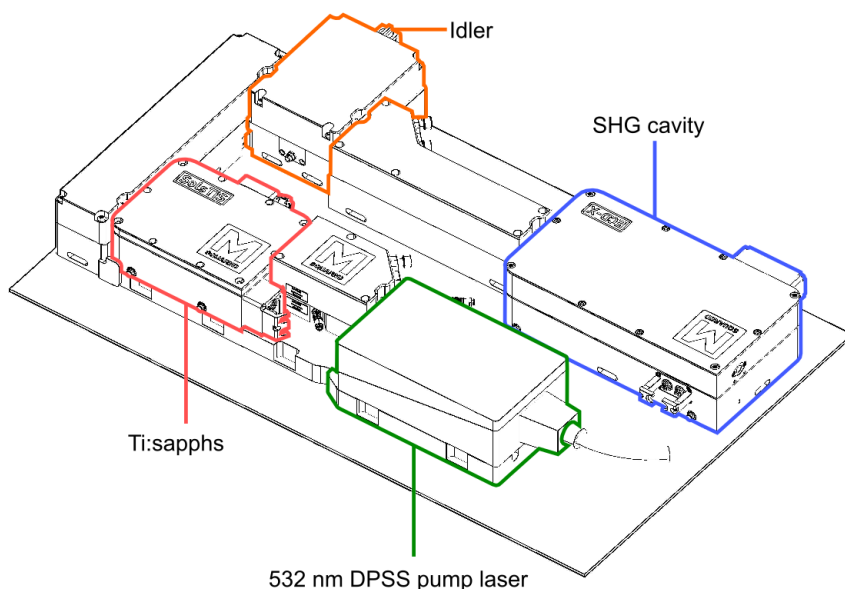


Figure 2.10: SOLSTIS laser. The titanium-Sapphire laser (in red) is pumped by a 532 nm laser diode (DPSS in green), itself pumped by a SPROUT laser at 1064 nm (18W). A small amount of the Ti:sapphres light is used as an Idler beam (orange) to lock the laser while most of the power goes to the SHG cavity (in blue) to produce up to 1W of blue. The gain profile of a TiSa crystal is very broad, so an etalon and filters are put inside the resonator to select a single mode of emission.

⁽¹⁴⁾ 10 mW in each arm with a splitter efficiency of 50% and double-pass acousto-optics modulator with 50% efficiency.

⁽¹⁵⁾ The parameter M^2 characterizes the deviation from a Gaussian beam, it is defined as $M^2 = \theta_{div} w_0 \pi / \lambda = \theta_{div} / \theta_{Gauss}$. θ_{div} is the output divergence angle and θ_{Gauss} the divergence angle for an ideal Gaussian beam of waist w_0 .

We also need a blue laser to address the Rydberg levels between 474 nm and 480 nm. One of the first constraint is to have a tunable laser on this frequency range. Furthermore, Rydberg states have a small overlap with the weakly excited states, so a high laser power is required to address them. Finally, the spectral width of the laser must be small enough not to broaden the targeted Rydberg state too much. The best option on the market to meet our expectation is to use a frequency doubling crystal in cavity fed by a Titanium-Sapphire laser. Our two SOLTIS lasers from Msquared focus on this demanding task and can deliver about 1 W between 460 nm and 490 nm. First, 18 W of 1064 nm is produced by a SPROUT pump and it is then frequency-doubled at 500 nm. This beam is sent to a standard Titanium-Sapphire laser (Msquared SolsTiS) with a tunable frequency from 680 nm to 1100 nm. The output beam is finally injected in a bow-tie cavity dedicated to Second Harmonic Generation and amplification (Msquared SolsTiS ECD). The non-linear crystal inside the cavity can be adjusted for mode-matching to cover the full range of frequencies from the TiSa. This laser can be stabilized by acting on two piezo actuators with two different ranges, one around ± 15 GHz for slow drifts and another one with ± 40 MHz for high frequency noise.

High Power 1064 nm fiber laser

The 1064 nm laser from Azur Light System (ALS) is a high-power laser with up to 10 W of output light. This laser is only used to trap atoms inside a crossed dipole trap. A seed laser is amplified by a high-power amplifier chain and goes to a fibered head. This makes the output beam quality factor very high, with $M^2 < 1.1$. We initially used this laser to lock the science cavity but we had numerous issues with it, such as mode jumps about 1 GHz, often multimode around the setpoint frequency...

2.2.2 Frequency locking chain

As discussed in the previous sections of this chapter, the experimental platform was designed to minimize inhomogeneous broadening of Rydberg states caused by stray electric fields or control fields inhomogeneities. To continue in this direction, it is therefore necessary to accurately control the spectral linewidth of our lasers. This involves our two TiSa, the TA pro at 780 nm and the DL pro at 795 nm with the aim to reach spectral linewidths below 10 kHz. The others lasers also need to be frequency stabilized. Indeed, our lasers are used to address the rubidium lines at a hyperfine level and for the length locking of our optical cavities. For instance, each of the three resonators inside the vacuum chamber is locked on a stable laser beam. This allows to compensate slow drifts and to adjust the cavity resonance to a specific rubidium transition. Seven of our lasers, out of eight in total, require frequency control.

Methods

Two techniques are used in our experiment, the first one is the Pound-Drever-Hall (PDH) method [20] that can be symmetrically implemented to lock a cavity on a laser and vice versa. The second method is a phase lock but it is only possible between two lasers. The idea, in both cases, is to have a signal to distinguish whether the system frequency is above or below a setpoint frequency. Then a PID controller⁽¹⁶⁾ (via piezo actuators, current, etc.) tends to minimize this error signal to reach the setpoint. Others method exists, for instance with saturated absorption on a vapor-cell [21], or with the Hansch-Couillaud method [22] but they are less stable than the PDH technique.

⁽¹⁶⁾The output signal is the sum of the proportional, integral and derivative terms of the error signal.

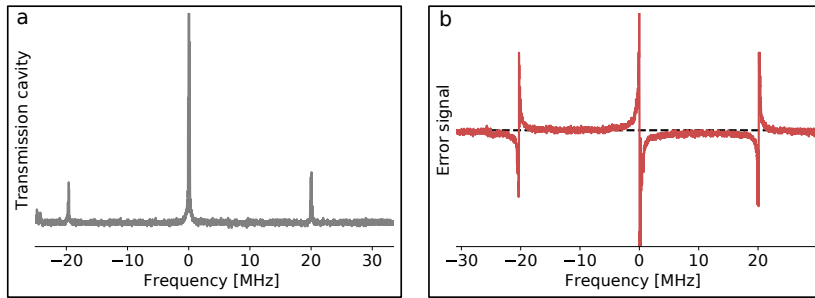


Figure 2.11: Pound-Drever-Hall. a- Laser intensity modulated at $\Omega=2\pi \times 20$ MHz by an EOM. b- Error signal of the Pound-Drever-Hall method. The zero is represented by the horizontal dashed line.

For the Pound-Drever-Hall (PDH) technique, the general idea is to look at the light reflection on a cavity. For a light beam crossing a cavity resonance, the phase of the field goes from $-\pi$ to $+\pi$. This is perfectly suited for a servo loop: one of the field quadrature is negative before a resonance and positive after. The aim of the method is to obtain a signal proportional to this quantity. The laser intensity is modulated at a frequency Ω by an electro-optic modulator (EOM) to produce two sidebands to the carrier. The resulting signal is then reflected on a cavity, it is acquired on a photodiode and demodulated at the frequency Ω . This signal is then given by:

$$S_{err} = S_0 \operatorname{Im}[R(\omega)R(\omega + \Omega)^* - R(\omega)^*R(\omega - \Omega)] \quad (2.12)$$

Where $R(\omega) = E_r/E_{input}$ is the cavity reflection at pulsation ω . Close to resonance and if the cavity linewidth is much more smaller than Ω , we have $R(\omega \pm \Omega) \approx -1$. This way, the measured signal is proportional to a quadrature of the carrier:

$$S_{err} \approx -2S_0 \operatorname{Im}(R(\omega)) \quad (2.13)$$

This defines the error signal of the PDH method, it is illustrated in the figure 2.11. The sign of the error signal is constant all along the range $]-\Omega, 0[$ and flips for $]0, \Omega[$ as shown in the figure. This gives a wide stability band for the PDH approach.

The phase-lock method is even simpler: two laser fields are mixed on a beam splitter and oscillations are recorded on a fast photodiode. This signal is demodulated at a given frequency f to obtain the error signal. The slave laser is then locked on the master laser with a frequency shift equal to $\pm f$. Even if this method is simple, it is less attractive than the PDH approach because it is hard and expensive to demodulate faster than 10 GHz and some of our lasers are separated by hundreds of terahertz.

Those two methods enslave one component to another but they do not provide any frequency reference. In our case, the absolute reference is given by an ultra-stable high-finesse cavity on which two lasers are locked. One of them is then used as a reference to stabilize a medium finesse cavity called transfer cavity. This cavity is in turn a reference for three lasers. A summary of the frequency stabilization of the lasers is shown in the figure 2.12.

Ultra-stable cavity and Transfer cavity

The absolute frequency reference of our experiment is an ultra-stable and high-finesse cavity made by Stable Laser System (SLS). The system is put under high-vacuum with a 10^{-8} mbar pressure to reduce thermal fluctuations of the optical index. The pressure inside the vacuum chamber is maintained by a ion pump (Agilent VacIon 2 L/s pump) with a flow of 2 L/s.

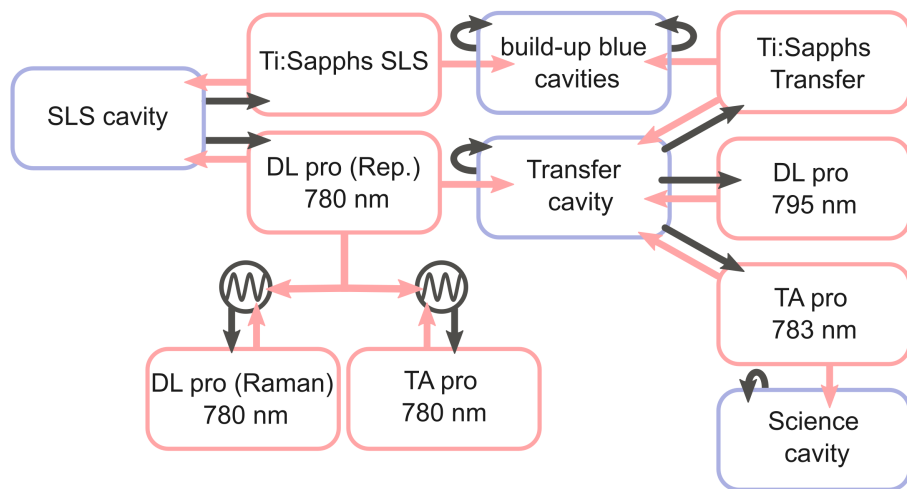


Figure 2.12: Locking chain. Cavities are circled in blue and lasers in red. Black arrows represent the electronic signal sent to stabilize a given component of the chain while red arrows symbolize the laser beam. Two lasers are phase locked on the TA pro 780 nm indicated by the black sinusoidal symbol.

Furthermore, this cavity is surrounded by an Ultra-Low Expansion glass (ULE) block and its temperature is stabilized at 28 °C where the expansion coefficient of ULE is minimal. We observed small drifts over months (< 1 MHz) that are easily compensated by looking at a saturated absorption spectrum on a rubidium cell. The distance between the two mirrors is $L = 10$ cm with a Finesse of ten thousands corresponding to a free spectral range of 1.5 GHz and a full width at half maximum of 150 kHz. The coating of the two mirrors were optimized for wavelengths at 780 and 980 nm so that our DL pro laser (Repumper) at 780 nm and one of the Ti:Sapphs are locked on that cavity. It was impossible to obtain a coating covering the whole set of laser frequencies while keeping the finesse of the resonator at this magnitude. For that reason, we have a second resonator: the transfer cavity with a medium finesse to lock three other lasers.

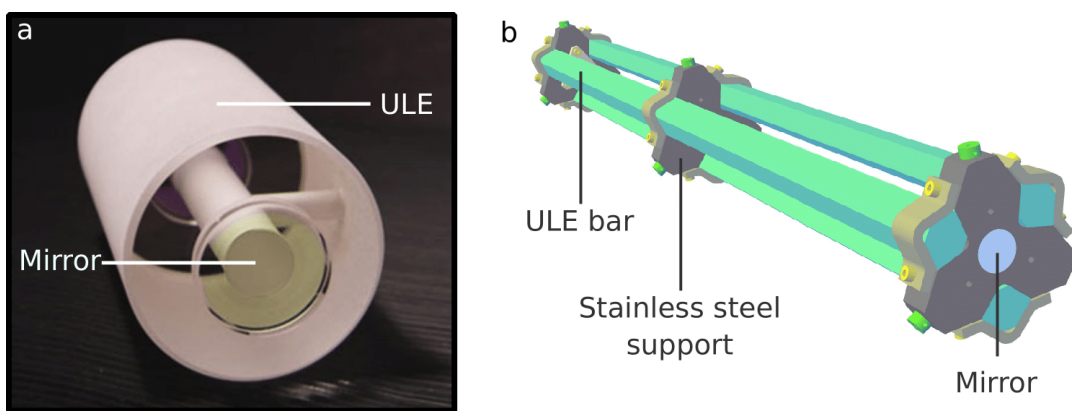


Figure 2.13: Stable Laser System cavity and transfer cavity. a- SLS cavity surrounded by a coat of ULE glass. The overall is put inside a vacuum chamber not visible in this image (image from stablelasers.com). b- The transfer cavity with three stainless supports each resting on two Viton cylinders for thermal and vibrational isolation. Three ULE bars maintain the whole system inside the vacuum chamber, mirror stand on each ends.

The transfer cavity is a homemade cavity stabilized by the DL pro (Repumper). The cavity

full width at half maximum is 100 kHz, close to the SLS cavity width. The free spectral range is much shorter with 200 MHz (instead of 1.5 GHz for the SLS cavity) to make the stabilization of others lasers easier. Thereby, the frequency of a laser can be adjusted over 200 MHz with a double-pass AOM to be resonant with the cavity. This constrains the length of the cavity to $L = 75$ cm. The resonator was designed to be stabilized by one laser and to lock three others lasers. It requires mirrors coating optimized at 960 nm, 780 nm, 795 nm and 1064 nm. This is of course only possible at the cost of a lower finesse (1800 at 795 nm). This cavity is also put under vacuum $P = 1.10^{-7}$ mbar for the same reason as the SLS cavity. Its pressure is also preserved by an ion pump (Agilent VacIon Plus 20 pumps) with a 20 L/s flow. Mirrors are sustained by three ULE glass bars hooked to the mirrors supports. Those supports are resting on Viton seals to further reduce mechanical vibrations (shown in figure 2.13). The DL pro at 795 nm, the 2nd Ti:Sapphs and the 783 nm laser are all locked on this cavity with the Pound-Drever-Hall technique. Each wavelength is separated by a grating after reflection on the cavity and it is acquired on a dedicated photodiode for locking.

The beatnote noise⁽¹⁷⁾ of our two Ti:sapphs lasers locked with the PDH method is estimated to 3 kHz. We further estimated the noise of one of the infrared probe, the DL pro 795 nm. In that case, the half width at $e^{-1/2}$ is 2.5 kHz. This estimation is obtained by comparing the amplitude of the error signal with the rms noise of the signal during the lock.

⁽¹⁷⁾Half width at half maximum, acquisition duration of 15 ns.

2.3 Control setup

This kind of experiment lies between cold atoms physics and quantum optics experiments. Therefore, there is an important difference in time scale between our needs for the atomic preparation and the optical part. For atomic manipulation, we need control from the microsecond to few seconds while the duration of our light pulses or the lifetime of our polaritons is about 100 ns. This particularity of our experiment has several consequences on the control and acquisition for both hardware and software means.

2.3.1 Hardware

The run of a single experimental cycle takes about 100 ms, from the 2D MOT loading to a measurement with the science cavity. In this short period of time, we must be able to switch off and on beams, swipe frequencies and acquire data. This whole process is managed by a PXI controller from National Instrument with several specialized electronic cards.

First of all, we need RF generators to drive AOMs (Acousto-Optic Modulator) in order to adjust the frequency of our beams. RF frequencies up to 300 MHz are generated by DDS (Direct Digital Synthesizer). Those RF generators are controlled by a FPGA (Field Programmable Gate Array) with the aim of modifying or sweeping the frequency, amplitude and phase of the signal during an experimental cycle. We also have home-made generators built from Arduino boards where the same parameters can be adjusted but fixed for a given cycle. For gigahertz waves, we make use of commercial USB generators built by Winfreaktech. Each DDS and Arduino channel can be switched off/on by an external TTL and the amplitude can be adjusted by an external analog signal. This is for instance useful when we want to lock the intensity of a laser beam.

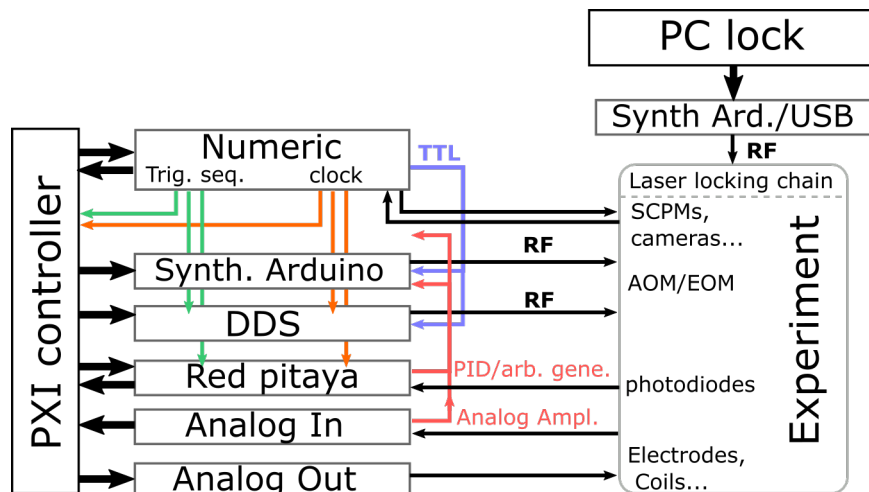


Figure 2.14: Control of the experiment. The PXI system sends instructions to the different cards. The instruments are synchronized by a trigger signal generated by the numeric card. DDS and Arduino channels produce RF signals for AOM and EOM on the experiment to adjust the frequency of our lasers beams or to simply switch light on/off. Digital channels can be used as TTL for RF channels, for our cameras... Some of those channels are configured to acquire data from SPCM, either time stamps or with adjustable time bins. Output Analog cards are devoted to the analog control of our RF signals, the voltage of our 8 electrodes, etc. Input Analog cards records photodiodes signals from 100 kHz to 250 MHz. Red Pitaya are programmed as a PID to lock the intensity of a laser beam during the sequence or can be used as an arbitrary function generator. A second controller is dedicated to the laser locking chain to adjust the frequency of each laser by driving AOM and EOM through Arduino and USB synthesizers.

Our digital cards generate TTL signals and are used to acquire data with SPCMs (Single Photon Counting Modules). Two modes are possible, either with digital input channel where we record time stamps with a resolution of 10 ns or digital analog input channel with an adjustable time bins adapted to a high photon rate. The standard signal acquisitions is carried out by analog cards in input mode with sampling rate up to 250 MHz for our two fast cards and at 100 kHz with slow cards. We also have analog cards in output mode for analog control of RF generators, electrodes driving...

Finally, we have Red Pitaya boards with an integrated FPGA for arbitrary function generation. For instance, it is used to shape short Gaussian pulse (50 ns intensity rms⁽¹⁸⁾). They are programmed to work as an analog control and/or as a servo loop with the ability to adjust or sweep the setpoint during a cycle at a 125 MHz rate.

The synchronization between instruments is ensured by a reference clock at 25 MHz and a sequence TTL defines the beginning of the sequence for the whole system.

2.3.2 Software

The software control is done by a home-made LabView program (VITO) on our PIX system. The user interface is separated in four main panels:

- **Select Channels:** The first interface is where the user picks channels to control from the list of instruments discussed in the previous subsection. Only those instruments will participate to the sequence.
- **Config Sequence:** This one is dedicated to the global structure of the sequence. This is where we define the steps with adjustable durations. Each step is executed one after the other and it is possible to make loops. This succession of steps defines what is called the experimental cycle. In this window, one can also define variables that are used to scan parameters between experimental cycles.
- **Config Channels:** The third panel is where the user programs each channel. For instance, a DDS channel can be configured for each step and it is also possible to define substeps. One can also use previously defined variables to scan a parameter between experimental cycles.
- **Run Sequence :** In the last interface, the user defines the number of cycles and starts sequences. This panel can display the data and handles its storage. The complete sequence can be saved in a SQL database and already saved sequences can be loaded. Data are stored in a TDMS files while the associated sequence is automatically uploaded to the database. They both share a unique ID key to ensure unambiguous identification.

An example is shown in figure 2.15 and figure 2.16, where two of the four panels are visible. We have a second software programmed in Python (RubImaPy) for imaging application. This program collects images from our cameras and is thus used in parallel of the VITO program.

⁽¹⁸⁾Half width at $e^{-1/2}$ of the intensity.

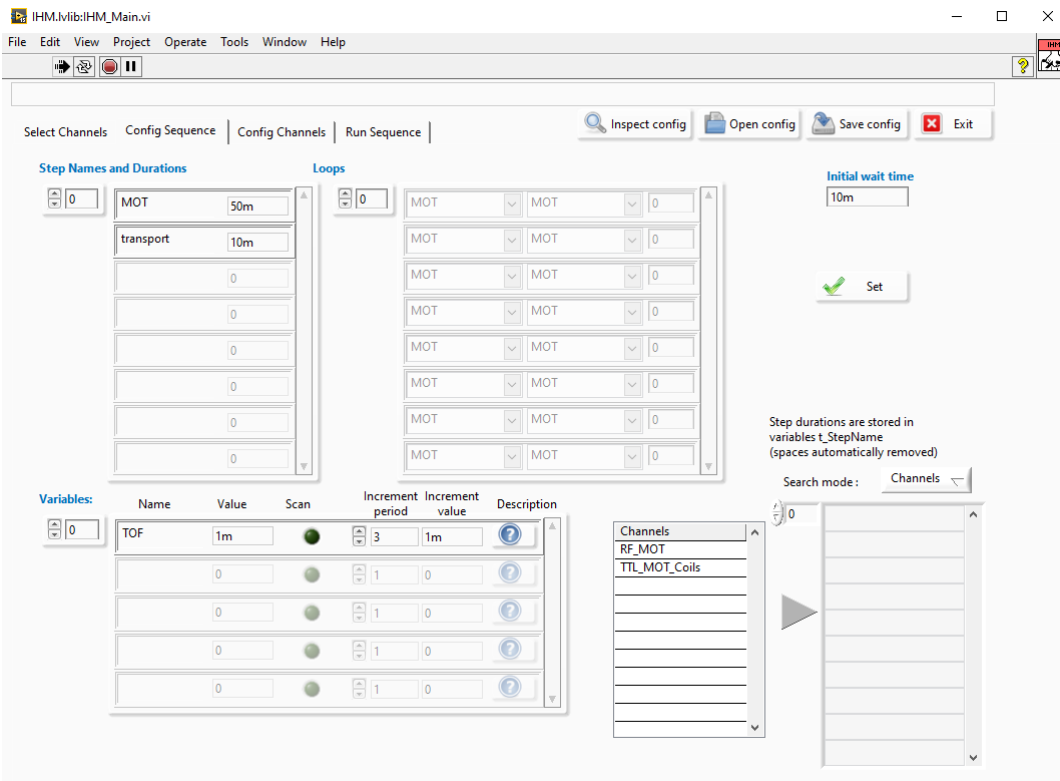


Figure 2.15: Vito, Config Sequence.

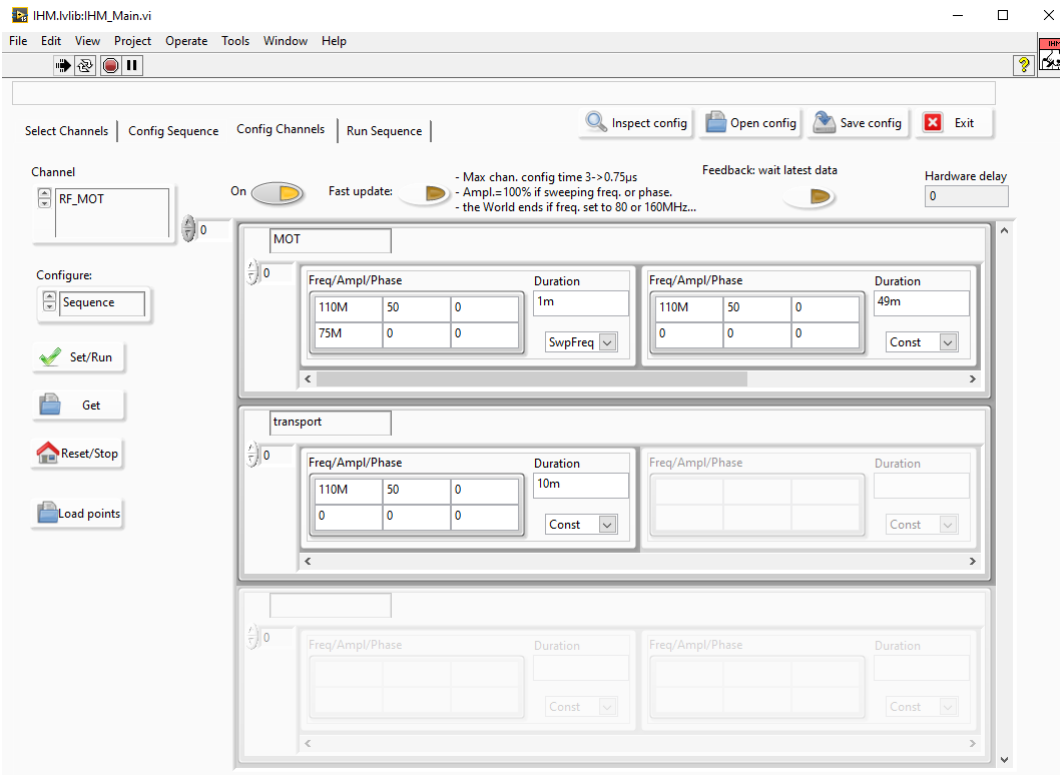


Figure 2.16: Vito, Config Channels.

Chapter 3

Preparation of an atomic ensemble inside the science cavity

Contents

3.1	Magneto-optical traps	39
3.1.1	Atomic beam: 2D MOT	40
3.1.2	3D Magneto-optical trap	41
Absorption imaging	42	
Compression and optical molasses	43	
Magnetic field compensation	44	
3.2	Optical dipole traps	46
3.2.1	Conveyor belt	47
Transport	48	
Longitudinal trapping frequencies	49	
3.2.2	Crossed-dipole trap	49
3.3	Degenerate Raman sideband cooling	51
3D optical lattice	51	
Raman transitions	52	
Experimental result	53	

This chapter now focuses on the preparation of a small cold and dense atomic cloud in our science cavity. The size of the atomic ensemble is adjusted to fit inside a unique Rydberg blockade volume, in a regime where the number of excitations through the resonator is limited to one [23, 24]. The size of the blockade sphere depends on several parameters but the order of magnitude is $R \simeq 16 \mu\text{m}$ for the 100S Rydberg state ⁽¹⁾. Once the size is fixed, the atomic density directly sets the coupling between the cavity and the atomic sample. We are thus free to explore the system's response in several coupling regimes with density values up to $5 \times 10^{11} \text{ cm}^{-3}$. The last parameter of interest is the temperature of the cloud that we managed to decrease to $2 \mu\text{K}$. At this temperature, the Doppler contribution and the inhomogeneous lightshift of the trap are small enough to not broaden too much the Rydberg linewidth.

Initially, the hot rubidium vapor is not located in the main chamber to keep the pressure as

⁽¹⁾ $C_6 = 56 \text{ THz}/\mu\text{m}^6$ for a linewidth of $\gamma = 3 \text{ MHz}$, $R = (C_6/\gamma)^{1/6}$.

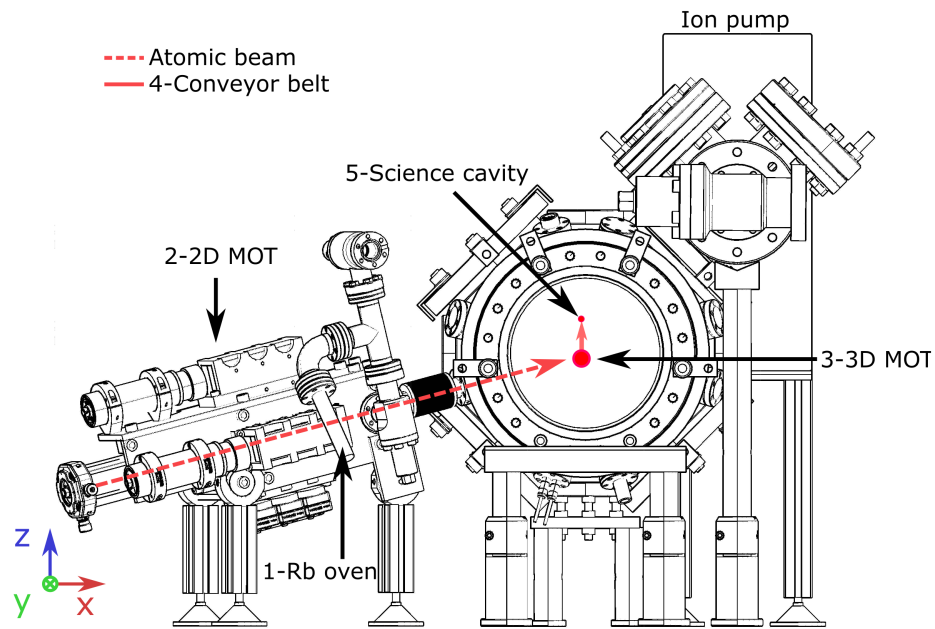


Figure 3.1: Vacuum chamber. 1- A solid sample of rubidium is heated at 37 °C in the oven. 2- Atoms are trapped and cooled down in two directions and pushed along the third one in the 2D MOT cell. 3-3D MOT is loaded by the atomic beam in the main vacuum chamber. 4-Cold atoms are transported over 33 mm in a conveyor belt. 5- Optical cavity, the cloud is cooled down using degenerate Raman sideband cooling and loaded in a crossed dipole trap.

low as possible in there. Several steps are necessary to cool, transport and trap atoms inside the science cavity as it is depicted in figure 3.1. First of all, a solid rubidium sample is heated at 37 °C in the oven. The produced gas spreads to the 2D MOT chamber where it is trapped and cooled down along the transversal axes by retro-reflected beams. A third beam is sent along the longitudinal direction to push atoms: they leave the 2D MOT (Magneto-Optical Trap) through a differential pumping tube and enter the main vacuum chamber. The atomic beam generated by the 2D MOT is again trapped and cooled down in a three-dimensional magneto-optical trap (3D MOT) inside the main chamber. The first section of this chapter is devoted to this part of the atomic manipulation, with a review on magneto-optical traps for rubidium 87 and a presentation of the parameters of our setup. Once atoms are trapped in the 3D MOT, the cloud is loaded into a 1D standing wave optical trap and it is transported 33 mm upwards at the level of the science cavity. This separation between the MOT and the cavity increases the duty cycle of our experiments as it is thus possible to keep atoms in the MOT while doing acquisitions with our science cavity. Finally, the cloud inside the cavity is cooled down by means of a degenerate Raman sideband cooling technique and loaded in a small crossed dipole trap. As mentioned in the beginning, this Raman cooling step reduces the inhomogeneous broadening of the Rydberg linewidth and increases the coherence time of a collective excitation in the gas. In addition, the lifetime inside the dipole trap is about few seconds and the trap induced light shift is low enough to probe several times the same cloud directly in the trap without reloading from the 3D MOT. The second section is dedicated to optical dipole traps, especially atomic transport to the science cavity and the small crossed dipole trap. In the last part of this chapter I discuss the degenerate Raman sideband cooling protocol used to reach temperature values on the order of 1 μK at the science cavity level.

3.1 Magneto-optical traps

This standard technique in ultra-cold experiments was used for the first time in the experiment conducted by the group of Pritchard [25] and allows to cool and trap atoms with light. In a magneto-optical trap (MOT), counter-propagating beams produce a frictional force on the atoms induced by the combination of the Doppler effect and radiation pressure. For an atom moving towards one of the beams with a velocity v , the Doppler shift reduces the detuning between the atomic transition and the frequency of this beam proportionally to the velocity. The detuning is on the contrary increased for the second beam propagating in the opposite direction. On average, the atom absorbs more photons from the first beam leading to a decrease of the velocity. In this one dimensional case, the force can be written as :

$$F_c(v) = -\alpha v \text{ where } \alpha = -\hbar k^2 s_0 \frac{2\Gamma\delta}{\Gamma^2/4 + \delta^2} \quad (3.1)$$

where \hbar is the reduced Planck constant, Γ the transition linewidth, c the speed of light, I the light intensity, k the wavenumber and $\delta = \omega_L - \omega_a$ the frequency detuning of the laser (ω_L) with respect to the transition (ω_a) which has to be negative to ensure that $\alpha > 0$. And we have introduced the saturation parameter s_0 :

$$s_0 = \frac{I/I_s}{1 + 4\delta^2/\Gamma^2} \text{ with } I_s = \frac{\hbar\omega_a^3\Gamma}{12\pi c^2} \quad (3.2)$$

This expression of the light force remains valid as long as $s_0 \ll 1$ meaning that the transition line is not saturated by light. In this low saturation limit, the maximum of α is reached at $\delta = -\Gamma/2$.

In addition to this frictional force, a harmonic trap is obtained by adding a magnetic field gradient of slope b to take advantage of the Zeeman effect in the light absorption process. As the Zeeman shift is linear with the magnetic moment μ , one can choose the polarization of counter-propagating beams to be opposite in an absolute referential to address $\sigma+$ and $\sigma-$ transitions. For atoms in the zero magnetic field region, the two beams induce an equal and opposite pressure leading to a zero mean force. When atoms are out of this region, the magnetic field gradient breaks this force balance. The detuning is reduced for one of the beams and increased for the other one due to the circular polarization. By adjusting the gradient direction with respect to the choice of polarization between the two beams, the light kicks atoms back to the zero field region. Therefore, this mechanism leads to a harmonic trapping force. In this one dimensional case and in the low saturation limit, this force is given by:

$$F_t(x) = -Kx, \text{ with } K = -k\mu b s_0 \frac{2\Gamma\delta}{\Gamma^2/4 + \delta^2} \quad (3.3)$$

It is assumed here that the cloud width is much smaller than that of the beam, $I(r) \approx I_0$.

We work with rubidium 87, a widely used atom in ultracold atoms experiments because of its well-known atomic structure and the technology maturity of laser diodes to address those atomic resonances. ^{87}Rb fundamental fine doublet is made of the line $5S_{1/2} \rightarrow 5P_{1/2}$ at 795 nm and $5S_{1/2} \rightarrow 5P_{3/2}$ at 780 nm that are called \mathbf{D}_1 and \mathbf{D}_2 respectively and the population decay rates of this doublet is $\Gamma_1 = 2\pi \times 5.75 \text{ MHz}$ and $\Gamma_2 = 2\pi \times 6.07 \text{ MHz}$. More details about this atom can be found in the detailed article of Daniel Adam Steck [26]. In the context of a magneto-optical trap, the D_2 line is preferred due to the existence of a cycling transition $|F=2, m_F=\pm 2\rangle \rightarrow |F'=3, m_{F'}=\pm 3\rangle$ with the strongest dipole matrix element. Atoms fallen in $5S_{1/2} F=1$ are repumped by a dedicated beam to $5P_{3/2} F'=2$ state, visible in figure 3.2. The temperature in the Magneto-optical trap is limited by light diffusion such that at the optimum $\delta = -\Gamma/2$, the Doppler temperature for ^{87}Rb is $T = \hbar\Gamma/(2k_B) = 146 \mu\text{K}$,

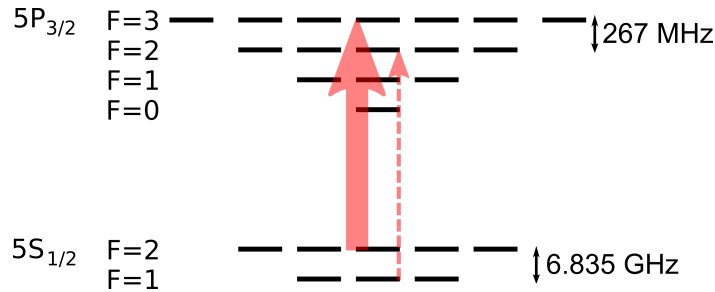


Figure 3.2: MOT beams for the D_2 line of rubidium 87. The rubidium 87 D_2 line is used for the magneto-optical trap. In dashed line the repumper beam and in solid line the trapping and cooling beam.

where k_B is the Boltzmann constant. One can switch off the magnetic field to get past this limit by taking advantage of the temperature scaling law in an optical molasses as we will see for the 3D MOT [27].

3.1.1 Atomic beam: 2D MOT

Our 2D MOT is a compact Low-Velocity Intense Source of atoms (LVIS) for ultracold experiments [28]. The system can be decomposed in two parts.

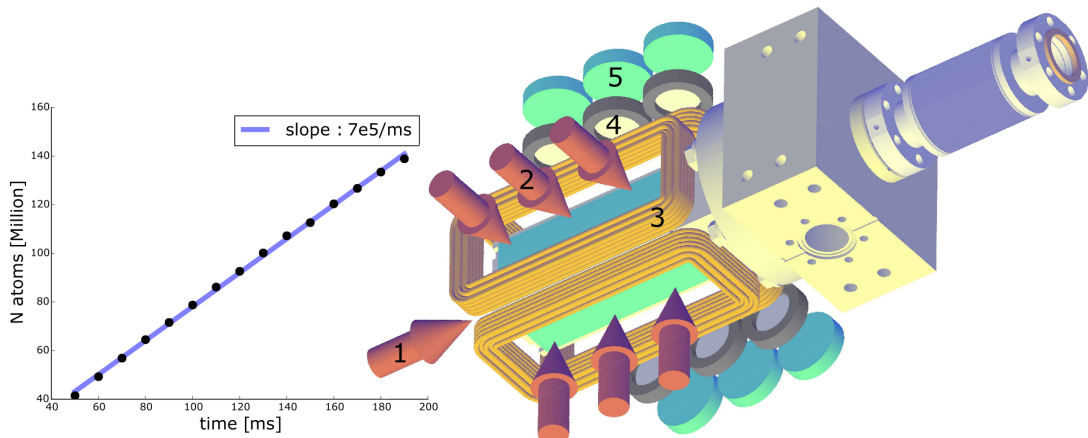


Figure 3.3: 2D MOT drawing and 3D MOT loading rate. Left- Loading rate of the 3D MOT by the atomic beam in the linear regime. Right- Simplified drawing of the 2D MOT. 1- pusher laser, 2- transverse cooling beams, 3 - anti-Helmholtz coils, 4- Quarter-Wave Plates, 5- mirrors.

The first one is a standard two-dimensions magneto-optical trap for rubidium 87 and ensures trapping and cooling in the transverse plane of the setup. The repumper applied on $5^2S_{1/2}, F = 1 \rightarrow 5^2P_{1/2}, F' = 2$ is generated by an external cavity laser diode (ECDL, Toptica DL Pro) and the MOT beam is provided by a taper-amplified ECDL (Toptica TA Pro), see Chapter 2 for more information about our lasers. This DL pro is locked on our ultra-stable cavity and it is used as a reference for the TA pro (phase lock 6.8 GHz below). Both the power of the MOT beam and its frequency can be adjusted by a double-pass Acousto-Optic Modulator (AOM) with a frequency shift between 150 and 250 MHz. The intensity of the repumper beams is also controlled by a single-pass AOM. Repumper (total output of 400 μ W) and MOT (50 mW) beams are combined and sent through two fibers to the two transversal axes of the 2D MOT system. In each of those two axes the output light is splitted in three parts by unpolarized beam splitters to enlarge the trapping area ($\simeq 13$ mm waist) all along

the vacuum cell where rubidium vapor is located. This light is then retro-reflected and its polarization is controlled by quarter wave-plates. A simplified drawing of the 2D MOT is shown in figure 3.3. Finally, two pairs of coils in anti-Helmholtz configuration generate a magnetic field gradient of 8.3 G cm^{-1} with a current of 2.5 A .

The glass cell itself was made of BK7 antireflection-coated windows and glued on a titanium frame (same expansion coefficient. It is connected to the rubidium oven where the solid sample is heated at 37°C to produce a hot vapor. Finally, the pressure inside the 2D MOT is around 10^{-7} mbar and is maintained by the differential pressure existing within the main chamber.

Along the third axis, a beam is collimated and crosses the glass cell to arrive at the level of a mirror with a $1 \mu\text{m}$ -diameter hole in its center. This resonant light exerts radiation pressure on the atoms by momentum transfer. In a retro-reflected configuration, atoms are equally kicked in the two opposite directions resulting in a zero mean force. Here, the part of the beam going through the hole breaks this balance and induces a force accelerating the atoms:

$$F_p = \frac{\Gamma}{2} \hbar k \frac{s_0}{1 + s_0} \text{ at } \delta = -3\Gamma \quad (3.4)$$

This acceleration is maintained by the repumper beams and stops as soon as atoms leave the 2D MOT, with a velocity of 6 m s^{-1} . The atomic source is connected to the chamber by a flexible port aligner and rests on adjustable feet to align the atomic jet with respect to the main chamber. The power and detuning of repumper and MOT beams were optimized via the loading rate of the 3D magneto-optical trap inside the main chamber, $\approx 7.10^8 \text{ s}^{-1}$ (see left panel in figure 3.3).

3.1.2 3D Magneto-optical trap

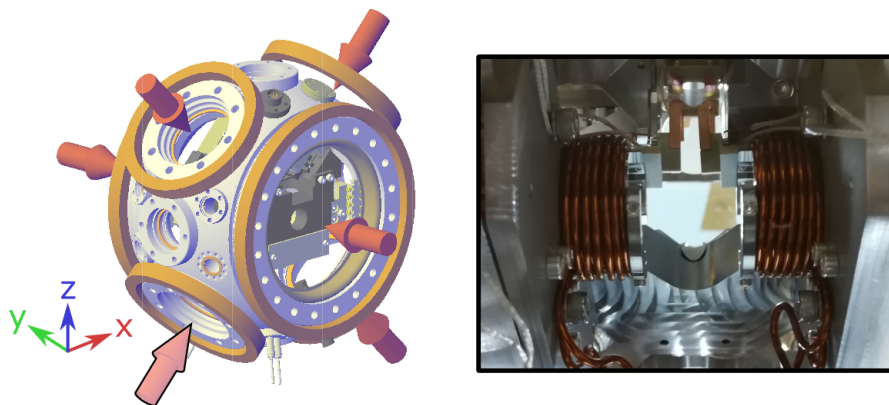


Figure 3.4: Magneto-optical trap setup. Left- Vacuum chamber with the six MOT beams, red arrow, and the six compensation coils in orange. Right- MOT coils inside the vacuum chamber, image taken from the arrow circled in black on the left drawing.

The first trap in the main vacuum chamber is a three-dimensional magneto-optical trap. Its role is to act as a reservoir of cold atoms to rapidly reload atoms inside the science cavity. The MOT and repumper beams come from the same lasers as those of the 2DMOT. The frequency and the power of the MOT beams are adjusted by a double-pass AOM while the repumper is only controlled in intensity by a single-pass AOM. Repumper and MOT beams are combined by a Schäfter-Kirchhoff variable fibered splitter (2 inputs-6 outputs). Each output beam contains approximately 12 mW of TA pro and $200 \mu\text{W}$ of repumper and has a 7.5 mm radius after collimation. The beams are distributed along three orthogonal axes.

This splitter has two photo-diodes for each input beam, that are used to lock the intensity with a PID loop feeding back the associated AOM. The magnetic field gradient is generated by a pair of coils placed inside the vacuum chamber to reduce the value of the current and thus avoid water/air cooling. Those two coils are in anti-Helmholtz configuration, each made of 12 turns of copper wire and powered via a feedthrough by a DC Power supply from Delta Elektronika (SM 15-100) with a homemade analog electronic circuit for current control. The ground of this supply is isolated from others electrical devices by an opto-isolator to protect them from voltage or current spikes. The typical current sent through the MOT coils during a sequence is around 7 A resulting in a magnetic gradient of 8 G cm^{-1} with a $25 \mu\text{s}$ switch time. The magnetic field zero is obtained by three pairs of coils in Helmholtz configuration, placed outside the chamber. The method used to properly compensate external magnetic field is detailed in a following sub-section. MOT beams, MOT coils and compensations coils are all shown in figure 3.4.

Absorption imaging

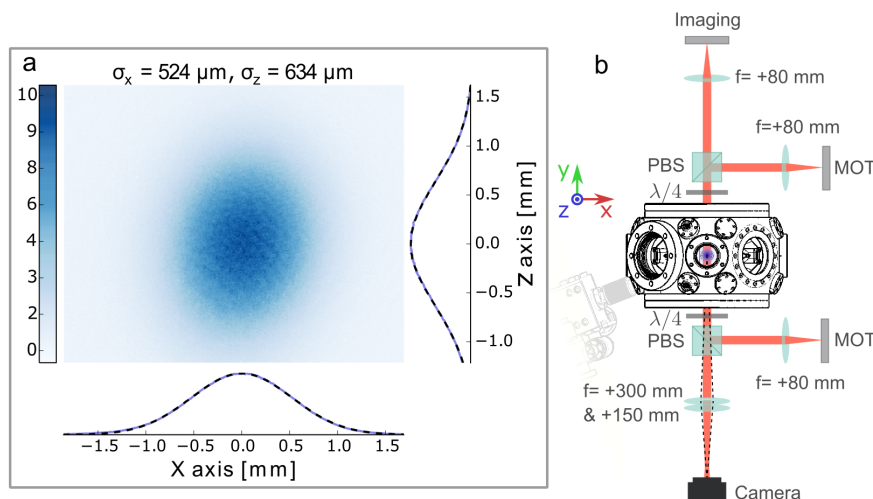


Figure 3.5: Absorption imaging. Left- Absorption imaging after a 10 ms time of flight. The color bar represents the integrated atomic density in μm^2 . The standard deviation σ_x is obtained by a gaussian fit of the integrated image along the z axis and vice versa for σ_z . Right- Imaging setup: PBS for Polarized beam splitter and $\lambda/4$ for quarter-wave plate. Imaging light is combined to the MOT beam with a PBS. Then it crosses the cloud and is acquired on the Point Grey camera.

A Point Grey camera (CM3-U3-13Y3) is aligned with one of the 3D MOT beams to access some parameters of the cloud by the standard absorption technique [29]. Resonant light is combined to the horizontal arm of our MOT with a polarized beam splitter. Part of the light is thus absorbed by the atomic sample which locally reduces its intensity. On the other side of the chamber, light is then collected by two thin lenses in contact and measured by the camera (1/2 magnification). This contact configuration is preferred to reduce optical aberrations in the imaging. Finally, this image is compared to a reference image without any atom taken 100 ms later. The ratio pixel by pixel between those two images gives access to the optical depth (OD) of the cloud:

$$\frac{I(x, y)}{I_0(x, y)} = e^{-OD}, \text{ with } OD = -\sigma_0 \int_l dz n(x, y, z) \quad (3.5)$$

where n is the atomic density, $\sigma_0 = 2.907 \cdot 10^{-9} \text{ cm}^2$ is the resonant cross section. As it can be seen in figure 3.5, it is possible to infer the total number of atoms, the integrated density $n(x, y)$ and the transverse Gaussian size of the cloud.

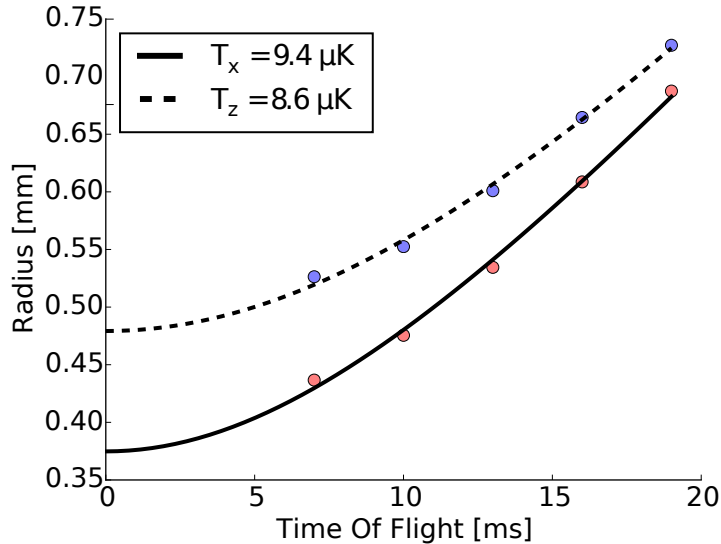


Figure 3.6: Temperature measurement. Estimation of the temperature along the two axes perpendicular to the imaging beam. The fitting function is defined by eq 3.6 and only depends on two parameters: the temperature and the initial size of the atomic cloud. This measurement was done after optimization of the compression and molasses steps with a fine magnetic field compensation, see following subsections.

Moreover, the temperature of the cloud is estimated by a time of flight technique: the size of the cloud is measured for different delays between the end of the MOT step and the imaging step. The expansion of the cloud is then given by:

$$\sigma_{rms}(t) = \sqrt{\frac{k_B T}{m} t^2 + \sigma_{rms}(0)^2} \quad (3.6)$$

where k_B is the Boltzmann constant, $m = 1.44 \cdot 10^{-25} \text{ kg}$ is the atomic mass of rubidium 87 and σ_{rms} is the root mean square of the atomic density distribution. This method is illustrated in figure 3.6.

Compression and optical molasses

In order to transport as many atoms as possible to the cavity, the MOT undergoes a compression phase followed by a molasses step to get past the Doppler temperature. The loading of the 3D MOT by the 2D MOT is done in 50 ms. The MOT beams are 3Γ red-detuned from $5S_{1/2}, F = 2 \rightarrow 5P_{3/2}, F' = 3$ line while 2D MOT beams are 10 MHz red-detuned to reduce heating. The repumper intensity is kept above saturation at 6 mW cm^{-2} and 2 mW cm^{-2} respectively for the 2D MOT and main MOT, but the cloud is essentially insensitive to that parameter. During this loading, the magnetic field gradient is 8 G cm^{-1} for the 2D MOT and 20 G cm^{-1} for the 3D MOT. The second step is the compression: during one millisecond, the magnetic field gradient is swept from 8 to 21 G cm^{-1} in order to increase the atomic density in the trap while others parameters are kept constant. In the last step, the magnetic field is adiabatically switched off in two milliseconds to produce a molasses to get past the Doppler limit ($T=146 \mu\text{K}$). As explained in the article of Dalibard [30], the reachable temperature

in the molasses scales as $T \propto I/\Delta$ where I is the intensity of the MOT beam and Δ is the detuning. In the first millisecond, the frequency of the MOT beam is swept from -3Γ to -23Γ (red-detuned). Its intensity is linearly decreased by a factor 30 during two milliseconds and at the same time, the repumper intensity is also decreased close to zero. After this sequence, the cloud temperature is $9\ \mu\text{K}$, the number of atoms is $N \simeq 30.10^6$ with a RMS width⁽²⁾ of 0.5 mm. A table summarizes the range of several parameters of our magneto optical trap.

Number of atoms	30.10^6
RMS width	0.5 mm
Density	$10^{10}\ \text{cm}^{-3}$
Temperature with molasses	$9\ \mu\text{K}$
Magnetic field gradient	$20\text{-}40\ \text{G cm}^{-1}$
MOT beam detuning	$3\Gamma\text{-}12\Gamma$
MOT beam intensity	$17\ \text{mW cm}^{-2}$

Table 3.1: Summery of the MOT parameters after 50 ms of loading.

Magnetic field compensation

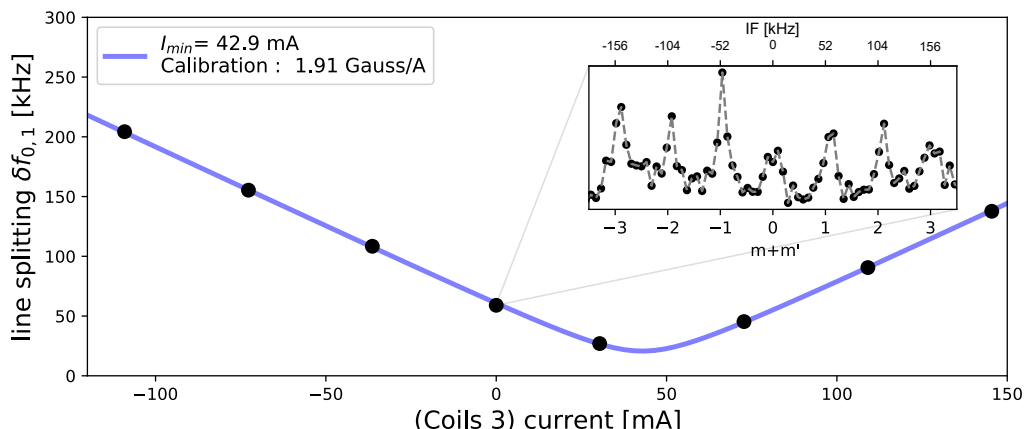


Figure 3.7: Magnetic field compensation. Radio-frequency measurement of the Hyperfine splitting. Main plot- Splitting frequency of $5^2\text{S}_{1/2}$ hyperfine levels $\delta f_{0,1}$ while varying the current of one of the compensation coils (data in black, fit in blue). The fitting function is $f(I) = \mu_B g / \hbar \sqrt{p_{cali}^2 (I - I_{min})^2 + B_{off}^2}$, with three free parameters : p_{cali} , I_{min} and B_{off} . Top right corner - Initial splitting between the seven hyperfine lines as expected from eq 3.7.

One important step to optimize the MOT is to cancel residual magnetic fields at the cloud center. Any offset in the magnetic field will move the center of the magnetic trap and thus induce a heating of the cloud. Three pairs of coils in Helmholtz configuration were attached around the viewports of the chamber, the two DN 160 and the four DN 60 in diagonal (figure 3.4) to produce a constant compensation field in the three dimensions. Each pair is driven by a High Finesse bipolar current power supply controlled by an analog voltage ($1\text{A} \leftrightarrow 5.5\text{V}$). In order to obtain the value of the magnetic field at the cloud position, we looked at the Zeeman splitting of the transitions between $5\text{S}_{1/2}$ hyperfine sub-levels ($6.834\ 683\ \text{GHz}$, $F = 1 \rightarrow F = 2$). The Zeeman splitting between states $|L = 0, F = 1, m\rangle$

⁽²⁾Standard deviation of the density distribution, here a Gaussian.

and $|L = 0, F = 2, m'\rangle$ is given by:

$$\delta f_{m,m'} = f_{m'} - f_m = \frac{\mu_B}{\hbar} g(m' + m) |\mathbf{B}| = \delta f_{0,1}(m + m') \quad (3.7)$$

where $|\mathbf{B}|$ is the norm of the magnetic field, μ_B is the Bohr magneton, \hbar is the reduced Planck constant and g is the Landé factor⁽³⁾ of the hyperfine state $5S_{1/2}$, $F = 2$ in Eq. 3.7.

The sequence starts by a simple MOT loading by the 2D MOT in 50 ms. Then, the magnetic field gradient and all beams are switched off except for the repumper to bring the cloud in $5S_{1/2}$, $F = 2$ state ($\sim 100 \mu\text{s}$). Next, the repumper is switched off while the microwave field is emitted from an antenna close to the vacuum chamber during ~ 1 ms. The 6.834 GHz microwave signal is generated by a Windfreaktech Synth HD, mixed with an intermediate frequency signal (IF range 1 kHz \sim 100 MHz) to adjust the frequency. The overall signal is amplified (KUHNE electronic RF power amplifier⁽⁴⁾, gain: + 40 dBm) before emission. Provided that the microwave signal is at resonance with one hyperfine transition, a part of the cloud is pumped in $F = 1$. A resonant beam removes atoms in $F = 2$ and then atoms in $F = 1$ are repumped in $F = 2$. Then, the number of atoms is measured in $F = 2$ by imaging. We obtain the hyperfine spectrum of the $5S_{1/2}$ state by repeating this procedure for several values of the microwave frequency, see top right corner plot in figure 3.7. This measurement is done for different current values for each pair of compensation coils to extract the optimal value of the current in the three directions. An example is shown in figure 3.7, for one pair of coils. Once the optimization is done, the full width at half maximum of the transition is ~ 50 kHz and the frequency splitting (~ 12 kHz) gives a residual magnetic field of ~ 17 mG.

⁽³⁾here we have $g \equiv g_{F=2} \approx -g_{F=1} \approx \frac{1}{2}$.

⁽⁴⁾ref KUPA640720-10A

3.2 Optical dipole traps

The previous section discussed the role played by radiation pressure in magneto-optical trap mechanisms. There is in fact a second light force, coming from the interaction between light and the induced atomic dipole. In 1970, Arthur Ashkin proposed to make use of this force to trap small dielectric objects with the so-called optical tweezers [19]. This method is nowadays massively employed in chemistry, physics and biology to manipulate atoms [31], cells [32], etc. We take advantage of this force to first transport atoms from the 3D MOT to the science cavity and then to create a conservative potential for our atomic sample inside the resonator. The potential describing this effect takes a simple form for rubidium atoms when the detuning between the laser frequency and the optical transition is big compared to the hyperfine splitting [33]. It is then simply given by:

$$U(\vec{r}) = \frac{\pi c^2 \Gamma}{2\omega_0^3} \left(\frac{2}{\Delta_2} + \frac{1}{\Delta_1} \right) I(\vec{r}) \quad (3.8)$$

where \vec{r} is the position vector, $\Delta_{1,2} = \omega_L - \omega_{1,2}$ is the detuning between the laser of angular frequency ω_L , and the $D_{1,2}$ line with angular frequency $\omega_{1,2}$. Here, $\omega_0 \approx \omega_{1,2}$ because $\delta = \omega_1 - \omega_2 \ll \omega_{1,2}$ and it is assumed that light is linearly polarized. From Eq. 3.8, we see that atoms are attracted towards increasing intensity for red-detuned potential, $(2/\Delta_2 + 1/\Delta_1) < 0$, and repelled from high intensity regions in the case of blue-detuned potential, $(2/\Delta_2 + 1/\Delta_1) > 0$. From now, we will only consider red-detuned optical dipole traps.

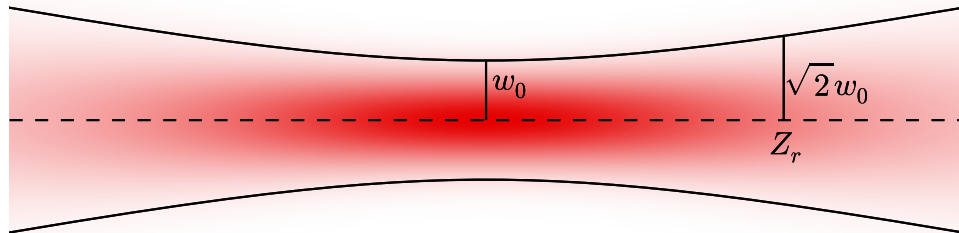


Figure 3.8: Gaussian beam. Gaussian beam intensity of w_0 waist in red. $w(z)$ is plotted in black as a function of z . For a red-detuned beam, a dielectric object is attracted towards the maximums of the intensity, here in the waist.

The propagation of a beam in the small-angle approximation obeys the paraxial wave equation discussed in more details in Chapter 2. One solution to this equation is the Gaussian beam corresponding to the profile of our laser beams and to the output mode of our single-mode optical fibers. For such a light beam with a wavelength λ , the intensity profile is:

$$I_1(z, r) = I_0 \left(\frac{w_0}{w(z)} \right)^2 e^{-2r^2/w(z)^2} \quad (3.9)$$

where $r = \sqrt{x^2 + y^2}$ is the radial coordinate, $w(z) = w_0 \sqrt{1 + (z/z_r)^2}$ is the spot size parameter and z_r is the Rayleigh range. For instance, in the case of a single beam and in the limit where $z/z_r \ll 1$ and $r/w_0 \ll 1$, one recovers a harmonic trap in the three directions:

$$U(r, z) \approx -U_0 + \frac{1}{2} m (\omega_z^2 z^2 + \omega_r^2 r^2) \text{ with } \omega_r = \sqrt{\frac{4U_0}{mw_0^2}}, \omega_z = \sqrt{\frac{2U_0}{mz_r^2}} \quad (3.10)$$

where ω_r and ω_z are the radial and longitudinal angular frequencies associated to the trap and U_0 is the absolute value of the potential in its center $U(0, 0)$. This elementary solution corresponds to an optical tweezer.

This process takes its origin from light refraction induced by the small dielectric medium, causing a change in the momentum of the light. The law of action and reaction implies that the small particle is also subjected to an equal and opposite force. As it is, there is no absorption of light in this process. However, the frequency detuning has a large but finite value and therefore the absorption probability is not zero. This phenomenon increases the velocity of our atoms and eventually induces losses. We can define a spontaneous emission rate, equivalent to heating rate, to take this effect into account. For Alkali atoms its expression is :

$$\Gamma_{sc}(\vec{r}) = \frac{\pi c^2 \Gamma^2}{2 \hbar \omega_0^3} \left(\frac{2}{\Delta_2^2} + \frac{1}{\Delta_1^2} \right) I(\vec{r}) \quad (3.11)$$

This rate has to be as small as possible if we want to trap atoms with an optical tweezer and this is even more true if we want to keep them in a specific atomic state. For high detuning values, where $\Delta_1 \approx \Delta_2$, there is a simple scaling factor between this quantity and the trap depth: $\hbar \Gamma_{sc} = \Gamma U / \Delta$ where $U \propto 1/\Delta$. There is an obvious advantage to go as far as possible to bring this rate as close to zero as possible. However, the finite amount of available power for our dipole traps imposes a trade-off depending on the context and needs.

3.2.1 Conveyor belt

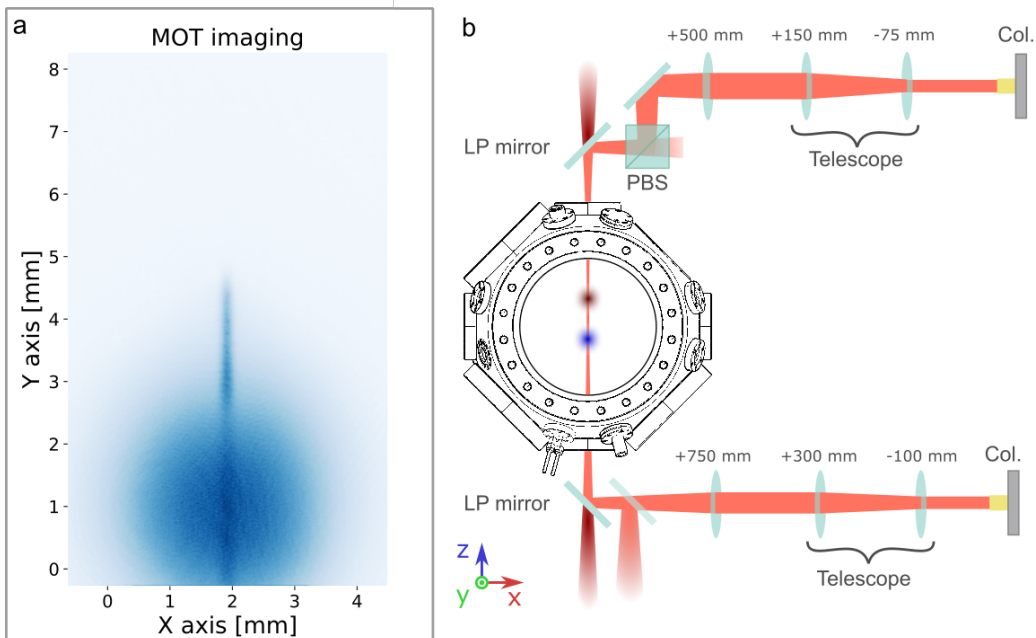


Figure 3.9: Conveyor belt. a- Our conveyor belt leaving the Magneto optical trap (imaging of the MOT). b- Optical setup. Lenses focal lengths are indicated. Col.: collimator. PBS: polarized beam splitter. LP: 900 nm Low-pass mirror. The conveyor beams are sent to the chamber table through two fibers and are collimated by two Schäfter and Kirchhoff collimators with an output waist of 1 mm. For each arm, a telescope adjusts the size of the beam and a third lens focuses the light in between the resonator and the 3D MOT with a 70 μm waist.

33 mm separate the atoms inside our 3D MOT from the optical cavity. Two counter-propagating beams along the vertical axis are used as a dipole trap to transport atoms over

this distance. We will now call it conveyor belt and the intensity profile is :

$$I_{conv}(r, z) = 4I_0(r, z) \cos(kz - \delta\omega t/2 + \phi)^2 \quad (3.12)$$

Here, it is assumed that the two beams have the same intensity I_0 . k is the wave vector modulus, ϕ a phase, and $\delta\omega = \omega_1 - \omega_2$ a frequency detuning. The taper-amplified Toptica laser used to produce this dipole trap is tuned between the D_1 and D_2 line at $\lambda = 782.9$ nm, in the red-detuned regime. This configuration corresponds to a 1D lattice of trapping along the z axis. The maximum available power in one arm is 250 mW with a 70 μm waist leading to $z_r = 19$ mm. To obtain a good overlap of the conveyor with the MOT but also between the two arms, we first align the lower arm of the conveyor on the MOT with a camera placed on the upper arm. Once this is done, the upper part is adjusted by maximizing the coupling of light in the lower collimator, see figure 3.9.

Transport

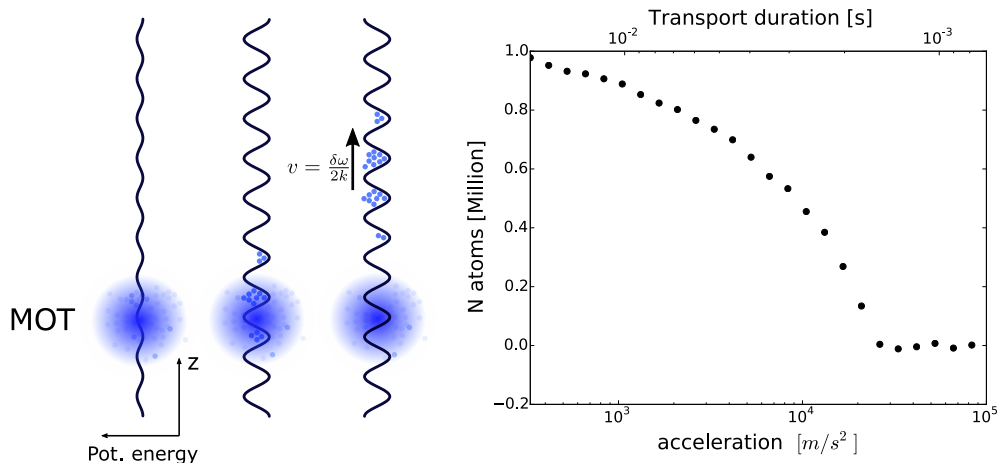


Figure 3.10: Transport with the conveyor belt. Left- illustration of the transport step. First, the conveyor belt amplitude is ramped up to trap atoms at the MOT position. We then shift the frequency of the lower arm, $\delta\omega$, to induce a displacement at a velocity $v = \delta\omega/(2k)$. Right- the number of atoms at the resonator level as a function of the acceleration, or equivalently the transport duration.

If we consider the situation where $\delta\omega \neq 0$, the intensity maxima move at a velocity $v = \delta\omega/(2k)$ and take away the cloud just as a conveyor belt would do. This method ensures fast transport of a high amount of atoms, $\sim 10^6$, with a high density $\sim 1 \times 10^{11} \text{ cm}^{-3}$ and reasonable temperature $T \approx 50 \mu\text{K}$ for a symmetric configuration (i.e. where the waist is placed halfway, see next sub-section). During transport over a distance d , atoms are first accelerated with a frequency sweep $\delta\omega = Rt$ during a t_0 time and then decelerated with the same slope R during t_0 . In those conditions, atoms undergo an acceleration $a = d/t_0^2$. Of course, we want the transport step to be as short as possible but diminishing the step duration increases the acceleration. In the reference frame of an atom, the acceleration shifts the potential by a linear term in z and thus reduces the depth of the trap in one direction [34]. We measured the number of transported atoms versus the total duration of the step $t_{tot} = 2t_0$ and found a good compromise at $t_{tot} = 10$ ms, shown in figure 3.10.

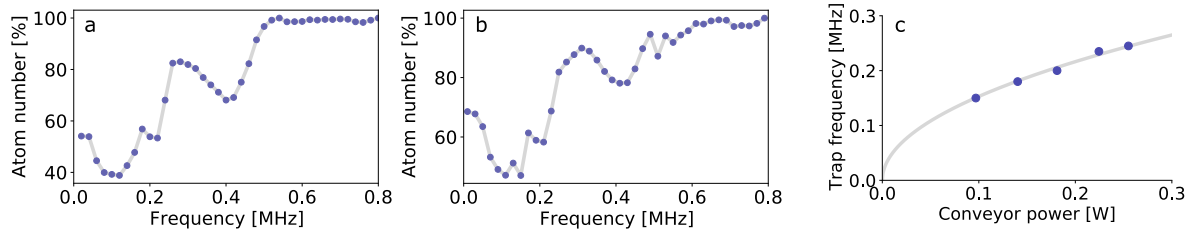


Figure 3.11: Longitudinal frequencies . a- Amplitude modulation of the lower arm at full power with atoms close to the 3D MOT. The atom number is recorded by the MOT camera for several values of the modulation frequency. A resonance is visible at 420 kHz corresponding to twice the trapping frequency. b- The same plot but at the cavity level. We observe the same resonance as expected for a waist located halfway between the MOT and the resonator. c- Trap frequency as a function of the power $P \propto U_0$ in the MOT, the fitting function is $C_{ste}\sqrt{P}$. Note: this plot was taken before adjustment of the waist position; actually the maximum frequency is above 210 kHz.

Longitudinal trapping frequencies

Let us now look at the $\delta\omega = 0$ case where the two beams form a standing wave. We want to check that the focus of our conveyor belt is halfway between the 3D MOT and the science cavity to reduce the compression-induced heating while transporting enough atoms. In this case, the longitudinal trapping frequencies should be identical at the MOT and cavity positions. This information is also important for the Raman cooling step described in the next section.

One can expand the cosine function around a maximum at a distance z of the waist position. The longitudinal frequency is then $\omega_z = k\sqrt{2U_z/m}$, where $U_z = U_0/(1 + (z/z_r)^2)$ is the trap depth at position z ⁽⁵⁾, constant over the typical length of the trap since $z_r \gg \lambda$. The radial frequency at a distance z is obtained from Eq. 3.10 by substituting U_0 with U_z and the waist w_0 by the spot parameter $w(z)$: $\omega_r = \sqrt{4U_z/(mw(z)^2)}$.

The longitudinal frequency can be measured by mean of parametric heating. The intensity is modulated at a given frequency which induces losses when this frequency corresponds to twice the trapping frequency [35]. It is visible in figure 3.11 where we measured the frequency both in the MOT and inside the science cavity. At full power, the longitudinal trapping frequency value is 210 kHz in the MOT and at the science cavity level. This indicates that the waist of the beam is indeed standing in between the 3D MOT and the science cavity. We don't have access to the radial frequency with this method because it is too small ($\omega_r/\omega_z = \sqrt{2}/(kw(z)) \ll 1$).

3.2.2 Crossed-dipole trap

Once atoms are transported inside the cavity, we want to confine them within a unique blockade volume. For $n = 100$ Rydberg state, the interaction coefficient is $C_6 = 56 \text{ THz}/\mu\text{m}^6$ corresponding to a e^{-2} radius⁽⁶⁾ of 14 μm for a 2 MHz linewidth. We thus employ two crossing beams at 1064 nm with opposite polarizations to avoid interference. This is equivalent to two superimposed optical tweezers as mentioned in the introduction of this section. The trap is loaded after a step of degenerate Raman sideband cooling to reduce the temperature of the cloud to 2 – 3 μK (see the next section). We are thus able to reduce the depth of the trap to 25 $\mu\text{K} = U_0/k_b$ and we can directly probe the atomic sample inside the trap since the differential light shift is about 60 kHz for atoms at 3 μK . Another advantage of the Raman cooling step is to increase the density by alternatively cooling and compressing. In our case

⁽⁵⁾Here $z = 0$ is the position of the waist.

⁽⁶⁾the distance at which the atomic density distribution falls to $1/e^2$ of its maximum.

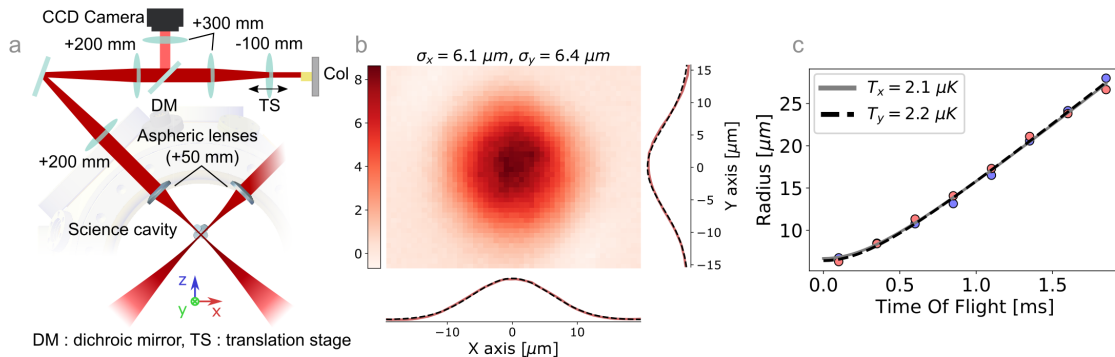


Figure 3.12: 1064 nm **crossed-Dipole Trap**. a- Optical setup: two beams are focused at the science cavity position by two aspheric lenses placed inside the main vacuum chamber. The first lens after the collimator stands on a translation stage to adjust the size of the beam at the crossing point. Those two in-vacuum lenses are also used for a high-resolution imaging of the small cloud. b- High resolution imaging: imaging after a $100 \mu\text{s}$ time-of-flight. The color bar on the left gives the atomic density integrated along the optical path in μm^{-2} . c- Temperature : estimation of the temperature after a sequence of degenerate Raman sideband cooling followed by a 50 ms waiting time inside the dipole trap.

we managed to reach an atomic density of $4 \times 10^{11} \mu\text{m}^{-3}$ in the small 1064 trap. In practice, each beam is made of 60 mW focused on a $10 \mu\text{m}$ waist resulting in a $13 \mu\text{m}$ radius for the atomic density distribution as shown in figure 3.12. Notice that we are able to adjust the radius of the cloud from $14 \mu\text{m}$ down to $10 \mu\text{m}$ by tuning the position of a lens attached to a translation stage in each arm⁽⁷⁾.

⁽⁷⁾We are here limited by the density and the need to keep a thousand atoms within the trap to maintain a sufficient atom-cavity coupling ($\approx 10 \text{ MHz}$).

3.3 Degenerate Raman sideband cooling

The degenerate Raman sideband cooling (DRSC) technique consists in the accumulation of atoms in the vibrational ground state of an isotropic three-dimensional trap [36]. Recently, an all optical cooling technique reaching quantum degeneracy has been demonstrated with this method [37] and has proven to be very efficient to get past the temperature lower bound set by light diffusion in dense atomic gases. With a few micro Kelvin cloud, the contribution of the Doppler effect to the inhomogeneous broadening of the Rydberg linewidth is negligible. The latter is a crucial parameter that sets the level of electromagnetically-induced transparency, the dynamics of our polaritons and the blockade volume. It also enables us to probe the cloud directly in the small crossed dipole trap at 1064 nm as the trap depth can be reduced to 25 μK and thus reach a satisfying differential light shift value ($\lesssim 60 \text{ kHz}$).

3D optical lattice

As mentioned in the introduction, atoms have to be trapped in a 3D optical lattice. More precisely, atoms must be in the Lamb-Dicke regime where the recoil energy, induced by light, is much smaller than the energy spacing of the trap $\hbar\omega_t$. In this limit, the energy transferred by one absorption process is negligible compared to the trapping strength. It is concretely expressed by the condition:

$$\eta^2 = \frac{E_R}{\hbar\omega_t} \ll 1 \quad (3.13)$$

where the recoil energy is simply $E_R = \frac{\hbar^2 k^2}{2m}$ and k is the wave vector modulus of the electromagnetic field transferred to an atom. In other words, the coupling of the electromagnetic field with the motion of an atom can be treated as a perturbation of the trapping Hamiltonian. The ordering is given by the η parameter and consequently the first non trivial term of this perturbation involves a change of one motional quantum only.

In our case the 3D lattice is made of the conveyor belt light for the confinement along the z axis, in addition to four others beams with a 150 μm waist to ensure confinement within the (x, y) plane. The first pair of beams comes along the diagonal MOT beams with a polarization parallel to y to trap atoms in the x direction and $\sim 3 \text{ mW}$ in each arm. On top of that, the second pair propagates in the (x, y) plane with a polarization along z with $\sim 10 \text{ mW}$ per beam. One of its arms makes an angle $\theta = 21^\circ$ with the y axis, while the other arm is tilted by the same amount but in the other direction. The full configuration is depicted on figure 3.13.

The set of beams for the horizontal lattice comes from a DL pro, phase locked 16 GHz above the $F = 2 \rightarrow F' = 3$ hyperfine D_2 line on the Repumper DL pro at 780 nm. The two pairs are spectrally separated: each goes through a 110 MHz double pass AOM but aligned on opposite orders, leading to a 440 MHz shift. On one hand, the relatively small detuning on both the D_1 and D_2 lines reduces the amount of necessary trapping power. On the other, it induces an important spontaneous scattering that limits the lifetime within the trap. We work with a blue-detuned lattice where atoms are attracted towards minima of the electromagnetic field to reduce this effect. Since the 3D lattice is also responsible for the Raman process, one could think that it also reduces the Raman rate, but we will see that it is not true. Despite the blue detuning, the trapping lifetime is still short (about 3 ms). Atoms are thus only loaded in this 3D lattice during a cooling process where the Raman cooling rate overcomes the heating. Finally, the power in each beam is adjusted such that the trap is isotropic. The trapping frequency in each direction is estimated by the parametric heating method introduced in the previous section. We have fixed its value at 180 kHz to ensure that atoms stand in the Lamb-Dicke regime, the typical recoil energy being of the order of $E_R/h = 10 \text{ kHz}$.

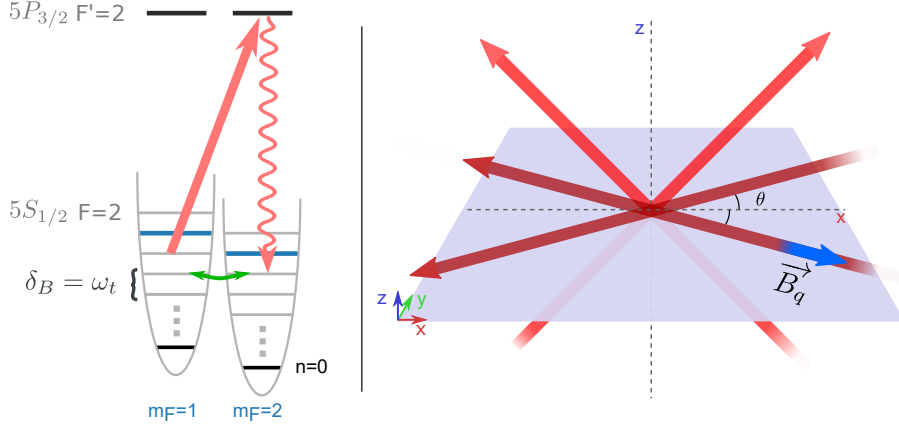


Figure 3.13: Degenerate Raman Sideband Cooling. Left- A magnetic field is adjusted to induce a Zeeman splitting in $5S_{1/2}, F = 2$ equal to the trapping frequency of our isotropic 3D trap. Thereby, Raman transitions (in green) can transfer an atom between $|F = 2, m_F - 1, n - 1\rangle$ and $|F = 2, m_F, n\rangle$. A $\sigma+$ polarized beam (red arrow) ensures optical pumping in the stretched state $5S_{1/2}, |F = 2, m_F = 2\rangle$ without affecting the vibrational state of the atom. The combination of the two is equivalent to an optical pumping with a dark state corresponding to the stretched state in the lower vibrational state of the trap, $|F = 2, m_F = 2, n = 0\rangle$ (black line). Right- Sketch of the four blue-detuned beam that ensure trapping in the (x,y) plane. The first pair in light red extends in the (z,x) plane with a polarization along y. The second pair is contained in the (x,y) plane with a polarization towards z.

Raman transitions

The second ingredient for DRSC is the magnetic field. It has to be tuned to induce a Zeeman splitting matching the trapping frequency for atoms pumped in $5S_{1/2} F=2$. The magnetic field magnitude, around 150 mG, makes it necessary to properly compensate residual magnetic field at the cavity level. We employed the same technique as in the 3D MOT (more details in 3.1.2 Magnetic field compensation). When this condition is fulfilled, trapping light can also induce Raman transitions from $|F = 2, m_F, n\rangle$ to $|F = 2, m_F - 1, n - 1\rangle$, n being the quantum number associated to the trap. The Hamiltonian describing this phenomenon, in the far-detuned regime ($\Delta_{1,2} \gg \Delta_{HF}$ ⁽⁸⁾, for rubidium and Alkali atoms is [38, 39]:

$$\hat{H}_R = \frac{id_1^2}{12\hbar} \left(\frac{1}{\Delta_1} - \frac{1}{\Delta_2} \right) \frac{\hat{\mathbf{C}} \cdot \hat{\mathbf{F}}}{\hbar F} \quad (3.14)$$

with $\hat{\mathbf{C}} = \mathbf{E}^*(\hat{r}) \times \mathbf{E}(\hat{r}) = i \operatorname{Im}(\mathbf{E}^*(\hat{r}) \times \mathbf{E}(\hat{r}))$ where \mathbf{E} is the complex electric field. One sees that it is possible to couple different sublevels m_F with operators \hat{F}_+ and \hat{F}_- by a careful adjustment of the vector $\hat{\mathbf{C}}$. Thus, the Raman light induces transition with $\Delta m_F = \pm 1$ as one can expect in the far-detuned regime where the relevant spin coupled to light is a spin 1/2⁽⁹⁾. Here, the scaling with respect to the frequency detuning is different from the dipole trap potential and goes to zero more rapidly. This is another reason why our Lattice beams are closer to one resonance as they also aim to produce Raman transitions.

Let us take the example of a pair of plane waves with linear polarization and the same intensity for simplicity. In this case, the complex electric field can be written as:

$$\mathbf{E}(r) = \mathcal{E} e^{i\phi_1(r)} \mathbf{u}_1 + \mathcal{E} e^{i\phi_2(r)} \mathbf{u}_2 \quad (3.15)$$

⁽⁸⁾ Δ_{HF}) is the hyperfine splitting of the two excited states $5P_{1/2}$ and $5P_{3/2}$.

⁽⁹⁾ J is the good quantum number and $J = 1/2$ in the ground state. A Raman transition can be written $|J, m_j^{(i)}\rangle \rightarrow |J', m_j'\rangle \rightarrow |J, m_j^{(f)}\rangle$ and thus $\Delta m_F = \Delta m_J = 0, \pm 1$.

where \mathcal{E} is the amplitude, $\phi_j(r) = \mathbf{k}_j \cdot \mathbf{r}$ and \mathbf{u}_j is a unitary vector along the j^{th} electric field. Consequently, the vector \mathbf{C} is simply:

$$\mathbf{C} = 2i \sin \theta |\mathcal{E}|^2 \sin \delta_\phi(r) \mathbf{u}_\perp \quad (3.16)$$

where θ is the angle between \mathbf{u}_1 and \mathbf{u}_2 , $\mathbf{u}_\perp = (\mathbf{u}_1 \times \mathbf{u}_2) / \|\mathbf{u}_1 \times \mathbf{u}_2\|$ and $\delta_\phi(r) = \phi_1(r) - \phi_2(r) = \|\mathbf{k}_1 - \mathbf{k}_2\| r_\parallel$ is the phase difference between the two optical beams.

If we expand the spatial contribution at the bottom of a blue-detuned trap and re-express the operator position with creation/annihilation operators $\hat{r}_\parallel = \sqrt{\hbar/(2m\omega)}(a + a^\dagger)$, we get the following expression for the Raman Hamiltonian at lowest order:

$$H_{Raman} = \Omega_R a^\dagger \hat{F}_+ + \Omega_R^* a \hat{F}_-, \quad \Omega_R = \frac{\eta d_1^2 |\mathcal{E}^2|}{6\hbar^2 F} \left(\frac{1}{\Delta_1} - \frac{1}{\Delta_2} \right) \sin \theta (u_x - i u_y) \quad (3.17)$$

where we have introduced ladder operator of the angular momentum $\hat{F}_\pm = \hat{F}_x \pm i \hat{F}_y$, ignored the term proportional to \hat{F}_z because it is off resonant as it only changes the quantum number associated to the trap, and used the Lamb-Dicke parameter $\eta = \|\mathbf{k}_2 - \mathbf{k}_1\| \sqrt{\hbar/(2m\omega)}$. Notice that this expression is identical for a red-detuned trap, while we might naively expect that Raman transitions are much more important at an intensity maximum. The optimal angle θ is a trade-off between the need to have interference to produce a trapping lattice scaling in $\cos(\theta)$ and the associated Raman rate directly proportional to $\sin(\theta)$. In practice, we use a small angle to ensure that the trapping dominates and the angle θ is optimized experimentally. This is performed thanks to a 10° tilted half-wave plates on three of our trapping beams to independently optimize the Raman rate along the three directions. Each pair of beams of the optical lattice contributes independently to the Raman process as they are all spectrally separated by at least 400 MHz. Crossed contributions are rapidly oscillating and averaged to zero in front of the trapping frequency.

Simultaneously, a $\sigma+$ polarized pump drives the D_2 transitions from $|F = 2, m_F = 1, n - 1\rangle$ to $|F' = 2, m_F, n - 1\rangle$. Atoms can be transferred by spontaneous decay back to states in $5S_{1/2}$: $|F = 2, m_F, n - 1\rangle$ or $|F = 2, m_F \pm 1, n - 1\rangle$ while a repumper beam maintains atoms in $F = 2$ to avoid losses in $F = 1$ state. The overall technique decreases the quantum number n and eventually leads to the dark state $|F = 2, m_F = 2, n = 0\rangle$ where no Raman transition is possible.

Experimental result

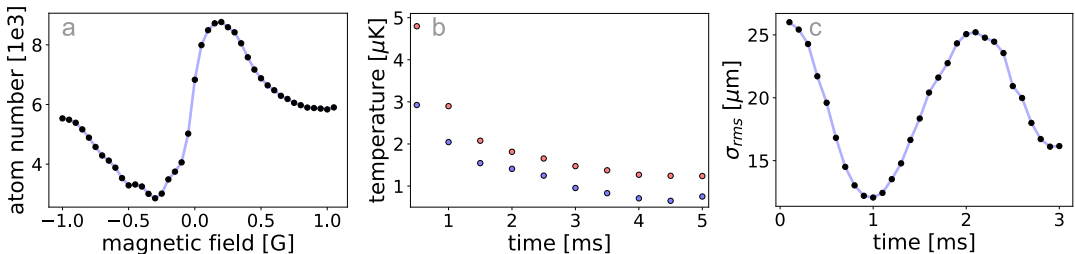


Figure 3.14: Optimization of the cooling and compression. a- We measure the number of remaining atoms as a function of the magnetic field applied in a 5 ms Raman cooling step. A broad resonance is visible for a positive magnetic field (0.05-0.3 mG) corresponding to efficient raman cooling while we observe an anti-resonance for negative values corresponding to an anti-Stokes configuration that heats the atoms . b- Temperature vs. cooling time. It saturates around $1.2\mu K$. The temperature is measured along the two transverses axes of one of the high-resolution imaging (vertical in blue and horizontal in red). c- After 5 ms of Raman cooling we turn off the blue-detuned lattice to observe the compression in the conveyor belt. The best compression is obtained after 1 ms in the trap.

The experimental sequence is an alternation of Raman cooling and compression to both decrease the temperature and gain in density. The typical duration of a Raman step to significantly decrease the temperature is 1.5 ms, as shown on the figure 3.14, right panel. The magnetic field is set to 0.15 mG but the resonance is broad making this setting not critical. On the contrary, the polarization of the pump is a sensitive parameter to well define the dark state. It is adjusted by a zero-order quarter-wave plate placed right before the beam passes through the atomic ensemble. The power of the pump is at $\sim 2 \mu\text{W}$ and the beam is collimated with a 1 mm waist.

After this Raman cooling step, we can compress the cloud by rising the depth of our conveyor belt. Once atoms are down in the trap, a new sequence of Raman cooling is run. This compression timing is adjusted by looking at the evolution of the size of the sample, shown on figure 3.14. Between those compression and cooling steps, the Raman lattice is adiabatically raised up and down in 100 μs . By using the conveyor belt, we were able to compress the atomic sample within the (x,y) plane but it does not have a significant impact on the last direction. We were not able to compress with our blue-detuned Raman lattices because, as mentioned earlier, the heating in absence of cooling induces important losses. Instead, we put a compression beam within the (x,y) plane at 783 nm to obtain a compression along the third axis. The beam is loaded after a sequence including a step of cooling, compression in the conveyor and a second step of cooling. This second compression is again followed by a 5 ms Raman cooling step to further decrease the temperature down to $\sim 1 \mu\text{K}$ with our small crossed dipole trap on⁽¹⁰⁾.

⁽¹⁰⁾We also tested this step with the trap off but we did not observe a significant difference on the loading.

Conclusion

We have detailed the numerous steps and techniques used for the preparation of the atomic ensemble. It starts by the loading of the 3D MOT by the 2D MOT in $\sim 50\text{ ms}$ and its optimization to gain in density and reduce the temperature of the cloud via a compression ($\sim 1\text{ ms}$) and an optical molasses ($\sim 2\text{ ms}$). Those two steps help to increase the number of atoms transported to the science cavity by the conveyor belt. After those 10 ms of transport, the atomic sample is quite hot $\sim 50\text{ }\mu\text{K}$ and a degenerate Raman sideband cooling method is employed to decrease the temperature close to $2\text{ }\mu\text{K}$. This step is interspersed with compressions to gain in density. Finally, a crossed dipole trap at 1064 nm is loaded with a peak density at $n \simeq 4 \times 10^{11}\text{ cm}^{-3}$ and a small cloud width at e^{-2} : $\simeq 10\text{ }\mu\text{m}$.

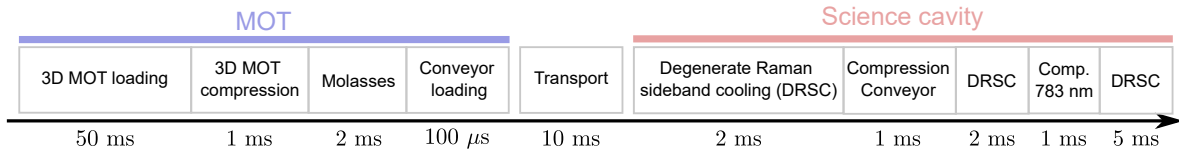


Figure 3.15: Sequence for the preparation of the atomic cloud. The sequence starts by the loading of the 3D MOT by the 2D MOT. It is then compressed and cool down to $9\text{ }\mu\text{K}$ in the molasses step. The conveyor belt is loaded and transports $\sim 10^6$ atoms to the science cavity. Once at the resonator level, the cloud is cool down to $\sim 1\text{ }\mu\text{K}$ and compressed to reach a peak atomic density of $4 \times 10^{11}\text{ cm}^{-3}$ inside the crossed dipole trap.

With those parameters, we expect the atomic ensemble to fit within a unique Rydberg blockade sphere for the targeted Rydberg states ($\sim 100S$) without too much broadening from the Doppler shift ($\sim 20\text{ kHz}$) or from the light shift induced by the crossed dipole trap ($\sim 60\text{ kHz}$). Thereby, the control of these critical parameters should allow us to obtain high electromagnetically-induced transparency as well as strong nonlinearities in our system.

Chapter 4

Detection for the atoms-cavity coupling

Contents

4.1	Detection setup	58
4.1.1	Homodyne detection	58
Principle		58
Wigner function reconstruction : maximum likelihood		59
Noise characterization		61
Phase lock		62
4.1.2	Intensity measurements	63
Avalanche photodiodes and single-photon avalanche diodes		63
Correlation measurements		64
4.1.3	Optical setup	65
4.2	Strong coupling regime	68
4.2.1	Optical pumping	68
Alignment		68
Optical pumping : population in $5S_{1/2}, F = 1$		69
4.2.2	Coupling to $ 5S_{1/2}, F = 1\rangle \rightarrow 5P_{1/2}, F = 2\rangle$	70
Experimental sequence		71
Transmission and reflection		72
Quadrature measurements		72

This short chapter aims at discussing the coupling between the science cavity and the small atomic ensemble. The science cavity is described in chapter 2 while the chapter 3 is dedicated to the preparation of the atomic cloud.

At first, the detection part of the experiment is introduced with particular emphasis on two methods: photon counting and homodyne measurements. In this section, the two techniques are presented together with their specific technical characteristics. The second section is devoted to the characterization of the strong coupling regime. Rubidium atoms feature many degenerated ground states at the hyperfine level. A quantization axis in addition to optical pumping allow to accumulate atoms in a single ground state. This step makes our cold atomic ensemble close to a perfect collection of two levels systems as described in the first chapter.

In particular, the purity of the optical pumping is estimated. We also discuss the alignment between the science cavity and the atomic cloud to finally characterize the coupling in several configuration: transmission, reflection and phase.

4.1 Detection setup

This section is a presentation of the detection part of our experiments. Since our work is based on the coupling between light and matter, we characterize our quantum system through the light that escapes from it. The two methods introduced here are an illustration of the complementarity of quantum mechanics. On one hand, a quantum state of light can be described by discrete ladder annihilation/creation operators (\hat{a}, \hat{a}^\dagger). In this case, the detector counts photons and the measurement is related to the particle-like behavior. The other approach of quantum mechanics is to rather consider continuous variables with quadrature operators ($\hat{x} = \sqrt{\hbar\omega/2}(\hat{a} + \hat{a}^\dagger)$, $\hat{p} = i\sqrt{\hbar\omega/2}(\hat{a} - \hat{a}^\dagger)$). These quantum observables are accessible with an Homodyne detection.

4.1.1 Homodyne detection

Principle

The basic idea of the Homodyne Detection (HD) is to obtain a measurement sensitive to the electromagnetic field of the probe and not its intensity. It was proposed by Yen an Chan in 1983 [40] and later demonstrated by Abbas Chan and Yee [41] during the same year.

Measuring the electromagnetic field in optics is an entire field of investigation, it is for instance used for imaging application to reconstruct the wavefront of a diffuser by holography techniques [42]. Here the method focuses on a the phase of a single optical mode. The signal of interest is combined with a reference laser beam called Local Oscillator (LO) to produce an interference term between the two. In our case, the probe is combined with the LO on a balanced unpolarized beam splitter and the two output channels are recorded with photodiodes. The local oscillator is used at high intensity and can be treated classically. Thereby, the difference between the two photocurrents is proportional to the field of both signals:

$$\hat{I}_1 - \hat{I}_2 \propto \|E_{LO}\| \hat{q}_\theta \quad (4.1)$$

where $I_{1,2}$ is the photocurrent of detector 1, 2, $\|E_{LO}\|$ is the modulus of the LO field, $\hat{q}_\theta = \cos(\theta)\hat{x} + \sin(\theta)\hat{p}$ is a quadrature of the probe and θ is the phase difference between the LO and the probe.

The quantum state to be characterized is usually very weak and this method allow to amplify the interference term via the LO power to extract the quantum signal out of the background noise. This makes homodyne detection very sensitive but this method requires the control of several parameters to ensure the stability during measurements.

First, the two output channels must be balanced to cancel out crossed contributions. Indeed, any residual offset will induces extra fluctuations over the weak signal. Another important quantity is the relative phase between the two beams. This phase must be controlled or at least measured, this issue is addressed in one of the following sub-section. Assuming these conditions are met, the probability distribution of a given quadrature is estimated from the accumulation of measurements. The acquired data are only proportional to the quadrature and a conventional way to normalize it is to fix the vacuum variance ($\langle 0 | \Delta \hat{q}_\theta | 0 \rangle$) to 1/2. Measurements on the experimental platform are performed with short pulses (from ~ 40 ns rms Gaussian pulses to ~ 100 μ s square pulses). The time envelope of the LO must be identical to that of the probe to ensure mode matching, but in practice we prefer to use a continuous oscillator to avoid drifts in the photocurrent. It is therefore necessary to post

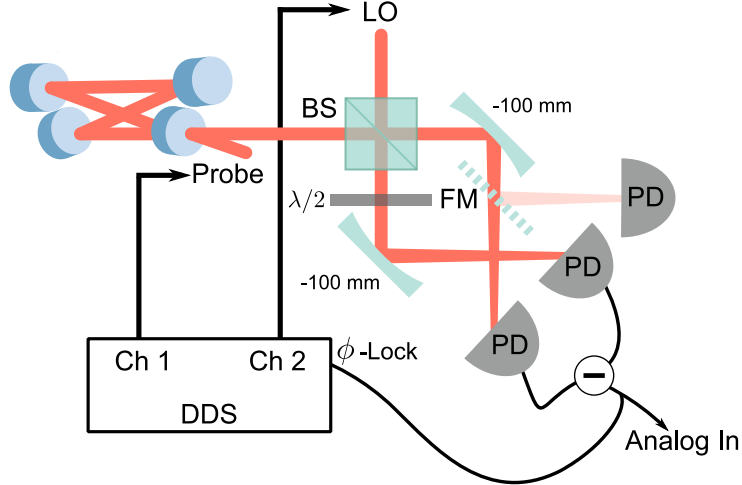


Figure 4.1: Homodyne detection. The local oscillator (LO) and the probe are combined on a 50:50 beam splitter (BS) and the output beams are focused by two mirrors ($f = -100 \text{ mm}$) before being recorded by two photodiodes. The output signal of the homodyne detection is the difference between the two photocurrents. The output signal of the homodyne detection is the substraction of the two photocurrents to keep only the interference term. A half-wave plate ($\lambda/2$) is there to make a fine balance to cancel cross contributions. A flip mirror (FM) can be switched to optimize the spatial overlap between the LO and the probe on a dedicated photodiode. The phase is also locked by sending the homodyne signal to the Direct digital synthesizer (DDS) that control our two beams (see text for more details).

select the appropriate temporal mode out of the continuous signal. This method will be illustrated in chapter 6.

The homodyne detection is well suited for phase-space reconstructions because it is possible to measure the probability distribution along two conjugate variables. Nevertheless, it is much more subtle than for classical physics since a point in the phase-space is not defined in quantum mechanics. Instead of a point, one can rather consider a surrounding as it is the case for instance with the Wigner function.

Wigner function reconstruction : maximum likelihood

The Wigner function is a phase-space representation of a quantum state and has been measured in many experiments [43, 44, 45, 46]. It is often presented as a phase-space probability except that it can take negative values. There is a univocal relation between this function (W) and the density matrix $\hat{\rho}$. The Wigner function is indeed given by:

$$W(x, p) = \frac{1}{\pi \hbar} \int_{-\infty}^{+\infty} \langle x + y | \hat{\rho} | x - y \rangle e^{-2ipy/\hbar} dy \quad (4.2)$$

The negativity of this function is associated to non-classical features of the state, it is therefore an interesting representation to characterize a quantum system [47]. The negativity of the function is however very fragile and it is lost for losses above 50% [48].

Some standard examples of Wigner functions are shown in figure 4.2. For instance, a single photon $|1\rangle$ takes negative values around $(0, 0)$ and shows no angular dependence. On the contrary, a coherent states $|\alpha\rangle$ describes a classical state (for instance a laser beam) and features no negativity in its Wigner function, it is simply a Gaussian at position $x = \text{Re}\{\alpha\}, p = \text{Im}\{\alpha\}$.

There is in fact a simple relation between the quadratures and the Wigner function. A

quadrature distribution rotated by the angle θ is simply the integration of the Wigner function along the orthogonal quadrature $q_{\theta+\pi/2}$. It is then possible to extract the Wigner function from its projection along several axes.

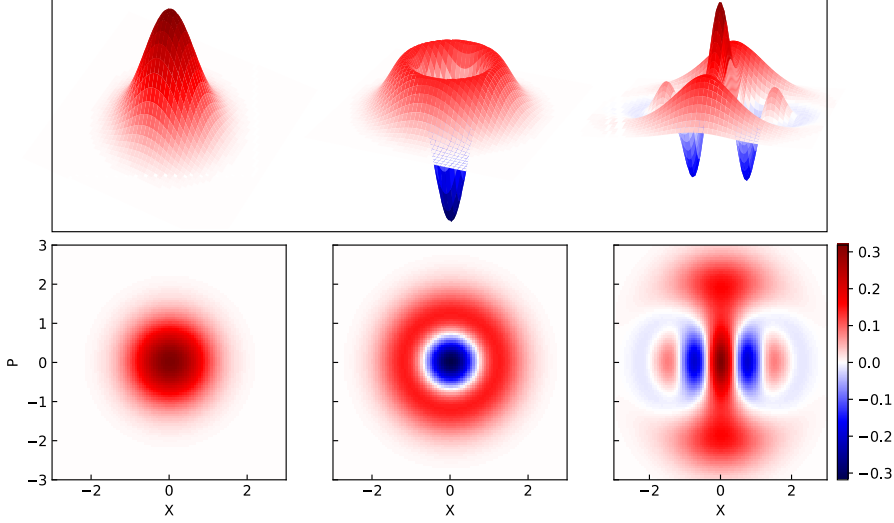


Figure 4.2: Wigner functions. Some examples of Wigner functions. From left to right: vacuum state $|0\rangle$, single-photon state $|1\rangle$ and even kitten states $(|\alpha\rangle + |-\alpha\rangle)/\sqrt{2}$ with $|\alpha|^2 = 2$. The vacuum state is a coherent state and thus exhibits no negativity (only red). The Wigner function of a single-photon state features negative values in the center (blue). A coherent superposition has a more complex Wigner function, it has interference fringes and oscillates between negative and positive values. The variance of the vacuum state is normalized to 1/2.

The standard method employed to reconstruct the Wigner function is an algorithm called maximum likelihood [49, 50]. This approach is based on the convergence towards the most likely density matrix ρ given the set of measured distributions [51]. First of all, the set of measurements obtained for a phase θ_k is discretized and organized into a histogram. The occurrence for a given bin x_j at phase θ_k is noted $m_{j,k}$. This quantity can be compared to the outcome of a given density matrix ρ . The probability to measure the bin x_j with the phase θ_k is $p_{j,k} = \text{Tr}[\hat{\Pi}(\theta_k, x_j)\hat{\rho}]$ where $\hat{\Pi}_{j,k}$ is the associated projector. Then, the probability of measuring this result $m_{j,k}$ times, assuming that the system was in the state ρ , is obtained by the formula $p(m_{j,k}|\rho) = p_{j,k}^{m_{j,k}}$. We have assumed here that the set of projectors form a complete basis for simplicity, we will come back to this assumption later. This can be extended to the entire data set to estimate the likelihood to observe the set of occurrences $\{m_{j,k}\}$ for a density matrix ρ :

$$\mathcal{L}(\hat{\rho}) = \prod_{j,k} p_{j,k}^{m_{j,k}} \quad (4.3)$$

The algorithm aims at maximizing this function to find the most likely density matrix. To this end, a new density matrix is defined iteratively from the previous one by the operation:

$$\hat{\rho}_{i+1} \propto \hat{R}(\hat{\rho}_i)\hat{\rho}_i\hat{R}(\hat{\rho}_i), \text{ where } \hat{R}(\hat{\rho}) = \sum_j \frac{m_{j,k}}{p_{j,k}} \hat{\Pi}_{j,k} \quad (4.4)$$

and ρ is normalized after each step. The initial density matrix is not very important, one can take for instance a thermal distribution. The key point here is that the most likely distribution should exhibit a proportionality between the probability and the data occurrences. It means that $\hat{R} \propto \hat{1}$. Thereby, we observe that it corresponds to a stationary point for the iterative step and it is possible to show that this operation converges towards this point [52]. For a

concrete implementation one need to restrict the size of the Hiblert space. An effective way to do this is to express all the operators in the Fock states basis and to fix the maximal value of the photon number. Furthermore, we have previously assumed that the set of projectors is complete but this may seem impossible as we have truncated an infinite Hilbert space. This approximation remains valid as long as the investigation window is great in front of the state to be reconstructed. A preliminary guess of the density matrix is thus necessary to adjust the binning and the window length. This is not a big issue as we are investigating states with very few photons, at most 2 while the Hilbert space for our reconstructions is at least fixed to 5 photons and can be extended if necessary.

As we mentioned earlier, the losses on our system will deteriorate the Wigner reconstruction. Detection losses can be taken into account in the algorithm and corrected to obtain the Wigner function at the output of our system. Anyway, it is crucial to minimize all sources of losses and we now turn our attention to the noise of our homodyne detector.

Noise characterization

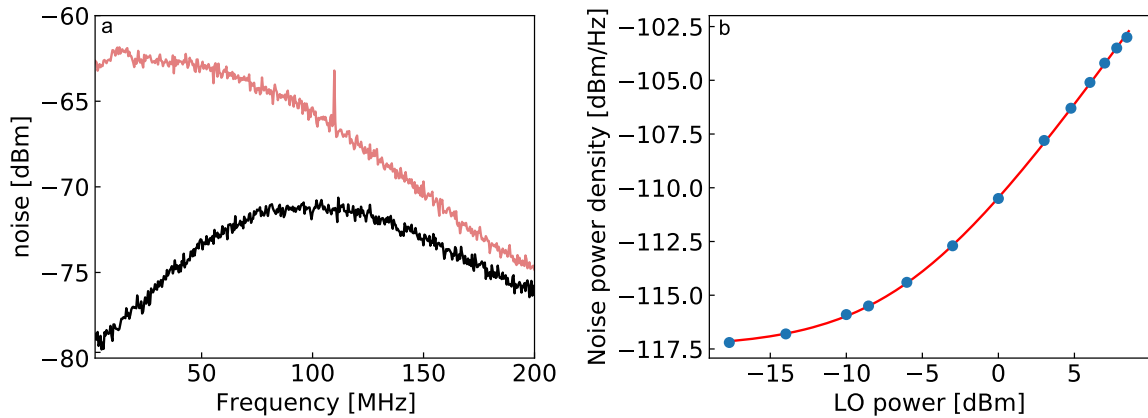


Figure 4.3: Noise. a- Noise spectrum for the homodyne detection alone (in black) and with the LO at 7 mW. The spectrum with 7 mW of LO is ~ 15 dB above the electronic noise over the detector bandwidth (100 MHz). b- Noise power density as a function of the LO power, measured at 20 MHz. The data set (blue dot) is fitted by the function: $10 \log_{10}(\sigma_P^0 + A \times P_{LO})$ (red curve) with A and σ_P^0 two free parameters and P_{LO} the LO power. The intrinsic noise is $\sigma_P^0 = 1.8 \times 10^{-12} \text{ mW Hz}^{-1}$ and corresponds to a noise-equivalent power of $10 \text{ pW}/\sqrt{\text{Hz}}$ (at 840 nm, Datasheet : $6 \text{ pW}/\sqrt{\text{Hz}}$ at 10 MHz).

The detection signal has to be shot-noise limited to faithfully capture a quantum state as extra-noise is the detection can be seen as additional losses [53]. The first source of noise comes from the electronics of the detector itself and the only way to reduce its impact is to increase the LO intensity. We are currently using the LO oscillator with about 7 mW close to the maximum for our photodiodes with a spectrum $\Delta S \sim 15$ dB above the electronic noise, as shown in figure 4.3. This ratio translates into a efficiency of detection given by $\eta_e = 1 - 10^{-\Delta S/10} \simeq 97\%$ while the efficiency of our photodiodes alone is $\eta_{PD} \simeq 91\%$. The second main issue is the balance between the two output channels. A half-wave plate is placed on one arm to make this compensation. The slight rotation of polarization induces a change of transmission through the glass plate in front of the sensor. This is possible because light is injected with a 20° angle⁽¹⁾ on our photodiodes. Despite this fine tuning, we observed slow drifts throughout our experimental cycles that results in a low frequency noise (~ 100 kHz). This can be attributed to fluctuations of the intensity due to polarization or temperature

⁽¹⁾The reflectivity depends on the incident angle.

drifts. A long reference signal is regularly acquired to properly define the zero and thus to eliminate this additional noise. This sample must be long (t_0) compare to the duration of the signal of interest (t_s) because the variances add up. The effective variance after this compensation (σ_{cor}^2) for the signal integrated over a duration t_s is:

$$\sigma_{cor}^2 = \sigma_{raw}^2 \left(1 + \frac{t_s}{t_0} \right) \quad (4.5)$$

where σ_{raw}^2 is the variance without offset correction. In practice, the ratio between t_0 and t_s is $\leq 1\%$. There is a third source of additional noise in our specific homodyne setup coming from the phase lock stability.

Phase lock

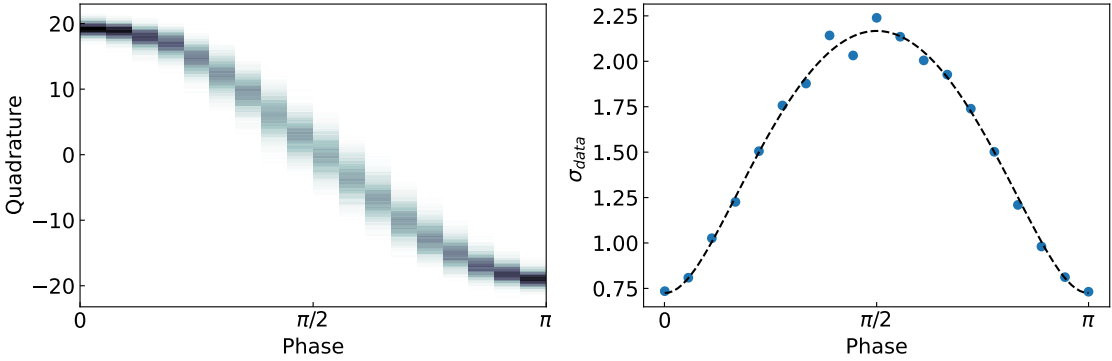


Figure 4.4: Phase stability. Left- Quadrature distribution as a function of the phase between the LO and a coherent state. The occurrence is represented from white (zero) to black (maximum). Right- The rms noise as a function of the input phase. We observe an important increase of this noise at strong intensity ($n_{phot} = \sim 200$). This additional noise is due to an imperfect lock of the phase. We have thus estimated the stability from those data with a fit: $f(\theta) = \sqrt{\sigma_0^2 + 2n\sigma_{ph}^2 \sin(\theta)^2}$ where σ_0 is the vacuum rms. The phase stability of our homodyne setup is $\simeq 6^\circ$.

The relative phase between the local oscillator and the probe defines the rotation angle of the quadrature. In some experiments, the phase is randomly fluctuating but slowly enough to be constant over each experimental cycle. The quadrature at a given phase can be reconstructed by measuring the phase for each measurement and post-selecting the data [54, 4]. In our case, we want an active control over this parameter to keep the phase stable throughout measurements.

This is possible thanks to an homemade phase lock, where a measurement of the relative phase is performed for each experimental cycle. Before homodyne measurement, the small residual offset of the HD is measured in the absence of any probe signal. The probe beam is then switched on to acquire the quadrature at a random phase. Afterwards, the phase is $\pi/2$ shifted and the second quadrature is measured. Finally, the offset is subtracted for both quadratures to estimate the relative phase. Those operations are performed in 400 μ s by a FPGA and the corrected phase is then sent to the DDS driving the probe and the local oscillator. This measurement is performed with the laser beams 40 MHz away from the atomic resonance (and the cavity resonance⁽²⁾) to not disturb or kick out our atoms. The difference of optical path between the local oscillator and the probe induces a phase shift when the

⁽²⁾The cavity is resonant with the $|5S_{1/2}, F = 1, m_F = 1\rangle \rightarrow |5P_{1/2}, F' = 2, m_{F'} = 2\rangle$ Rubidium transition in almost all the experiments presented in this manuscript

frequency is changed after the phase-lock step to go back close to the resonance. This shift is calibrated by looking at the frequency shift needed to observe a 2π phase shift and it is automatically subtracted.

We also estimated the stability of the phase lock to be about $\sigma_{ph} = 0.11$ rad = 6.1° , as shown in figure 4.4. This estimation is obtained by measuring the noise for several values of the phase with a coherent states $|\alpha|e^{i\theta}\rangle$. The variance of the vacuum state is normalized to 1/2 as previously mentioned and the quadrature distribution is then given by Gaussian with a mean value $\langle \hat{q}_\theta \rangle = 2|\alpha| \cos(\theta)$ along X axis and a variance $\langle \Delta \hat{q}_\theta \rangle = 1/2$. The additional noise is thus $\sigma_{add} = 2\sigma_{ph}\sqrt{n} \sin(\theta)$, where $n = |\alpha|^2$ in the mean photon number of the coherent state. The noise of the phase-lock constrains the photon number in order to keep the quadrature variance close to the shot-noise, $n \ll \frac{1}{4\sigma_{ph}^2} = 23$ and at $n = 1$ the additional noise is about 5%.

4.1.2 Intensity measurements

The other main method to extract information about our quantum system is to measure the intensity of the electromagnetic field. The field that escape from the cavity is usually very weak. For instance, the Rydberg blockade induces a saturation of the transmission flux at a few megahertz since at most one excitation can propagate through the resonator per polariton lifetime, see chapter 5. As an order of magnitude a 10 MHz photon flux at 780 nm is only equal to $\simeq 2.5$ pW. This make standard photodiodes unadapted. Instead, we make use of single-photon avalanche diodes (SPAD) and avalanche photodiodes (APD) depending on the context.

Avalanche photodiodes and single-photon avalanche diodes

Single-photon avalanche diodes (SPAD), also called Single-photon counting modules (SPCM), is one of the most standard device to records weak photon flux. Other approaches exist, for instance with superconductor nano-wires (SSPD) [55] or photomultipliers [56]. This kind of detectors are based on a nonlinear response of the system to produce a pulse for each incident photon, limited by the device's bandwidth. The output signal is therefore binary and this detection is dedicated to flux recording with access to the arrival time of photons (rising edge). In the case of SPAD, the nonlinearity comes from a silicon avalanche diode with a biased voltage far bellow the voltage breakdown to produce a strong current out of a single photon, as illustrated in figure 4.5. It makes this detection very fragile, the system is thermoelectrically cooled and its temperature is controlled to ensure a good stability.

Our modules (Excelitas (CD3583H)) has detection efficiency of 70% at 780 nm with a maximum count rate at ~ 20 MHz. The deadtime of our detectors is ~ 25 ns for an input rate below 1 MHz and the typical pulse width is ~ 20 ns. One key characteristic of such a detector is the darkcount rate: the excitation of an electron by the background induces a cascade effect and leads to a false positive click on the avalanche photodiode. For our detectors, the darkcount rate is announced at less than 100 Hz. However, we have observed that some of them have increased to ~ 300 kHz. Another artifact comes from the probability to observe a fictitious photon right after the detection of a real photon. Again, it depends on the quality of the device and our detectors have a probability of afterpulses at 0.1%. Two recording modes are possibles with the control system of the setup described in chapter 2. It is either done with time stamps at a 10 ns resolution or with an adjustable binning suitable for high-photon rates⁽³⁾. The first method is interesting for correlation measurements where the

⁽³⁾It reduces the total amount of data

arrival time of photons is important, see next subsection. The second approach is preferred when we record spectra of the resonator, the steady state of the system⁽⁴⁾, etc.

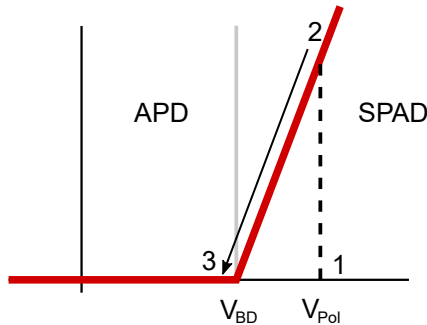


Figure 4.5: SPAD vs APD. Current-voltage characteristic of a diode. Below $V=V_{BD}$ (breakdown voltage) the system responds linearly with the input intensity. Avalanche photodiodes operate in this regime. On the contrary, a SPAD is used well above the breakdown point to produce a strong current out of a single photon. After the detection of a photon, a fast circuit decrease the biased voltage to kill the amplification.

There is currently one Laser Components avalanche photodiode (LCSA500-01) on our experiment. In this case, the biased voltage is maintained below the voltage breakdown to ensure the linearity with respect to the input flux. This avalanche photodiode is not often used but it is helpful to align and optimize the coupling between the cavity and our atomic sample. During this kind of procedure it is convenient to have a visibility at the single-shot level or close to it. If we assume that our measurements are shot-noise limited the signal to noise ratio scale is $\propto \sqrt{P}$, where P is the incident power. It is therefore interesting to increase the power and our single-photons detector are limited to ≈ 20 MHz.

Correlation measurements

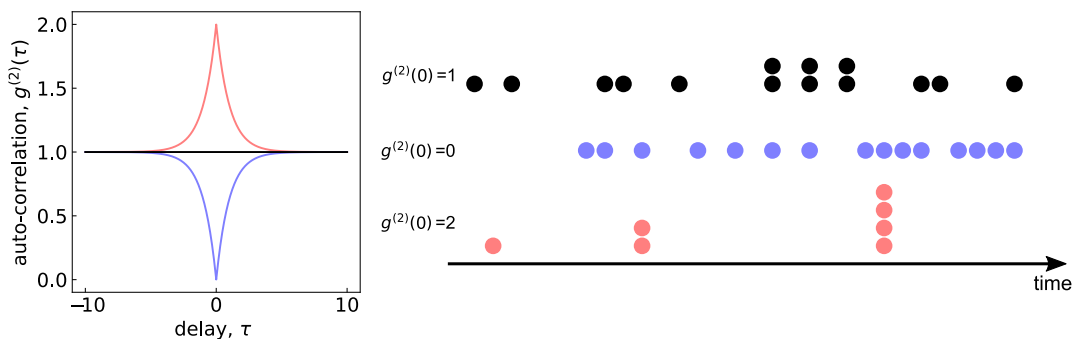


Figure 4.6: Photon statistics. Left- Second-order autocorrelation function ($g^{(2)}$) as a function of time. Thermal light (red curve) features a maximum at zero delay ($g^{(2)}(0) = 2$) while single-photons correlations exhibit on the contrary a minimum at $g^{(2)}(0) = 0$. A standard laser beam (black) has a flat correlation function. Right- The three configurations (same colors) randomly generated as a function of time. We see that thermal photons bunch while a single photon source is characterized by a clear separation between photons (anti-bunching).

Counting photons is a technical achievement on its own but more information can be extracted from the nature of light with this kind of devices. In particular, a SPCM return a click each time at least a photon is present in front of the detector but it is unable to

⁽⁴⁾See next chapter, for instance with saturation measurements induced by Rydberg blockade.

make a distinction between number states photons. Instead, it is possible to obtain the light's statistics by looking at correlations between the arrival time of photons on two SPCM detectors. The idea is to split the signal of interest in two on a beam splitter and to record coincidences between the two detectors. This corresponds to a measurement of the second order auto-correlation function:

$$g^{(2)}(t, t') = \frac{\langle \hat{E}_1^-(t) \hat{E}_2^-(t') \hat{E}_2^+(t') \hat{E}_2^+(t) \rangle}{\langle \hat{E}_1^-(t) \hat{E}_1^-(t) \rangle \langle \hat{E}_2^+(t) \hat{E}_2^-(t) \rangle} \quad (4.6)$$

where $\hat{E}^{+/-}$ is the positive/negative-frequency part of the electric field operator, the subset 1, 2 refer to the detector. The measurement is performed at time t on the first detector and t' for the second one. The function is normalized by the means photon number of both channels to impose $g(-\infty, +\infty)=1$ in the continuous regime. If we consider a single mode coherent state, we see that the correlation function is just equal to 1. Instead it vanishes for a single-photon state. The explanation for this is quite straightforwards: a single photon arriving on the beam splitter will either go to the first output channel or to the second one but it will be impossible to observe a click on both detector at the same time. When there is a continuous flux of single photons, coincidences becomes possibles but for a delay between the two paths matching the time separation between consecutive photons.

Historically, this kind of measurements was performed for the first time by Hanbury Brown and Twiss to measure the angular size of stars [57]. In their measurements, the two detectors were separated by an adjustable distance d to records light from a very distant source. They recorded the decrease of the second order auto-correlation as a function of the distance between the two detectors to estimate the coherence time of the source. This can be explained classically with a thermal state, i.e the superposition of several coherent states with random phases. In this case, the correlation function can be rewritten as :

$$g^{(2)}(\tau) = \frac{\langle I_1(t) I_2(t + \tau) \rangle}{\langle I_1(t) \rangle \langle I_2(t + \tau) \rangle} \quad (4.7)$$

where we have assume time invariance such that the auto-correlation only depends on the delay between the two detectors $t' - t = \tau$. Here, its purely classical statistics and since $\langle (I(t) - \langle I(t) \rangle)^2 \rangle \geq 0$ one see that $g^2(0) \geq 1$ and $g^2(0) \geq g^2(\tau)$. For a thermal light the autocorrelation rises to $g^{(2)}(0) = 2$ [58, 59] while one must recover $g^{(2)}(\tau) = 1$ when the delay exceed the coherence time of the source. In their experiment, they were limited by the detectors bandwidth and observed a $\sim 4\%$ increase of the auto-correlation at zero delay.

This approach can be generalized to n detectors to measure the n^{th} auto-correlation function of the electric field. A drop at zero delay would indicate a decrease of the probability to measure at least n photons at the same time, while a coherent state would always exhibit a flat response at 1.

4.1.3 Optical setup

The optical setup surrounding the cavity is separated in three tasks.

First, we have two technical beams. One is dedicated to lock the cavity's length. The second laser light is an optical pumping beam that is employed to control the hyperfine state of our atoms. They are sent in the opposite direction of the detection path to reduce the injection of parasitic light in our detection devices. The locking beam is at 783 nm with $\sim 1 \text{ nW}$ on a 1 mm waist and it is detected in reflection on a dedicated APD. . A Dichroic mirror (Semrock LL01-808, a few nm bandwidth) is placed in front of the APD to filter out the other beams, the locking technique and laser sources are introduced in the chapter 2.

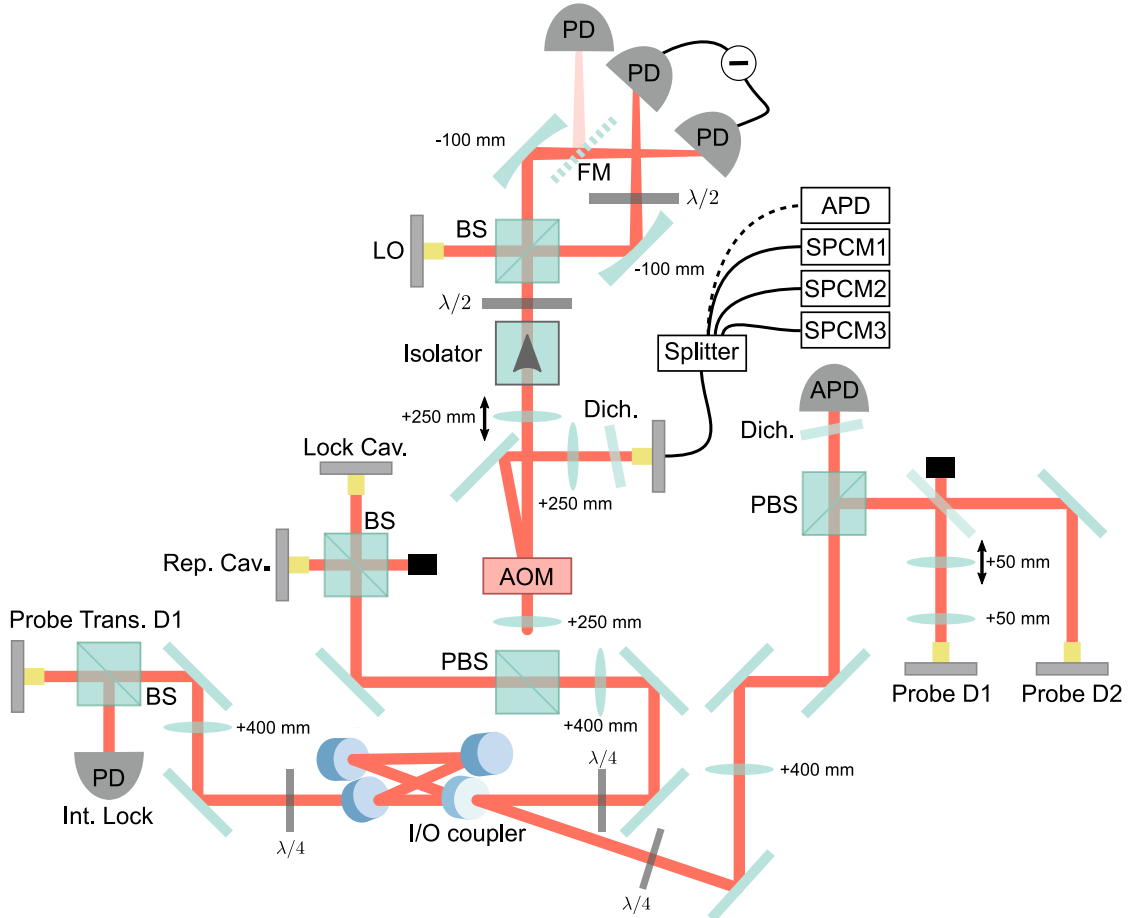


Figure 4.7: Probe and detection setup. Optical setup for the science cavity. The optical path of the detection can be switched with an AOM to either use the homodyne setup or a SPCM. 795 nm light is injected in transmission through an high-reflectivity mirror. Half of the signal is sent to a photodiode for an intensity locking. Two probe are injected in reflection at 795 nm (D_1) and 780 nm (D_2). The LO is currently at 795 nm and the probe D_2 is only used to create a Rydberg inside the cavity and is thus not detected. A dichroic mirror is placed in front of the SPCM fiber coupler to prevent the injection of this light beams. It is optimized at 795 nm with a bandwidth of a few nanometers (Semrock LL01-808).

The second part of the setup is made of laser beams to probes our science cavity. Two D_1 probes (795 nm) can be sent in reflection or in transmission to characterize the system {atoms + cavity}. The probe in transmission is thus injected from a high-selectivity (HR) mirror but it is not an issue because we work with weak photon flux (~ 1 MHz) as the system strongly saturates because of Rydberg blockade. This saturation effect is discussed in more details in chapter 1 and chapter 5. The intensity lock of this probe is visible on the figure 4.7, with a photodiode monitoring the intensity before the beam injection through the HR mirror. Note that all the probes are locked in intensity but it is not visible on the setup because it is done before the injection fibers. The beam in reflection is collimated with a telescope to optimize the mode matching with the science cavity TEM_{0,0} (translation stage on one lens). The third beam is the D_2 probe (780 nm) and is only used to coherently control a Rydberg excitation inside the resonator. This is a separate topic, which will be discussed in Chapter 7..

The last part is the detection path. the output light is sent through an AOM to switch between the detections introduced in the previous subsections. The light can be oriented towards our SPCMs or APD and it is filtered at 795 nm (Semrock LL01-808). It is distributed

by a home-made splitter, this is for instance used to make a balance between two SPCMs for correlations measurements. The other option is to make an homodyne detection with a LO currently at 795 nm. The lens before the detection can be translated to optimize the mode matching with the LO beam. This is done with the probe in transmission to directly optimize the mode matching with the science cavity mode. A Faraday isolator is placed right before the homodyne detection to reduce the diffusion of LO's light ($\sim 7\text{ mW}$) back in the cavity mode (20 dB decrease⁽⁵⁾). Notice that the D_2 probe is thus never detected.

⁽⁵⁾Initially, we observed about $\sim 6\text{ MHz}$ coupled back to the cavity mode and it is now at 40 kHz . We also removed the input and output cube of the isolator to reduce optical losses.

4.2 Strong coupling regime

Now that the detection paths and related detections techniques have been introduced, we turn our attention to the coupling between our small atomic cloud and the optical cavity. We will first discuss how to optimize the coupling and control the hyperfine state of the ultracold ensemble. We will give an estimation of the purity of the atomic cloud after a pumping step. This purity has a direct impact on the electromagnetically-induced transparency of the atomic cloud as atoms prepared in the wrong zeeman states can induce absorption. Finally, we briefly presents some measurements of the strong coupling regime in several configurations.

4.2.1 Optical pumping

Alignment

In the first chapter, we have described the response of an ensemble of two level systems coupled to a cavity. It is characterized by the coupling factor g called vacuum rabi splitting. In chapter 3, we have described the preparation of a small atomic ensemble at the cavity level but we did not discuss the alignment between the sample and the resonator. The first step to obtain this coupling is to align the conveyor belt with the $20 \mu\text{m}$ waist of the science cavity. To this end, the cavity's length is locked on one of the rubidium transition in order to monitor losses induced by the presence of atoms inside the resonator. This can be done by looking at the reflection or transmission of the cavity. The signal must be weak in order not to kick the cloud out of the cavity mode. Below this limit, it should be as powerful as possible to make the alignment easier. It is therefore acquired on the Laser Component APD introduced in the previous section.

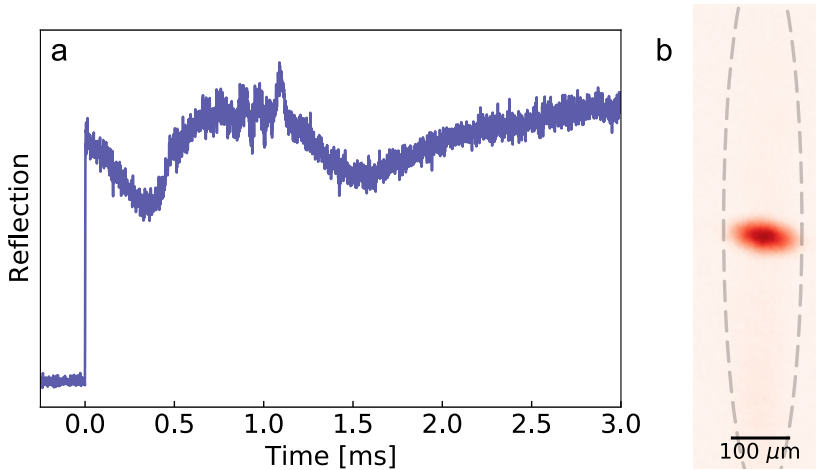


Figure 4.8: Atoms-cavity alignment. a- Measure of the cavity reflection to align the cloud with the mode of the cavity. At $t = 0$ the trap is switched off and light is sent through the cavity. We observe a decrease followed by an increase characteristic of the switch between Losses<Transmission regime to Losses>Transmission. b- Atoms inside the conveyor belt are pumped in $F = 1$ and we then sent light through the cavity to pump back atoms in $F = 2$ before imaging with $F = 2$ light to observe the position of the science cavity mode.

The cloud is released from the trap for a few milliseconds and spreads close to the cavity mode. The optimal position of the trap is then obtained when optical losses (due to absorption) are maximum at zero delay, as shown in figure 4.8. It corresponds to a coarse alignment that can be improved by directly looking at the rabi splitting once there is enough coupling.

The easiest way to measure the coupling is to switch to a transmission configuration. Since it only requires a small amount of power, light is injected from a high-reflectivity mirror and collected from the input/output mirror as we have discussed in the previous section. The coupled system's spectrum is measured by scanning the laser frequency around the cavity resonance (and the cavity is locked on one rubidium transition). Once this step is done, the vertical alignment is not at all precise because the cloud has a cigar shape inside the conveyor belt ($\sigma_z = 0.5 \text{ mm}$, $\sigma_r = 35 \mu\text{m}$) see chapter 3.

The idea is then to inject a large amount of light through the resonator to kick or pump atoms overlapping with the mode to estimate accurately the position of the cavity field with respect to the cigar shaped cloud. This hole, or the remaining atoms, are then observed with a beam addressing $5S_{1/2}, F = 2 \rightarrow 5P_{3/2}, F' = 3$ along the high-resolution imaging axis as shown in figure 4.8. It is thus possible to align our Raman beams and the 1064 nm crossed dipole trap on it. The final step consists in a slight adjustment of the two arms of the small crossed dipole trap to maximize the coupling of our small ensemble with the resonator.

Optical pumping : population in $5S_{1/2}, F = 1$

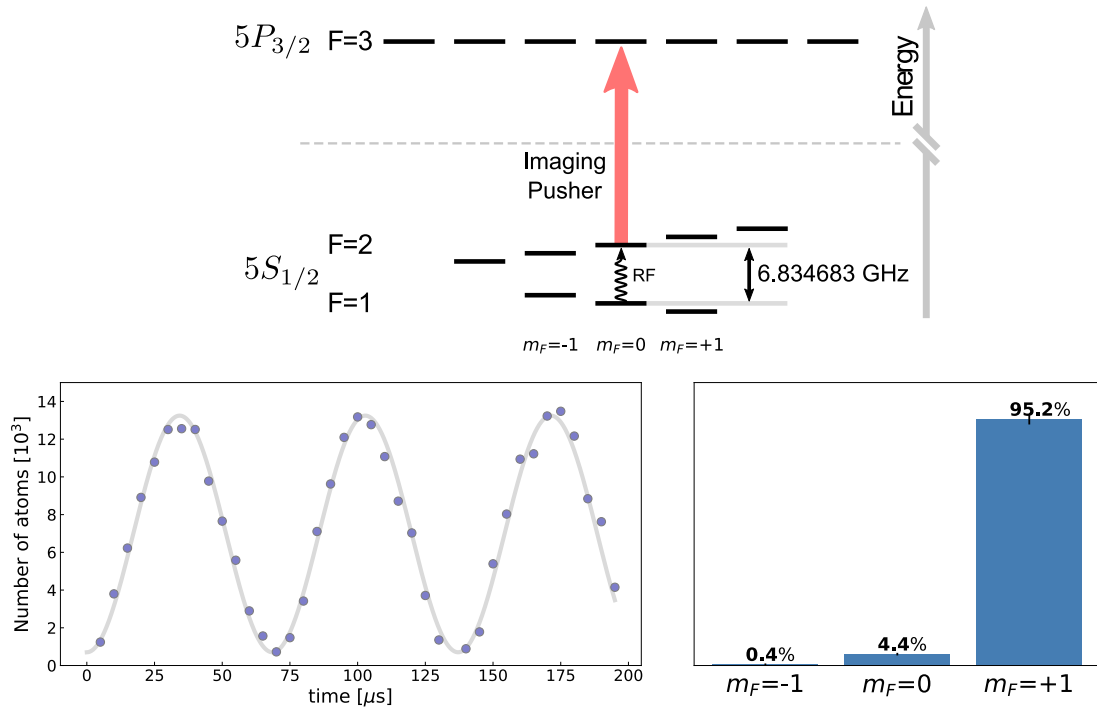


Figure 4.9: Optical pumping. Top- Schematic for $|F = 1, m_F = 0\rangle \rightarrow |F = 2, m_F = 0\rangle$ radio-frequency population transfer. Hyperfine lines are split by a 3 G magnetic field ($\simeq 2 \text{ MHz}$). Bottom left- Rabi oscillations between hyperfine states $|5S_{1/2}, F = 1, m_F = 0\rangle$ and $|5S_{1/2}, F = 2, m_F = 0\rangle$ by driving atoms with the RF antenna at 6.834683 GHz. We observe the number of atoms transferred to $|5S_{1/2}, F = 2, m_F = 0\rangle$ with our high-resolution imaging on $5S_{1/2}, F = 2 \rightarrow 5P_{3/2}, F' = 3$. This is done for the three Zeeman ground states of $5S_{1/2}, F = 1$ to estimate the population distribution. Bottom right- We apply RF π -pulse after a standard pumping step to estimate the purity of the optical pumping. After the pulse, we switch off the magnetic field before imaging to ensure an identical redistribution of the population between zeeman states of $5S_{1/2} F = 2$. We found that $95 \pm 2\%$ of the population is in $m_F = +1$ after our pumping sequence.

We have chosen to work with the probe on the D_1 line (795 nm) in order to easily filter it from Raman, conveyor and MOT beams at 780 nm. A magnetic field quantization of 3 G is switched on along the science cavity axis in order to address sigma transitions with the

circular polarizations through the resonator.. This impose to work with linearly polarized light for our control beams to address a single Rydberg state because of the geometry of our experimental platform, see chapter 2. The choice of the hyperfine and zeeman state for our 3-levels ladder scheme (discussed in chapter 1) depends on the precise targeted Rydberg state and to our ability to optically pump our atoms. For those reasons, we are currently working with $|g\rangle = |5S_{1/2}, F = 1, m_F = +1\rangle$, an intermediate state $|e\rangle = |5P_{1/2}, F = 2, m_F = +2\rangle$ and the Rydberg state $|r\rangle = |nS, m_J = +1/2\rangle$. The optical pumping is done with a circularly polarized beam driving $5S_{1/2}, F = 1 \rightarrow 5P_{3/2}, F' = 1$. This beam is sent through the science cavity (200 MHz out of resonance) synchronized with a repumping beam on $5S_{1/2}, F = 2 \rightarrow 5P_{3/2}, F' = 2$ (our hyperfine pumping beam for the Raman) in freespace. As a result, the atoms accumulate in the dark state $|5S_{1/2}, F = 1, m_F = +1\rangle$. The step last 100 μ s but the repumper beam is only on in the first 20 μ s to ensure that atoms in $F = 1, m_F \neq +1$ fall in $F = 2$. Atoms in $F = 2$ will not participate to absorption and are used as a reservoir to increase the duty cycle.

The pumping purity directly impacts the transparency of our atomic sample in EIT configuration, the consequence of a bad optical pumping is discussed in more details in chapter 5. We now briefly describe the method employed to estimate the population in $5S_{1/2}, F = 1$ after pumping. We first apply a standard optical pumping sequence as described previously, then we sent a strong resonant beam on $5S_{1/2}, F = 2 \rightarrow 5P_{3/2}, F' = 3$ to remove atoms in $F = 2$. The population in a given hyperfine ground state $|5S_{1/2}, F = 1, m_F = 0, \pm 1\rangle$ can be coherently transferred to $|5S_{1/2}, F = 2, m_F\rangle$ by applying a π -pulse of radio frequency from the antenna used for magnetic field calibrations, see chapter 3. Indeed, each π -transition is well separated from others hyperfine lines by at least ~ 2 MHz thanks to the quantization magnetic field (3 G). After this coherent transfer, the magnetic field is switched off to ensure a degeneracy between Zeeman states in $F = 2$ to obtain an homogeneous distribution independent of the initial ground state (m_F). The ratio of atoms in each Zeeman state is measured by absorption imaging on $5S_{1/2}, F = 2 \rightarrow 5P_{3/2}, F' = 3$. After such a pumping step, we have $95(\pm 2)\%^{(6)}$ of the atomic ensemble pumped in $m_F = +1$ as shown in figure 4.9. If, for some reason, this value is not high enough, it is still possible to add a radio frequency step to coherently transfer atoms in the wrong Zeeman state to $F = 2$. The only concern is to previously removes atoms in $F = 2$, which may heat our atoms or induces losses.

4.2.2 Coupling to $|5S_{1/2}, F = 1\rangle \rightarrow |5P_{1/2}, F = 2\rangle$

We will now tackle the coupling of our cold atomic ensemble with the science cavity. In chapter 1 we have discussed the coupling of an ensemble of atoms to the electromagnetic field of a cavity. At that moment, we did not provide any specific mode for the light field. In chapter 2, we have presented the modes of our cavity and seen that the fundamental mode ($\text{TEM}_{0,0}$) is a Gaussian. The two main properties of our resonator are thus its roundtrip length that we will note $\ell \simeq 90$ mm⁽⁷⁾ and $w = 21 \mu\text{m}$ the waist of the fundamental mode. We are now able to estimate the coupling strength in this configuration. The field operator is given by:

$$\hat{E} = E_0 e^{-r^2/w^2} (\hat{a} + \hat{a}^\dagger), \text{ where } E_0 = \sqrt{\frac{2\hbar c}{\epsilon_0 \lambda \ell w^2}} \quad (4.8)$$

where the value of E_0 is obtained by computing the mean value of the power. The cavity coupling of a single atom at the waist of the mode is then $g_0 = dE_0/\hbar \simeq 2\pi \times 400$ kHz for a probe addressing $|5S_{1/2}, F = 1\rangle \rightarrow |5P_{1/2}, F = 2\rangle$. We clearly see that the coupling strength of a single atoms is well below the spontaneous emission rate and the cavity damping rate.

⁽⁶⁾Error at 1σ (Gaussian half width at $e^{-1/2}$).

⁽⁷⁾the length can be tuned by the two translation stages, see chapter 2.

Therefore, our experiment features no cooperative effect at the single atom level $C_0 \approx 1\%$. On the contrary, with a peak density of $4 \times 10^{11} \text{ cm}^{-3}$ and a rms width $\sigma_c = 5 \mu\text{m}$, we expect about ~ 800 atoms coupled to the cavity with a collective coupling strength of 10 MHz. This times the cooperative effect should be visible with $C \approx 6$. We now briefly presents some measurements of the atoms-cavity coupling.

Experimental sequence

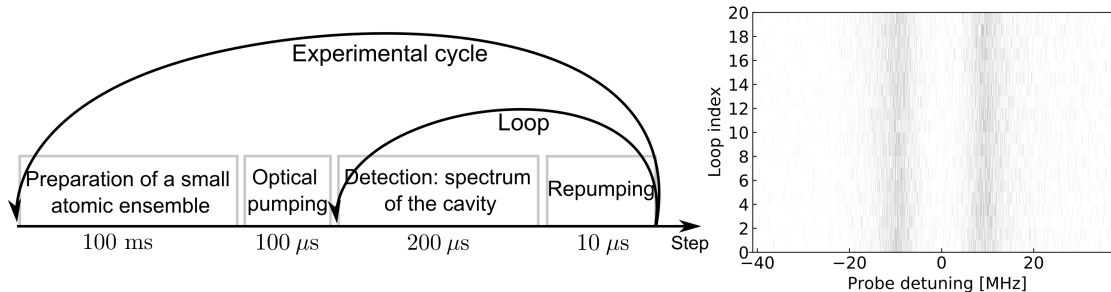


Figure 4.10: Sequence and stability. The typical experimental cycle for a spectrum measurement of the coupled system {atoms + cavity}. First the atomic ensemble is prepared as explained in the chapter 3 (~ 100 ms). Then a $100 \mu\text{s}$ of optical pumping is applied to put all the atoms in a unique Zeeman state. The cavity is scanned during $200 \mu\text{s}$ with the dipole trap on. The number of atoms is $F = 1, m_F = 1$ is then readjusted with a short repumping step. The acquisition plus the repumping step is repeated ~ 20 times (loop) before restarting the full experimental cycle. Right - Check of the coupling stability throughout the loops (in transmission). Photons detected are represented in grey. Here, the atoms cavity coupling is about 10 MHz and with $\sim 2\%$ of rms fluctuations.

We have first performed transmission measurements to characterize the coupling and more importantly the Rydberg Electromagnetically Induced Transparency. Here, we will not discuss the coupling with Rydberg states as it will be addressed in the next chapter.

The probe is sent through a double-pass AOM to scan over 80 MHz around the cavity resonance while the APD or a SPCM records the transmitted signal. The output intensity of the AOM is not flat over this frequency range and we use an intensity lock to compensate those drifts, as shown in figure 4.7. The sequence is first a preparation of the small atomic sample (about 100 ms, see Chapter 3 for a complete description) and then the optical pumping step ($100 \mu\text{s}$, see previous sub-section). The scan last $200 \mu\text{s}$ and we are able to repeat this measurement about ~ 20 times⁽⁸⁾ with the same atomic ensemble. Those measurements are interspersed with short repumping steps ($10 \mu\text{s}$) to maintain the Rabi frequency stable ($\simeq 2\%$ of rms fluctuations), as shown in figure 4.10, right plot. In practice we can have g between 0 and 20 MHz corresponding to a cooperativity, $C = g^2/(2\kappa\gamma)$, between 0 and 55 depending on the size of the atomic ensemble. We can also adjust this value by changing the repumping duration within the pumping step.

For reflection measurements, the intensity is locked before the fiber on the detection setup. We observe residual drifts that are compensated by a reference taken with the cavity locked on the next FSR. This reference signal is obtained with the cavity locked far away from the laser frequency and the atomic resonance. Otherwise, the sequence is similar to transmission measurements. When we want to used the homodyne detection, a $400 \mu\text{s}$ step is added before the acquisition, as we have explained in the previous section.

⁽⁸⁾this can be extended to a 100 or more but when we perform EIT it is not possible to go far beyond 20.

Transmission and reflection

In the strong coupling regime ($C \gg 1$) and if the cavity is resonant with a Rubidium transition, the transmission spectrum exhibits two resonances at $\pm g$. This is often called bright polaritons because the state is a mixture between the atomic ensemble and cavity photons. Indeed, we have seen in chapter 1 that $\langle P \rangle \approx \pm \langle a \rangle$ for $\delta\omega = \pm g$ in the strong coupling regime. One can in fact define two bosonic operators $B_{\pm} = (a \pm P)/2$ for each polariton with an associated lifetime given by $\gamma_B = (\kappa + \gamma)/2$. This decay rate is simply the probability to be a photonic excitation, $p(\text{ph}|B) = 1/2$, times its decay rate plus the probability to be an atomic excitation ($p(\text{at}|B) = 1/2$) times its damping rate. We can also find the transmission height of the two peaks with those simple arguments. We only record the photons that escapes from the cavity thus the transmission is the probability for a bright polariton to be desexcited as a photon during a shot time dt over the probability to be desexcited either as a photon or as an atomic excitation during this time interval. It gives here $T = \frac{\kappa^2}{(\kappa+\gamma)^2}$ and since $\gamma \simeq \kappa$ we observe a transmission of $\simeq 25\%$ on the figure 4.11. The field damping rate of the cavity κ is also estimated by looking at the cavity resonance without atoms, this is also visible in figure 4.11.

The same measurement can be done in reflection of the cavity. It is funny to notice that the reflectivity goes down to zero at the two resonances. Again we can make a simple model to understand this. When we probe the system at the resonance of one of the polaritons, we drive the system at a frequency $\Omega_B = \kappa \times p(\text{ph}|B) = \kappa/2$ per input photon while the losses rate is given by the spontaneous emission of the atomic part of a polariton: $\gamma \times p(\text{at}|B) = \gamma/2$. We are in a configuration where the loss rate is almost equal to the injection rate. We already discussed this in chapter II and it corresponds to a reflection close to zero. This phenomenon is similar to the reflection of (an empty) symmetric two-mirror cavity where the two mirrors share the same transmission coefficient.

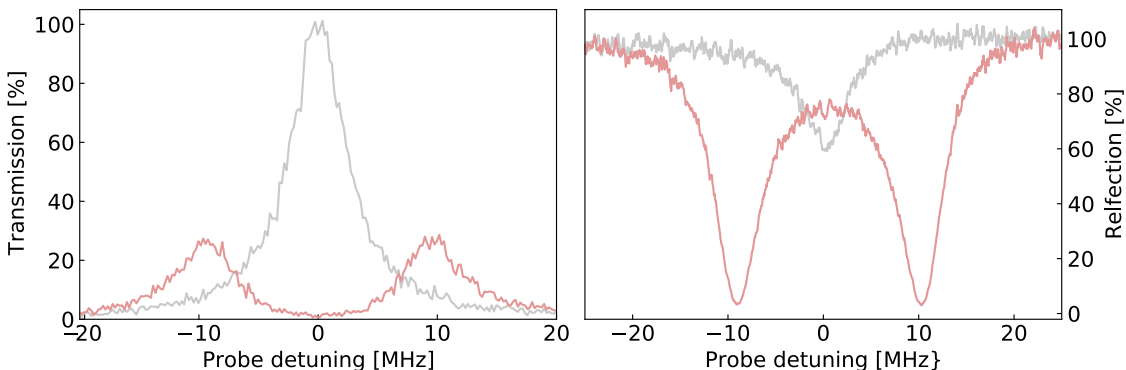


Figure 4.11: Atoms-cavity coupling. Observation of the strong coupling regime between the cavity and the atomic ensemble in transmission (left) and in reflection (right). The empty cavity spectrum (grey) gives access to the cavity's field damping rate $\kappa = 2.8$ MHz. When atoms are coupled, two peaks are visible on the transmission while the transmission features a drop at the two resonances $\pm g$.

Quadrature measurements

The last information we can get from the atoms-cavity coupling comes from the phase. The atom-cavity system is probed in the linear regime with weak coherent state such that the output is still a coherent state, see chapter 1. We have thus measured the mean value of two quadratures $\hat{X} = \hat{q}_0$ and $\hat{P} = \hat{q}_{\pi/2}$ to infer the phase of the output electromagnetic field. We expect to have a 2π phase shift when we scan the empty cavity resonance and

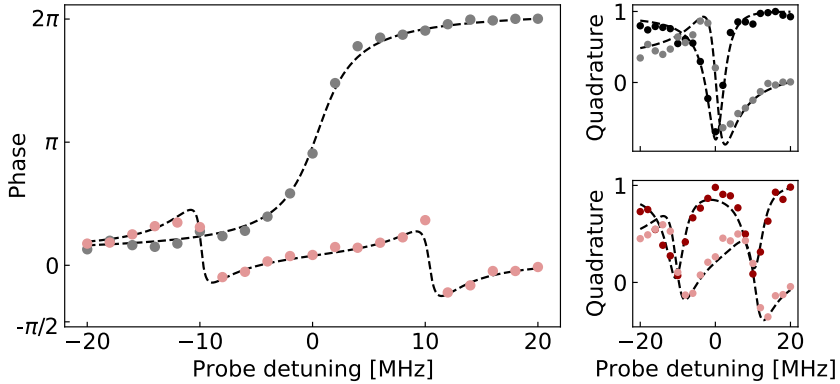


Figure 4.12: Quadratures and phase for the atoms-cavity coupling. Right- Phase spectrum for the empty cavity (grey) and with atoms coupled to the resonator (red). We observe a 2π -shift when the empty cavity resonance is crossed. The phase at zero detuning is π -shifted when atoms are coupled to the cavity. Left- X (dark colors) and P (light) quadratures are represented for the empty cavity (top) and for the atoms-cavity coupling (bottom). Notice that the amplitudes are normalized to one. Theoretical curves are fitted on the phases data alone (dashed lines). The only free parameters are an offset (15°) and the coupling ($g \simeq 10$ MHz).

this is what we observe in figure 4.12. When atoms are coupled to the cavity, the phase at resonance is π shifted compared to the empty cavity case. This is precisely what we expect to see with the strong nonlinearities of Rydberg atoms, a switch of the optical response of the system between zero and one photon inside the resonator. This will be the subject of the next chapter. We observe a phase variation near the resonance of the two bright polaritons. To understand this it is fruitful to change the coupling regime at fixed cooperativity. For instance, if we artificially decrease the cavity decay rate, and the coupling factor accordingly, such that are in a configuration where $g \gg \gamma \gg \kappa$. In this case the losses due to the atomic component is much more important and the incident light is reflected, the phase spectrum is then almost flat. On the contrary if $g \gg \kappa \gg \gamma$, the atomic losses are negligible: each polariton resonance is almost like a naked cavity mode and the phase is 2π shifted when we cross one of those resonances. This is illustrated in figure 4.13.

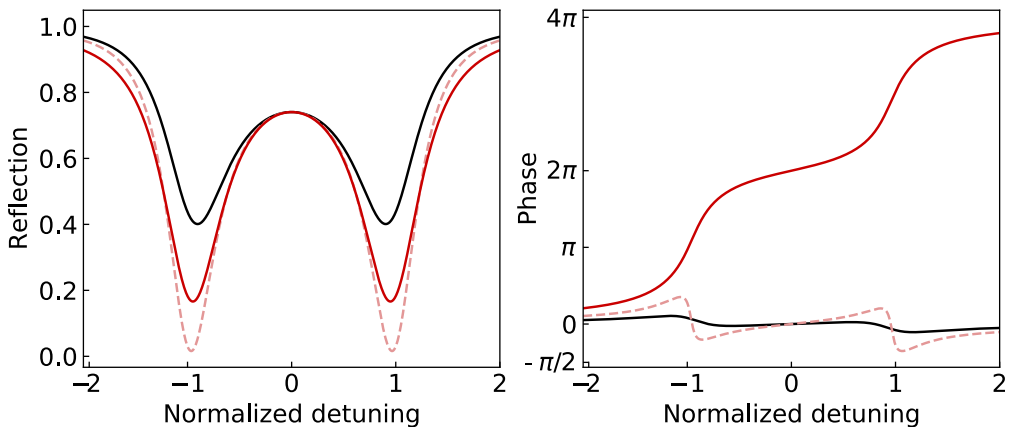


Figure 4.13: Reflection and Phase vs coupling regimes. Left - Reflection of the cavity as a function of the cavity damping rate κ but a fixed cooperativity $C = g^2/(2\kappa\gamma)$. Three configurations are considered: $g \gg \gamma \gg \kappa$ (black), $g \gg \kappa \simeq \gamma$ (dashed lines), $g \gg \kappa \gg \gamma$ (red). We see that the reflection goes up as we move away from $\kappa \simeq \gamma$ as explained in the text. Right- Phase as a function of the frequency for the three cases (same colors). We see that the field is reflected when $\gamma > \kappa$ and reflected otherwise at the polariton resonances (π -phase shift).

Part II

Observation of strongly interacting photons with a single Rydberg superatom

Bibliography

- [1] N. Šibalić, J. D. Pritchard, C. S. Adams, and K. J. Weatherill. “ARC: An open-source library for calculating properties of alkali Rydberg atoms”. In: *Computer Physics Communications* 220 (2017), pp. 319–331. ISSN: 00104655. DOI: 10.1016/j.cpc.2017.06.015. arXiv: 1612.05529. URL: <http://dx.doi.org/10.1016/j.cpc.2017.06.015>.
- [2] R. Calder and G. Lewin. “Reduction of stainless-steel outgassing in ultra-high vacuum”. In: *British Journal of Applied Physics* 18.10 (1967), pp. 1459–1472. ISSN: 05083443. DOI: 10.1088/0508-3443/18/10/313.
- [3] LIGO. “LIGO Vacuum Compatible Materials List”. In: *Laser Interferometer Gravitational Wave Observatory* (2014), pp. 1–24.
- [4] Bastian Hacker, Stephan Welte, Severin Daiss, Armin Shaukat, Stephan Ritter, Lin Li, and Gerhard Rempe. “Deterministic creation of entangled atom–light Schrödinger-cat states”. In: *Nature Photonics* 13.2 (2019), pp. 110–115. ISSN: 17494893. DOI: 10.1038/s41566-018-0339-5. arXiv: 1812.09604. URL: <http://dx.doi.org/10.1038/s41566-018-0339-5>.
- [5] Bastian Hacker. “Two-Photon Gate and Creation of Optical Cat States using One Atom in a Cavity”. In: (2019).
- [6] Atreju Tauschinsky, Rutger M.T. Thijssen, S. Whitlock, H. B. Van LindenVanDenHeuvell, and R. J.C. Spreeuw. “Spatially resolved excitation of Rydberg atoms and surface effects on an atom chip”. In: *Physical Review A - Atomic, Molecular, and Optical Physics* 81.6 (2010), pp. 1–5. ISSN: 10502947. DOI: 10.1103/PhysRevA.81.063411.
- [7] S. D. Hogan, J. A. Agner, F. Merkt, T. Thiele, S. Philipp, and A. Walruff. “Driving Rydberg-Rydberg transitions from a coplanar Microwave Waveguide”. In: *Physical Review Letters* 108.6 (2012), pp. 1–5. ISSN: 00319007. DOI: 10.1103/PhysRevLett.108.063004. arXiv: 1110.1256.
- [8] Jia Ningyuan, Alexandros Georgakopoulos, Albert Ryou, Nathan Schine, Ariel Sommer, and Jonathan Simon. “Observation and characterization of cavity Rydberg polaritons”. In: 041802 (2016), pp. 1–5. DOI: 10.1103/PhysRevA.93.041802.
- [9] Dorian Gangloff, Molu Shi, Tailin Wu, Alexei Bylinskii, Boris Braverman, Michael Gutierrez, Rosanna Nichols, Junru Li, Kai Aichholz, Marko Cetina, Leon Karpa, Branislav Jelenković, Isaac Chuang, and Vladan Vuletić. “Preventing and reversing vacuum-induced optical losses in high-finesse tantalum (V) oxide mirror coatings”. In: *Optics Express* 23.14 (2015), p. 18014. ISSN: 1094-4087. DOI: 10.1364/oe.23.018014. arXiv: 1505.03381.
- [10] Steven J.M. Habraken and Gerard Nienhuis. “Modes of a twisted optical cavity”. In: *Physical Review A - Atomic, Molecular, and Optical Physics* 75.3 (2007), pp. 1–11. ISSN: 10941622. DOI: 10.1103/PhysRevA.75.033819.

- [11] Yuan Jie, Long Xingwu, Liang Linmei, Zhang Bin, Wang Fei, and Zhao Hongchang. “Nonplanar ring resonator modes: Generalized Gaussian beams”. In: *Applied Optics* 46.15 (2007), pp. 2980–2989. ISSN: 15394522. DOI: 10.1364/AO.46.002980.
- [12] T. Akagi et al. “Development of a three dimensional four mirror optical cavity for laser-Compton scattering”. In: *Nuclear Instruments and Methods in Physics Research, Section A: Accelerators, Spectrometers, Detectors and Associated Equipment* 724 (2013), pp. 63–71. ISSN: 01689002. DOI: 10.1016/j.nima.2013.04.066. URL: <http://dx.doi.org/10.1016/j.nima.2013.04.066>.
- [13] Andreas Noack, Christina Bogan, and Benno Willke. “Higher-order Laguerre–Gauss modes in (non-) planar four-mirror cavities for future gravitational wave detectors”. In: *Optics Letters* 42.4 (2017), p. 751. ISSN: 0146-9592. DOI: 10.1364/ol.42.000751.
- [14] Ariel Sommer and Jonathan Simon. “Engineering photonic Floquet Hamiltonians through Fabry-Pérot resonators”. In: *New Journal of Physics* 18.3 (2016). ISSN: 13672630. DOI: 10.1088/1367-2630/18/3/035008. arXiv: 1511.00595.
- [15] Nathan Schine, Albert Ryou, Andrey Gromov, Ariel Sommer, and Jonathan Simon. “Synthetic Landau levels for photons”. In: *Nature* 534.7609 (2016), pp. 671–675. ISSN: 14764687. DOI: 10.1038/nature17943. arXiv: 1511.07381. URL: <http://dx.doi.org/10.1038/nature17943>.
- [16] Logan W. Clark, Nathan Schine, Claire Baum, Ningyuan Jia, and Jonathan Simon. “Observation of Laughlin states made of light”. In: *Nature* 582.7810 (2020), pp. 41–45. ISSN: 14764687. DOI: 10.1038/s41586-020-2318-5. arXiv: 1907.05872. URL: <http://dx.doi.org/10.1038/s41586-020-2318-5>.
- [17] S. L. Kaufman. “High-resolution laser spectroscopy in fast beams”. In: *Optics Communications* 17.3 (1976), pp. 309–312. ISSN: 00304018. DOI: 10.1016/0030-4018(76)90267-4.
- [18] Gerard A. Mourou, Toshiki Tajima, and Sergei V. Bulanov. “Optics in the relativistic regime”. In: *Reviews of Modern Physics* 78.2 (2006). ISSN: 00346861. DOI: 10.1103/RevModPhys.78.309.
- [19] A. Ashkin. “Acceleration and Trapping of Particles by Radiation Pressure”. In: *Physical Review Letters* 24.4 (1970), pp. 156–159. ISSN: 00319007. DOI: 10.1103/PhysRevLett.24.156.
- [20] J. L. Hall R.W.P. Drever. “Laser Phase and Frequency Stabilization Using an Optical Resonator”. In: 105 (1983), pp. 97–105.
- [21] A. J. Wallard. “Frequency stabilization of the helium-neon laser by saturated absorption in iodine vapour”. In: *Journal of Physics E: Scientific Instruments* 5.9 (1972), pp. 926–930. ISSN: 00223735. DOI: 10.1088/0022-3735/5/9/025.
- [22] T W Hansch and B Couillaud. “Laser frequency stabilization by polarization spectroscopy of a reflecting reference cavity”. In: *Optics Communications* 35.3 (1980), pp. 3–6.
- [23] Thibault Peyronel, Ofer Firstenberg, Qi Yu Liang, Sebastian Hofferberth, Alexey V. Gorshkov, Thomas Pohl, Mikhail D. Lukin, and Vladan Vuletić. “Quantum nonlinear optics with single photons enabled by strongly interacting atoms”. In: *Nature* 488.7409 (2012), pp. 57–60. ISSN: 00280836. DOI: 10.1038/nature11361.
- [24] Ningyuan Jia, Nathan Schine, Alexandros Georgakopoulos, Albert Ryou, Logan W Clark, Ariel Sommer, Jonathan Simon, Jia Ningyuan, Nathan Schine, Alexandros Georgakopoulos, Logan W Clark, Ariel Sommer, and Jonathan Simon. “A strongly interacting polaritonic quantum dot”. In: *Nature Physics* (2018).

- [25] E. L. Raab, M. Prentiss, Alex Cable, Steven Chu, and D. E. Pritchard. “Trapping of Neutral Sodium Atoms with Radiation Pressure”. In: *Physical Review Letters* 59.23 (1987), pp. 2631–2634. ISSN: 00319007. DOI: 10.1103/PhysRevLett.59.2631.
- [26] Daniel Adam Steck. “Rubidium 87 D Line Data”. In: (2019). URL: <http://steck.us/alkalidata>.
- [27] Paul D. Lett, Richard N. Watts, Christoph I. Westbrook, William D. Phillips, Phillip L. Gould, and Harold J. Metcalf. “Observation of atoms laser cooled below the doppler limit”. In: *Physical Review Letters* 61.2 (1988), pp. 169–172. ISSN: 00319007. DOI: 10.1103/PhysRevLett.61.169.
- [28] Z. T. Lu, K. L. Corwin, M. J. Renn, M. H. Anderson, E. A. Comell, and C. E. Wieman. “Low-Velocity intense source of atoms from a magneto-optical trap”. In: *Collected Papers of Carl Wieman* (2008), pp. 420–423. DOI: 10.1142/9789812813787_0057.
- [29] G. Reinaudi, T. Lahaye, Z. Wang, and D. Guéry-Odelin. “Strong saturation absorption imaging of dense clouds of ultracold atoms”. In: *Optics Letters* 32.21 (2007), p. 3143. ISSN: 0146-9592. DOI: 10.1364/ol.32.003143. arXiv: 0707.2930.
- [30] J. Dalibard and C. Cohen-Tannoudji. “Laser cooling below the Doppler limit by polarization gradients: simple theoretical models”. In: *Journal of the Optical Society of America B* 6.11 (1989), p. 2023. ISSN: 0740-3224. DOI: 10.1364/josab.6.002023.
- [31] Daniel Barredo, Vincent Lienhard, Sylvain de Léséleuc, Thierry Lahaye, and Antoine Browaeys. “Synthetic three-dimensional atomic structures assembled atom by atom”. In: *Nature* 561.7721 (2018), pp. 79–82. ISSN: 14764687. DOI: 10.1038/s41586-018-0450-2. arXiv: 1712.02727. URL: <http://dx.doi.org/10.1038/s41586-018-0450-2>.
- [32] Hu Zhang and Kuo Kang Liu. “Optical tweezers for single cells”. In: *Journal of the Royal Society Interface* 5.24 (2008), pp. 671–690. ISSN: 17425662. DOI: 10.1098/rsif.2008.0052.
- [33] Rudolf Grimm and Yurii B Ovchinnikov. “Optical dipole traps for neutral atoms”. In: (1987). arXiv: 9902072v1 [arXiv:physics].
- [34] D. Schrader, S. Kuhr, W. Alt, M. Müller, V. Gomer, and D. Meschede. “An optical conveyor belt for single neutral atoms”. In: *Applied Physics B: Lasers and Optics* 73.8 (2001), pp. 819–824. ISSN: 09462171. DOI: 10.1007/s003400100722. arXiv: 0107029 [quant-ph].
- [35] R. Jáuregui. “Nonperturbative and perturbative treatments of parametric heating in atom traps”. In: *Physical Review A - Atomic, Molecular, and Optical Physics* 64.5 (2001), p. 8. ISSN: 10941622. DOI: 10.1103/PhysRevA.64.053408.
- [36] Dian Jiun Han, Steffen Wolf, Steven Oliver, Colin McCormick, Marshall T. DePue, and David S. Weiss. “3D Raman sideband cooling of cesium atoms at high density”. In: *Physical Review Letters* 85.4 (2000), pp. 724–727. ISSN: 00319007. DOI: 10.1103/PhysRevLett.85.724.
- [37] Alban Urvoy, Zachary Vendeiro, Joshua Ramette, Albert Adiyatullin, and Vladan Vuletić. “Direct Laser Cooling to Bose-Einstein Condensation in a Dipole Trap”. In: *Physical Review Letters* 122.20 (2019), pp. 1–6. ISSN: 10797114. DOI: 10.1103/PhysRevLett.122.203202. arXiv: 1902.10361.
- [38] S. E. Hamann, D. L. Haycock, G. Klose, P. H. Pax, I. H. Deutsch, and P. S. Jessen. “Resolved-sideband raman cooling to the ground state of an optical lattice”. In: *Physical Review Letters* 80.19 (1998), pp. 4149–4152. ISSN: 10797114. DOI: 10.1103/PhysRevLett.80.4149.

- [39] Ivan H. Deutsch and Poul S. Jessen. “Quantum-state control in optical lattices”. In: *Physical Review A - Atomic, Molecular, and Optical Physics* 57.3 (1998), pp. 1972–1986. ISSN: 10941622. DOI: 10.1103/PhysRevA.57.1972.
- [40] Horace P. Yuen and Vincent W.S. Chan. “Noise in Homodyne and Heterodyne Detection.” In: 8.3 (1983), pp. 218–220. ISSN: 0146-9592. DOI: 10.1364/o1.8.000177.
- [41] G. L. Abbas, V. W. S. Chan, and T. K. Yee. “Local-oscillator excess-noise suppression for homodyne and heterodyne detection”. In: *Optics Letters* 8.8 (1983), p. 419. ISSN: 0146-9592. DOI: 10.1364/o1.8.000419.
- [42] Ulf Schnars, Claas Falldorf, John Watson, and Werner Jüptner. *Digital holography and wavefront sensing: Principles, techniques and applications*. 2015, pp. 1–226. ISBN: 9783662446935. DOI: 10.1007/978-3-662-44693-5.
- [43] P. Bertet, A. Auffeves, P. Maioli, S. Osnaghi, T. Meunier, M. Brune, J. M. Raimond, and S. Haroche. “Direct Measurement of the Wigner Function of a One-Photon Fock State in a Cavity”. In: *Physical Review Letters* 89.20 (2002), pp. 20–23. ISSN: 10797114. DOI: 10.1103/PhysRevLett.89.200402.
- [44] Brian Vlastakis, Gerhard Kirchmair, Zaki Leghtas, Simon E. Nigg, Luigi Frunzio, S. M. Girvin, Mazyar Mirrahimi, M. H. Devoret, and R. J. Schoelkopf. “Deterministically encoding quantum information using 100-photon Schrödinger cat states”. In: *Science* 342.6158 (2013), pp. 607–610. ISSN: 10959203. DOI: 10.1126/science.1243289.
- [45] Alexei Ourjoumtsev, Hyunseok Jeong, Rosa Tualle-Brouri, and Philippe Grangier. “Generation of optical ‘Schrödinger cats’ from photon number states”. In: *Nature* 448.7155 (2007), pp. 784–786. ISSN: 14764687. DOI: 10.1038/nature06054.
- [46] Olivier Morin, Kun Huang, Jianli Liu, Hanna Le Jeannic, Claude Fabre, and Julien Laurat. “Remote creation of hybrid entanglement between particle-like and wave-like optical qubits”. In: *Nature Photonics* 8.7 (2014), pp. 570–574. ISSN: 17494893. DOI: 10.1038/nphoton.2014.137. arXiv: 1309.6191.
- [47] Anatole Kenfack and Karol Zyczkowski. “Negativity of the Wigner function as an indicator of non-classicality”. In: *Journal of Optics B: Quantum and Semiclassical Optics* 6.10 (2004), pp. 396–404. ISSN: 14644266. DOI: 10.1088/1464-4266/6/10/003. arXiv: 0406015 [quant-ph].
- [48] U Leonhardt. *Measuring the quantum state of light*. Cambridge university press, 1997.
- [49] Halbert White. “Maximum Likelihood Estimation of Misspecified Models”. In: *Econometrica* 50.1 (1982), pp. 1–25.
- [50] Persi Diaconis. “The markov chain monte carlo revolution”. In: *Bulletin of the American Mathematical Society* 46.2 (2009), pp. 179–205. ISSN: 02730979. DOI: 10.1090/S0273-0979-08-01238-X.
- [51] A. I. Lvovsky. “Iterative maximum-likelihood reconstruction in quantum homodyne tomography”. In: *Journal of Optics B: Quantum and Semiclassical Optics* 6.6 (2004). ISSN: 14644266. DOI: 10.1088/1464-4266/6/6/014. arXiv: 0311097 [quant-ph].
- [52] D. Lee Y. Vardi. “From Image Deblurring to Optimal Investments : Maximum Likelihood Solutions for Positive Linear Inverse Problems Author (s): Y . Vardi and D . Lee Source : Journal of the Royal Statistical Society . Series B (Methodological), Vol . 55 , No . 3 Publish”. In: *Royal Statistical Society* 55.3 (1993), pp. 569–612.
- [53] Jürgen Appel, Dallas Hoffman, Eden Figueroa, and A. I. Lvovsky. “Electronic noise in optical homodyne tomography”. In: *Physical Review A - Atomic, Molecular, and Optical Physics* 75.3 (2007), pp. 1–4. ISSN: 10502947. DOI: 10.1103/PhysRevA.75.035802. arXiv: 0610116 [quant-ph].

- [54] A. Ourjoumtsev, A. Kubanek, M. Koch, C. Sames, P. W.H. Pinkse, G. Rempe, and K. Murr. “Observation of squeezed light from one atom excited with two photons”. In: *Nature* 474.7353 (2011), pp. 623–626. ISSN: 00280836. DOI: [10.1038/nature10170](https://doi.org/10.1038/nature10170).
- [55] Robert H. Hadfield, Martin J. Stevens, Steven S. Gruber, Aaron J. Miller, Robert E. Schwall, Richard P. Mirin, and Sae Woo Nam. “Single photon source characterization with a superconducting single photon detector”. In: *Optics InfoBase Conference Papers* 13.26 (2006), pp. 6746–6753. ISSN: 21622701. DOI: [10.1364/opex.13.010846](https://doi.org/10.1364/opex.13.010846).
- [56] B. K. Lubsandorzhiev. “On the history of photomultiplier tube invention”. In: *Nuclear Instruments and Methods in Physics Research, Section A: Accelerators, Spectrometers, Detectors and Associated Equipment* 567.1 SPEC. ISS. (2006), pp. 236–238. ISSN: 01689002. DOI: [10.1016/j.nima.2006.05.221](https://doi.org/10.1016/j.nima.2006.05.221).
- [57] R. Hambury Brown and R. Q. Twiss. “Correlation between photons in two coherent beams of light”. In: *Journal of Astrophysics and Astronomy* 15.1 (1994), pp. 13–19. ISSN: 02506335. DOI: [10.1007/BF03010401](https://doi.org/10.1007/BF03010401).
- [58] L. Mandel and E. Wolf. “Correlation in the fluctuating outputs from two square-law detectors illuminated by light of any state of coherence and polarization”. In: *Physical Review* 124.6 (1961), pp. 1696–1702. ISSN: 0031899X. DOI: [10.1103/PhysRev.124.1696](https://doi.org/10.1103/PhysRev.124.1696).
- [59] L. Mandel and E. Wolf. “Coherence properties of optical fields”. In: *Reviews of Modern Physics* 37.2 (1965), pp. 231–287. ISSN: 00346861. DOI: [10.1103/RevModPhys.37.231](https://doi.org/10.1103/RevModPhys.37.231).